Queen Mary, University of London

Ph.D Thesis

A Measurement of $\frac{\mathbf{W+jets}}{\mathbf{Z+jets}}$ with the ATLAS Detector

---

Author:
Gregory Fletcher

Supervisor:
Dr. Marcella Bona

December 17, 2014

A study is presented on the production of vector boson ($W^{\pm}$ and Z^0) events in association with recoiling hadronic activity in the form of hadronic jets, using proton-proton collisions at the LHC. The dataset was taken by the ATLAS detector during the 2011 data-taking run, at a centre of mass energy $\sqrt{s} = 7$ TeV, and corresponds to an integrated luminosity of 4.6 fb^{-1}. A measurement of the cross-section ratio of $\frac{\text{W+jets}}{\text{Z+jets}}$ events is defined, reducing the large systematic uncertainties inherent in the experimental measurement of such events. Inclusive and differential cross-sections are presented for $\frac{\text{W+jets}}{\text{Z+jets}}$, as a function of a range of kinematic variables, and are compared to state-of-the-art theoretical predictions.

Contents

1 Introduction **3**

2 Theory **7**

2.1 The Standard Model 7

2.1.1 Particles of The Standard Model 8

2.2 Quantum Electrodynamics, Gauge Invariance and Electroweak Theory 10

2.2.1 Charge Screening and Running Coupling in QED 13

2.3 Quantum Chromodynamics 14

2.3.1 Running Coupling and Asymptotic Freedom in QCD . . 15

2.3.2 Parton Distribution Functions 17

2.3.3 Hard Scatter and Factorisation Theorem 20

2.4 W and Z Boson Production 21

2.4.1 Production with Associated Hadronic Jets 24

2.4.2 Multi-jet Cross-Sections 26

2.5 Jet Reconstruction Algorithms 29

2.5.1 Cone Algorithms 29

2.5.2 Cluster Algorithms 30

2.6 Monte Carlo Generators 31

2.6.1 HERWIG 34

2.6.2 ALPGEN 34

2.6.3 SHERPA 34

2.6.4 BLACKHAT 35

3 The LHC and The ATLAS Detector 37

3.1 The LHC 37

3.2 The ATLAS Detector 39

3.2.1 Coordinate System 40

3.2.2 The Inner Detector 41

3.2.2.1 The Pixel Detector 42

3.2.2.2 The Semiconductor Tracker 43

3.2.2.3 Lorentz Angle in The SCT 44

3.2.2.4 The Transition Radiation Tracker 49

3.2.3 Electromagnetic Calorimeter 50

3.2.4 Hadronic Calorimeter 52

3.2.5 Muon Spectrometer 54

3.2.6 Trigger System 55

4 Detector Level Study of W+jets and Z+jets 59

4.1 Monte Carlo Simulation 59

4.2 Event Selection 61

4.2.1 Electron Selection 62

4.2.2 Muon Selection 63

4.2.3 W$\rightarrow l\nu$ events 64

4.2.4 $Z \rightarrow ll$ events 65

4.2.5 Jet Selection 65

4.3 Jet Calibration 72

4.3.1 Jet Origin and Pile-up Corrections 72

4.3.2 Jet Energy Scale 73

4.4 Detector Level Systematic Uncertainties 73

4.4.1 Jet Energy Scale Uncertainty 74

4.4.1.1 η-Intercalibration 75

4.4.1.2 Single-hadron response at large P_T 75

4.4.1.3 Non-closure 76
4.4.2 Jet-energy Resolution 76
4.4.3 Missing Transverse Energy 76
4.4.4 Lepton Systematic Uncertainties 77
4.4.4.1 Electron Uncertainties 77
4.4.4.2 Muon Uncertainties 78
4.4.5 Uncertainties on Monte Carlo Backgrounds 78
4.5 Detector Level Distributions 79

5 Background Characterisation 87
5.1 Data-Driven QCD Background 87
5.1.1 Muon Channel 89
5.1.1.1 Selection of Control Sample 90
5.1.1.2 Alternative Control Sample Selection 91
5.1.1.3 Fit Results 92
5.1.2 Electron Channel 97
5.1.2.1 Selection of Control Sample 97
5.1.2.2 Fit Results 98
5.1.3 Systematic Uncertainties 99
5.2 $t\bar{t}$ Background 102
5.2.1 Selection of Control Sample 104
5.2.2 Discriminating Variable 106
5.2.3 $t\bar{t}$ Fit 107
5.2.4 Systematic Uncertainties 108

6 Unfolding to Particle Level 113
6.1 Bayes' Theorem 114
6.1.1 Practical Application of Bayes' Theorem 115
6.2 Unfolding Method 116
6.2.1 Response Matrices 117
6.2.2 Fake Corrections 120

6.2.3 Closure Tests . . . 122
6.3 Systematic Uncertainties on the Unfolding Technique . . . 130
6.3.1 Statistical Unfolding Uncertainty . . . 130
6.3.2 Model Unfolding Uncertainty . . . 131
6.4 Systematic Uncertainties on the Unfolded Results . . . 134
6.5 Electron Channel Results Unfolded to Particle Level . . . 135

7 Theoretical Predictions 143
7.1 Sensitivity Study with Leading-Order Predictions . . . 143
7.2 Next-to-Leading Order Predictions . . . 145
7.2.1 Uncertainties on BH+S Predictions . . . 148
7.2.2 Corrections to BH+S Predictions . . . 149
7.2.2.1 Non-Perturbative Corrections . . . 149
7.2.2.2 Corrections for QED Final State Radiation . . 150
7.2.2.3 Acceptance Corrections . . . 151

8 Combined Results and Discussion 157
8.1 Combination of Electron and Muon Channels . . . 158
8.2 Results . . . 160
8.2.1 Jet Multiplicity . . . 160
8.2.2 Leading Jet P_T . . . 161
8.2.3 Sub-Leading Jet P_T . . . 165
8.2.4 Scalar Sum P_T . . . 168
8.2.5 Jet Rapidity . . . 172
8.2.6 Di-jet Variables . . . 173

9 Conclusion 179

List of Figures

2.1 The QCD colour field (between a $q\bar{q}$ pair) with $V(r) \sim r$ (left) and the QED Coulomb field (between an e^+e^- pair) with $V(r) \sim 1/r$ (right). 25

2.2 Formation of jets via splitting of $q\bar{q}$ pairs, producing a parton shower. 26

2.3 Lowest order diagrams for W or Z production with 1 associated hadronic jet in a hadron-hadron collision. 27

2.4 Final state configuration containing a W and 2 partons. 28

2.5 Comparison of the performance of 4 different jet algorithms in clustering a sample parton-level event (generated with HERWIG [18]) with many additional random soft particles [19]. 32

3.1 Schematic of the CERN site [29]. 38

3.2 The peak luminosity (left) and the peak pile-up (right) versus time during the proton-proton runs of 2010, 2011 and 2012. Figures taken from ATLAS public results [30]. 39

3.3 Schematic of the ATLAS detector [31]. 40

3.4 Schematic of the ATLAS Inner Detector [33]. 42

3.5 <111> and <100> crystal orientations. 46

3.6 $\eta - \phi$ map showing the position of the SCT modules with silicon sensors of <100> crystal orientation. Black: Layer 0; Green: Layer 2; Yellow: Layer 3. 46

3.7 Fits to cluster width vs incident angle for silicon modules in the three layers of the SCT barrel. Left: Side 0; Right: Side 1; Top: <111> modules; Bottom: <100> modules. 47

3.8 Lorentz angle result for cosmic ray data taken when he magnetic field was off. The fit was performed on a combined profile of all sides and layers. The error bar on this measurement is the statistical error from the fit. 48

3.9 Lorentz angle results for separate sides and layers, and for <111> and <100> modules. The systematic uncertainty band is derived from the study on cosmic ray events 49

3.10 Schematic of the ATLAS Calorimetry [47]. 53

3.11 Schematic of the ATLAS Muon Spectrometer showing the position of the muon chambers (top) [51] and their arrangement in the x-y plane (bottom) [52]. 56

4.1 Transverse mass (M_T), E_T^{miss} and W boson P_T distributions in the $W \to e\nu$ channel. The error band consists of all detector level systematics discussed in Section 4.4 and those associated with the data-driven QCD and $t\bar{t}$ background estimations discussed in Sections 5.1.3 and 5.2.4 respectively. 66

4.2 Z boson invariant mass and P_T distributions in the $Z \to ee$ channel. The error band consists of all detector level systematics discussed in Section 4.4 and those associated with the data-driven QCD background estimation discussed in Section 5.1.3. . 67

4.3 Illustration of the jet vertex fraction, here f refers to the fraction of P_T within Jet 2 that belongs to tracks originating from vertex PV1. 69

4.4 Electron and muon channel detector level systematic uncertainties for exclusive jet multiplicity. Top: Electron channel; Bottom: Muon channel; Left: W+jets channel; Right: Z+jets channel. 80

4.5 Detector level kinematic distributions (including data-driven backgrounds) for exclusive jet multiplicity. Left: W+jets channel; Right: Z+jets channel; Top: Electron channel; Bottom: Muon channel. 83

4.6 Detector level kinematic distributions (including data-driven backgrounds) for leading jet P_T. Left: W+jets channel; Right: Z+jets channel; Top: Electron channel; Bottom: Muon channel. 84

4.7 Detector level kinematic distributions (including data-driven backgrounds) for leading jet rapidity. Left: W+jets channel; Right: Z+jets channel; Top: Electron channel; Bottom: Muon channel. 85

5.1 Template fits to the E_T^{miss} distribution for exclusive jet multiplicities 0-5, in the $W \to \mu\nu$ + jets channel. Here "EWK + top processes" refers to the $(\text{Sig+Bkg})^{\text{SS}}$ template. 95

5.2 Template fits to the $M_{\mu\mu}$ distribution for exclusive jet multiplicities 0-2, in the $Z \to \mu\mu$ + jets channel. Here "EWK + top processes" refers to the $(\text{Sig+Bkg})^{\text{SS}}$ template. 96

5.3 Percentage uncertainties on the nominal QCD fraction in the $W \to \mu\nu$ + jets channel. 102

5.4 Feynman diagram depicting semileptonic top decay arising from quark-anitquark annihilation. 104

5.5 Template and results of the data-driven $t\bar{t}$ fits in the N_{jet}=3 (left) and N_{jet}=5 (right) bins, in the muon W channel. Errors on data points are statistical only. For jet multiplicity lower than 3, the $t\bar{t}$ background is taken from Monte Carlo simulation. Plots taken from [77]. 109

5.6 Fractional uncertainties on the nominal $t\bar{t}$ fraction in the $W \to e\nu$ + jets (top) and $W \to \mu\nu$ + jets (bottom) channels. Left: Up and Down variations for all systematics on the estimation method. Right: Fully symmeterised variations and the quadratic sum. 111

6.1 Electron channel response matrices for exclusive jet multiplicity (top), leading jet P_T (middle) and leading jet rapidity (bottom). Columns are normalised to the selection efficiency. Left: W+jets channel; Right: Z+jets channel. 119

6.2 Electron channel bin-by-bin fake correction factors for exclusive jet multiplicity (top), leading jet P_T (middle) and leading jet rapidity (bottom). Left: W+jets channel; Right: Z+jets channel. 123

6.3 Electron channel unfolded data distributions for exclusive jet multiplicity (top), leading jet P_T (middle) and leading jet rapidity (bottom). Left: W+jets channel; Right: Z+jets channel. Results are shown for unfolding with 1-6 Bayesian iterations and are compared to the corresponding particle-level ALPGEN Monte Carlo distribution. 124

6.4 Electron channel unfolded data distributions for the ratio of $\frac{\text{W+jets}}{\text{Z+jets}}$. Shown are the distributions of exclusive jet multiplicity (top left), leading jet P_T (top right) and leading jet rapidity (bottom). Results are shown for unfolding with 1-6 Bayesian iterations and are compared to the corresponding particle-level ALPGEN Monte Carlo distribution. 125

6.5 Electron channel closure tests for the W+jets channel. Shown are the exclusive jet multiplicity (top), leading jet P_T (middle) and leading jet rapidity (bottom) distributions. Left: ALPGEN closure test; Right: SHERPA closure test. In each case the result is compared to the corresponding particle-level distribution, from either ALPGEN or SHERPA. 127

6.6 Electron channel closure tests for the Z+jets channel. Shown are the exclusive jet multiplicity (top), leading jet P_T (middle) and leading jet rapidity (bottom) distributions. Left: ALPGEN closure test; Right: SHERPA closure test. In each case the result is compared to the corresponding particle-level distribution, from either ALPGEN or SHERPA. 128

6.7 Electron channel closure tests for the $\frac{\text{W+jets}}{\text{Z+jets}}$ channel. Shown are the exclusive jet multiplicity (top), leading jet P_T (middle) and leading jet rapidity (bottom) distributions. Left: ALPGEN closure test; Right: SHERPA closure test. In each case the result is compared to the corresponding particle-level distribution, from either ALPGEN or SHERPA. 129

6.8 Electron channel uncertainties on the unfolding procedure arising from Monte Carlo modelling and statistics for exclusive jet multiplicity (top row), inclusive jet multiplicity (2nd row), leading jet P_T in events with at least one jet (3rd row) and leading jet rapidity in events with at least one jet (bottom row). Left: W+jets; Right: Z+jets 133

6.9 Electron channel unfolded data distribution and theoretical predictions for exclusive jet multiplicity (top) and inclusive jet multiplicity (bottom). Left: W+jets channel; Right: Z+jets channel. 139

6.10 Electron channel unfolded data distribution and theoretical predictions for leading jet P_T in events with at least one jet (top) and second leading jet P_T in events with at least two jets (bottom). Left: W+jets channel; Right: Z+jets channel. 140

6.11 Electron channel unfolded data distribution and theoretical predictions for the scalar sum of all jet P_T (a variable referred to as S_T) in events with at least 2 jets (top) and leading jet rapidity in events with at least one jet (bottom). Left: W+jets channel; Right: Z+jets channel. 141

7.1 Comparison between ALPGEN+HERWIG and SHERPA theoretical predictions for the ratio of $\frac{\text{W+jets}}{\text{Z+jets}}$ events as a function of leading jet P_T. Top: Events with at least one jet; Bottom: Events with at least two jets. Left: Electron channel; Right: Muon channel. 146

7.2 Comparison between ALPGEN+HERWIG and SHERPA theoretical predictions for the ratio of $\frac{\text{W+jets}}{\text{Z+jets}}$ events as a function of S_T, measured for events with at least 2 jets. Left: Electron channel; Right: Muon channel. 147

7.3 Comparison between ALPGEN+HERWIG and SHERPA theoretical predictions for the ratio of $\frac{\text{W+jets}}{\text{Z+jets}}$ events as a function of leading jet rapidity, measured for events with at least one jet. Left: Electron channel; Right: Muon channel. 147

7.4 Electron channel QED final state radiation corrections for exclusive jet multiplicity (top) and leading jet P_T for events with at least one jet (bottom). Left: W+jets channel; Right: Z+jets channel 152

7.5 Electron channel QED final state radiation corrections for S_T for events with at least two jets (top) and leading jet rapidity in events with at least one jet (bottom). Left: W+jets channel; Right: Z+jets channel 153

7.6 Electron channel acceptance corrections for exclusive jet multiplicity (top) and leading jet P_T for events with at least one jet (bottom). Left: W+jets channel; Right: Z+jets channel 155

7.7 Electron channel acceptance corrections for S_T for events with at least two jets (top) and leading jet rapidity in events with at least one jet (bottom). Left: W+jets channel; Right: Z+jets channel 156

8.1 $\frac{\text{W+jets}}{\text{Z+jets}}$ ratio measurement of data unfolded to particle level in the combined electron and muon channel, presented as a function of exclusive (left) and inclusive (right) jet multiplicity. 161

8.2 $\frac{\text{W+jets}}{\text{Z+jets}}$ ratio measurement of data unfolded to particle level as a function of leading jet P_T for events with at least one jet, in the muon (left), electron (right) and combined (centre) channels. . . 163

8.3 $\frac{\text{W+jets}}{\text{Z+jets}}$ ratio measurement of data unfolded to particle level as a function of leading jet P_T for events with exactly one jet, in the combined channel. 164

8.4 $\frac{\text{W+jets}}{\text{Z+jets}}$ ratio measurement of data unfolded to particle level as a function of leading jet P_T for events with at least two jets, in the muon (left), electron (right) and combined (centre) channels. 166

8.5 $\frac{\text{W+jets}}{\text{Z+jets}}$ ratio measurement of data unfolded to particle level as a function of leading jet P_T for events with at least 3 jets, in the combined channel. 167

8.6 W+jets (left) and Z+jets (right) measurements of data unfolded to particle level as a function of leading jet P_T for events with at least two jets, in the combined channel. 167

8.7 $\frac{\text{W+jets}}{\text{Z+jets}}$ ratio measurement of data unfolded to particle level as a function of the second leading jet P_T for events with at least two jets, in the muon (left), electron (right) and combined (centre) channels. 169

8.8 $\frac{\text{W+jets}}{\text{Z+jets}}$ ratio measurement of data unfolded to particle level as a function of the third leading jet P_T for events with at least three jets, in the muon (left), electron (right) and combined (centre) channels. 170

8.9 $\frac{\text{W+jets}}{\text{Z+jets}}$ ratio measurement of data unfolded to particle level in the combined electron and muon channel, presented as a function of S_T for events with at least two (left) and three (right) jets. . 171

8.10 $\frac{\text{W+jets}}{\text{Z+jets}}$ ratio measurement of data unfolded to particle level as a function of the rapidity of the leading jet in events with at least one jet, in the muon (left), electron (right) and combined (centre) channels. 174

8.11 $\frac{\text{W+jets}}{\text{Z+jets}}$ ratio measurement of data unfolded to particle level as a function of the rapidity of the second leading jet in events with at least two jets, in the muon (left), electron (right) and combined (centre) channels. 175

8.12 $\frac{\text{W+jets}}{\text{Z+jets}}$ ratio measurement as a function leading jet rapidity obtained from MCFM with four different PDF sets: CT10 (black), NNPDF 2.3 (cyan), MSTW 2008 (blue) and HERAPDF (red). Plot taken from [77] 176

8.13 $\frac{\text{W+jets}}{\text{Z+jets}}$ ratio measurement of data unfolded to particle level as a function of the angular distance (ΔR) between the two leading jets in events with at least two jets, in the muon (left), electron (right) and combined (centre) channels. 177

8.14 $\frac{\text{W+jets}}{\text{Z+jets}}$ ratio measurement of data unfolded to particle level as a function of the separation in azimuthal angle, $\Delta\phi_{j_1,j_2}$, of the two leading jets in events with at least 2 jets, in the combined channel. 178

8.15 Comparison of ALPGEN+HERWIG and SHERPA theoretical predictions for $\Delta\phi_{j_1,j_2}$ between the two leading jets in events with at least two jets in the electron channel. Left: W+jets events; Right: Z+jets events. 178

List of Tables

2.1 The three generations of quarks in the Standard Model [3]. . . . 9

2.2 The three generations of leptons in the Standard Model [3]. . . . 9

2.3 The force mediating bosons of the Standard Model [3]. 10

2.4 Branching fractions for W decay modes [3]. 24

2.5 Branching ratios for Z decay modes [3]. 24

4.1 Monte Carlo samples of simulated events used in this analysis. Effective luminosities for those samples with separate components for different numbers of partons (0-5) are shown where necessary. 61

4.2 Electron and muon triggers used for the W$\rightarrow$ $l\nu$ and Z$\rightarrow$ ll event selection. The letters in brackets refer to the data-taking period. 64

4.3 Event preselection and lepton selections, common to both $W \rightarrow l\nu$ and $Z \rightarrow ll$ channels. 68

4.4 Vector boson and jet selections, common to both electron and muon channels. 69

4.5 Event yield table to show the number of events predicted by Monte Carlo simulation and data-driven methods (multi-jet events and $t\bar{t}$ events for 3 and 4 jets), compared with the total number of events observed in data. Top: W$\rightarrow$ $e\nu$ + jets event selection; Bottom: Z$\rightarrow$ ee + jets event selection. 70

4.6 Event yield table to show the number of events predicted by Monte Carlo simulation and data-driven methods (multi-jet events and $t\bar{t}$ events for 3 and 4 jets), compared with the total number of events observed in data. Top: W$\rightarrow \mu\nu$ + jets event selection; Bottom: Z$\rightarrow \mu\mu$ + jets event selection. 71

4.7 Detector level systematic uncertainties in the electron channel, values quoted as total percentage error. 81

4.8 Detector level systematic uncertainties in the muon channel, values quoted as total percentage error. 82

5.1 QCD fraction, signal contamination and total contamination for various QCD template candidates in the $W \rightarrow \mu\nu$ + jets channel. 93

5.2 Nominal QCD fractions obtained from the template fits for exclusive jet multiplicity bins in the $W \rightarrow \mu\nu$ + jets (once the E_T^{miss} requirement had been reapplied) and $Z \rightarrow \mu\mu$ + jets channels. 94

5.3 Nominal QCD fractions obtained from the template fits for exclusive jet multiplicity bins in the $W \rightarrow e\nu$ + jets (once the E_T^{miss} requirement had been reapplied) and $Z \rightarrow ee$ + jets channels. 99

5.4 Fractional systematic uncertainties on the QCD background estimation in the $W \rightarrow \mu\nu$ + jets channel (once the E_T^{miss} cut has been reapplied). 101

5.5 Fitted top fractions and the systematic uncertainties (quoted as total percentage error) on the $t\bar{t}$ background estimation in the electron and muon channels. 112

6.1 Fiducial regions of measurement at particle level for different channels. "OS" refers to a selection of two leptons of opposite sign, i.e. e^+e^- or $\mu^+\mu^-$. 118

6.2 Systematic uncertainties (quoted as total percentage error) on the unfolding method for the electron channel, in bins of exclusive and inclusive jet multiplicity. 132

6.3 Systematic uncertainties (quoted as total percentage error) on the unfolded results for the electron channel, in bins of inclusive jet multiplicity. 136

6.4 Systematic uncertainties (quoted as total percentage error) on the unfolded results for the muon channel, in bins of inclusive jet multiplicity. 137

8.1 Common phase space for W and Z boson channels and jet selection. "OS" refers to a selection of two leptons of opposite sign, i.e. e^+e^- or $\mu^+\mu^-$. 158

Chapter 1

Introduction

The Large Hadron Collider is a particle accelerator designed to produce proton-proton collisions at unprecedented energies. ATLAS is a general purpose detector designed to measure the products of such collisions, thereby allowing scientists to explore a new and extremely rich physics programme. In such an environment, certain components of the Standard Model of particle physics will be produced in abundance. Among them are the propagators of the weak nuclear force, namely the W and Z vector bosons[1]. Such particles will be produced in association with hadronic activity, which we can measure in ATLAS as "jets" of particles. It is therefore imperative for searches for new physics processes, and continued study of the Standard Model, to gain a comprehensive understanding of quantum chromodynamics (QCD). A deeper understanding of QCD will facilitate precise predictions of hadronic behaviour at the high energy frontier of experimental particle physics.

In addition, W and Z bosons with associated hadronic activity produce the same final state signatures as processes that could indicate the presence of new physics. A thorough understanding of how W+jets and Z+jets events behave is crucial to new physics studies, and studies of the Higgs boson, for which W+jets and Z+jets events are background processes.

[1]Throughout this work, W refers to either a W^+ or W^- boson, and Z refers to either a Z^0 or γ^* boson.

This work presents a measurement of the ratio of $\frac{\text{W+jets}}{\text{Z+jets}}$ events as a function of a wide range of kinematic variables. The decay modes of the W and Z bosons are very well understood, therefore an analysis of $\frac{\text{W+jets}}{\text{Z+jets}}$ events is a way to measure the differences in the kinematic distributions of hadronic jets recoiling from a W or Z, providing a precise test of QCD. The precise nature of this measurement draws from the fact that many sources of systematic uncertainty that dominate separate W+jets and Z+jets measurements, but are nevertheless common to both, are greatly reduced in the ratio.

A precise evaluation of state-of-the-art theoretical predictions of QCD effects can be extracted by comparing the measured ratio with predictions from Monte Carlo simulation and next-to-leading order calculations.

The measurement presented in this thesis was conducted on data acquired by the ATLAS detector during the 2011 LHC proton-proton run at a centre of mass energy of $\sqrt{s} = 7$ TeV. The first measurement of this kind was made by the ATLAS collaboration using data taken during the 2010 LHC run [1]. This measurement demonstrated the sensitivity of the ratio to QCD effects but suffered from statistical limitations and was therefore narrow in scope. The dataset employed in the analysis described here is over 100 times as large as that used in the former ratio measurement. This increase in statistics lead to a significant improvement in precision over a large region of phase space, and provided access to previously unobtainable differential distributions.

The structure of this work is as follows: Chapter 2 provides a theoretical background and overview of the Standard Model of particle physics, with particular emphasis placed on those concepts most relevant to the ratio measurement: the W and Z vector bosons and hadronic jets.

Chapter 3 discusses the LHC, specifically the process by which protons are accelerated to desired energies. The ATLAS detector is also discussed, detailing the various components pertinent to detecting events of the type that enter the $\frac{\text{W+jets}}{\text{Z+jets}}$ ratio. Additionally, a short study of the Lorentz angle as measured in the ATLAS Semiconductor Tracker is presented, this study was

conducted as part of the author's service task.

Chapter 4 describes the method by which W+jets and Z+jets events were selected from the 2011 dataset. Separate selections are detailed for the electron and muon decay channels. The way in which the ATLAS collaboration performs calibrations on hadronic jets is discussed, and the sources of systematic uncertainty entering the analysis at detector level are detailed. Detector-level distributions are shown for W+jets and Z+jets events, in both leptonic channels.

Chapter 5 details the way in which background events were characterised for this analysis. This chapter focuses on those backgrounds determined by data-driven techniques. They are multi-jet events from QCD processes passing the W+jets and Z+jets event selections, and $t\bar{t}$ events passing the W+jets event selection. A discussion of the sources of systematic uncertainty associated with each background estimation is included.

Chapter 6 details the Bayesian iterative method by which the distributions measured at detector level are "unfolded" to particle level. Unfolding was performed to account for detector effects and for direct comparison with theoretical predictions. Sources of systematic uncertainty associated with this method are presented and particle level distributions for W+jets and Z+jets events in the electron channel are shown.

Chapter 7 presents a short study with leading order Monte Carlo predictions that demonstrates the sensitivity of the ratio measurement to QCD radiation, and the decoupling of QED and QCD radiation in this analysis. Chapter 7 also includes a discussion of the theoretical predictions to which the unfolded data are compared. Most attention is paid to the next-to-leading order calculations provided by BLACKHAT+SHERPA, and the various bin-by-bin correction factors (and associated systematic uncertainties) required before direct comparisons can be made.

Finally, Chapter 8 provides a brief overview of the extrapolation of the two separate lepton channels from their respective fiducial phase space to a

common phase space, and the method by which the two measurements are combined. The $\frac{\text{W+jets}}{\text{Z+jets}}$ ratio is then presented at particle level, as a function of inclusive and exclusive jet multiplicity up to four jets. Additionally, differential measurements of the ratio are presented as a function of: (i) the transverse momentum and rapidity of the leading, second- and third-leading jets in events with at least one, two or three jets respectively, (ii) the scalar sum of all jet transverse momentum in events with at least two or three jets, and (iii) a set of "di-jet" variables in events with at least two jets. A discussion of each distribution and the salient features of their agreement or disagreement with theoretical predictions is included.

The analysis presented in this thesis was conducted within the ATLAS collaboration, by an analysis team of 12 people. The internal ATLAS note, that describes the full analysis in every detail, is over 850 pages long. For this reason, not every aspect of the analysis is discussed in this thesis, nor was the full analysis the sole work of the author. Instead, an attempt has been made to highlight the pertinent points at each stage of the analysis, with particular emphasis on the aspects that the author contributed to. The measurement of $\frac{\text{W+jets}}{\text{Z+jets}}$ is powerful due to the cancellation of many systematic uncertainties. Therefore, care has been taken to describe in detail the sources of systematic uncertainty entering the measurement at each stage of the analysis.

Additionally, the author worked on a separate analysis of W+jets events [2] which was conducted in parallel with the $\frac{\text{W+jets}}{\text{Z+jets}}$ measurement. The former measured a wider range of kinematic variables than those measured in the $\frac{\text{W+jets}}{\text{Z+jets}}$ analysis, but is not described here due to space constraints. All plots in this thesis were produced by the author, unless specified otherwise.

Chapter 2

Theory

2.1 The Standard Model

The Standard Model of particle physics describes the fundamental constituents of matter and the interactions between them. Decades of experimental evidence have revealed the Standard Model to be extraordinarily robust, successfully predicting the existence of many particles. Quantum field theory allows us to represent particles in terms of quantisable fields, therefore the Standard Model is best described as a theory of interacting fields. The dynamics of such fields can in turn be expressed by a renormalisable Lagrangian which is invariant under local gauge transformations. The requirement of invariance under symmetry transformations is of particular importance as it is this quality of the Standard Model Lagrangian that gives rise to conservable quantities and their associated conservation laws. This is a direct result of the theorem proved by Emmy Noether in 1915. For example, invariance under rotational translations leads to conservation of angular momentum and likewise time translation symmetry leads to conservation of energy.

One of the principal achievements of the Standard Model has been the successful description, within the same theoretical framework, of three of the four fundamental forces of nature: the electromagnetic, weak and strong forces,

expressed in terms of gauge theories as $U(1)$, $SU(2)$ and $SU(3)$ respectively. The Standard Model can be written as their combination, namely $SU(3) \times SU(2) \times U(1)$ (the combination of $SU(2) \times U(1)$ gives rise to what is formally known as electroweak theory). The mediators of the aforementioned forces and the particles on which they act are described in the following section. The fourth known force, gravity, is not included in the current Standard Model, described as it is by the theory of General Relativity.

2.1.1 Particles of The Standard Model

The fundamental particles of the Standard Model are categorised into two groups, defined by their intrinsic angular momentum (spin): bosons (integer spin) and fermions (half-integer spin). Each fermion and boson with non-zero quantum numbers has a corresponding antiparticle with the same mass, lifetime and equal-but-opposite charge. Fermions are sub-categorised into quarks and leptons, and three generations of particles, with increasing mass, exist for each. Quarks carry one of three colour charges (red, blue, green) and exist only in bound, colourless, states known as hadrons. This is a direct consequence of colour confinement, more on which in subsequent sections. Hadrons are comprised of either quark-anti quark pairs or three quarks; the former are known as mesons and have integer spin (e.g. pions and kaons) and the latter baryons which have half-integer spin (e.g. protons and neutrons). The three generations of quarks are grouped in pairs with a charge difference of one electron charge (e). Leptons are not confined to bound states and therefore exist freely. Each lepton also has an associated neutrino. Tables 2.1 and 2.2 summarise the three generations of quarks and leptons respectively.

The other primary category of elementary particles, bosons, are the force mediators in the Standard model. Massless photons (γ) mediate the electromagnetic force, by coupling to electric charge, and massless gluons (g) mediate the strong force, by coupling to colour charge. Massive $W^{\pm}$ and Z^0 bosons

Quark	Symbol	Charge (e)	Mass (GeV)	Spin ($h/2\pi$)
up	u	2/3	0.003	1/2
down	d	-1/3	0.006	1/2
strange	s	-1/3	0.1	1/2
charm	c	2/3	1.3	1/2
bottom	b	-1/3	4.2	1/2
top	t	2/3	173	1/2

Table 2.1: The three generations of quarks in the Standard Model [3].

Lepton	Symbol	Charge (e)	Mass (GeV)	Spin ($h/2\pi$)
electron	e	-1	0.0005	1/2
electron neutrino	ν_e	0	< 2 x 10^{-9}	1/2
muon	μ	-1	0.1	1/2
muon neutrino	ν_μ	0	< 2 x 10^{-9}	1/2
tau	τ	-1	1.8	1/2
tau neutrino	ν_τ	0	< 2 x 10^{-9}	1/2

Table 2.2: The three generations of leptons in the Standard Model [3].

Boson	Symbol	Charge (e)	Mass (GeV)	Spin ($h/2\pi$)
Photon	γ	0	0	1
Gluon	g	0	0	1
$W^{\pm}$	$W^{\pm}$	±1	80.385$\pm$0.015	1
Z^0	Z^0	0	91.188$\pm$0.002	1

Table 2.3: The force mediating bosons of the Standard Model [3].

mediate the charged and neutral current weak interactions respectively, and couple to all fermions. The bosons and their properties are summarised in Table 2.3.

2.2 Quantum Electrodynamics, Gauge Invariance and Electroweak Theory

Quantum electrodynamics (QED) is the quantum field theory (QFT) that describes the dynamics of the electromagnetic force. It is represented by a $U(1)$ gauge theory. As mentioned above, invariance under symmetry transformations is a fundamental principle of QFT. Following this guiding principle, the QED Lagrangian is formed by requiring invariance of the Dirac Lagrangian (where γ^{μ} are the Dirac matrices):

$$\mathcal{L}_{Dirac} = i\bar{\psi}\gamma^{\mu}\partial_{\mu}\psi - m\bar{\psi}\psi \tag{2.1}$$

under local gauge transformations:

$$\psi(x) \rightarrow \psi^{'}(x) = e^{i\alpha}\psi(x), \bar{\psi}(x) \rightarrow \bar{\psi}^{'}(x) = e^{-i\alpha}\bar{\psi}(x) \tag{2.2}$$

This is achieved by replacing ∂_μ with the covariant derivative $D_\mu = \partial_\mu - ieA_\mu$, which in turn requires the introduction of the photon gauge field A_μ. This field couples to charged particles and transforms as:

$$A_\mu \rightarrow A_\mu + \frac{1}{e}\partial_\mu A_\mu \tag{2.3}$$

Since A_μ is a physical field, a final term corresponding to its kinetic energy is added to the Lagrangian. This term must also be gauge invariant and thus involves the gauge invariant field strength tensor $F_{\mu\nu} = \partial_\mu F_\mu - \partial_\nu F_\nu$. The QED Lagrangian is therefore written as:

$$\mathcal{L}_{QED} = \bar{\psi}(i\gamma^\mu\partial_\mu - m)\psi + e\bar{\psi}\gamma^\mu A_\mu\psi - \frac{1}{4}F_{\mu\nu}F^{\mu\nu} \tag{2.4}$$

It can be shown from equation 2.4 that a non-zero mass term would break the gauge invariance of the QED Lagrangian, therefore the photon is required to be massless.

Electroweak theory was formulated independently by Sheldon Lee Glashow, Abdul Salam and Steven Weinberg as a way to construct a gauge invariant theory of the weak force, provided the electromagnetic force was also included. As mentioned in Section 2.1, electroweak theory is represented by a combination of the gauge theories based on the invariance groups $SU(2)$ and $U(1)$. The Lagrangian for the group $SU(2) \times U(1)$ contains three bosons associated with $SU(2)$, W^i_μ (i=1,2,3), and one associated with $U(1)$, B_μ. The kinetic energy terms for the vector boson fields (analogous to $-\frac{1}{4}F_{\mu\nu}F^{\mu\nu}$ in the QED Lagrangian) are:

$$\mathcal{L} = -\frac{1}{4}\sum_i (W_{\mu\nu})^i (W^{\mu\nu})^i - \frac{1}{4}B_{\mu\nu}B^{\mu\nu} \tag{2.5}$$

where:

$$B_{\mu\nu} = \partial_\mu B_\nu - \partial_\nu B_\mu \tag{2.6}$$

and

$$W^i_{\mu\nu} = \partial_\mu W^i_\nu - \partial_\nu W^i_\mu - g_W W^k_\mu W^l_\nu \epsilon^i_{kl} \tag{2.7}$$

where g_W is the gauge coupling of $SU(2)$ and ϵ^i_{kl} is the Levi-Civita symbol representing the permutation tensor. The non-abelian nature of $SU(2)$ results in the third term in Equation 2.7. This term corresponds to self coupling of the vector bosons, W^i_μ (directly analogous to gluon self coupling discussed in Section 2.3). W^i_μ and B_μ can be expressed in terms of the physical gauge fields W^+_μ, W^-_μ, Z_μ and A_μ, connected to the W^+, W^-, Z^0 bosons and the photon respectively:

$$W^1_\mu = \frac{1}{\sqrt{2}}(W^+_\mu + W^-_\mu) \tag{2.8}$$

$$W^2_\mu = \frac{i}{\sqrt{2}}(W^-_\mu - W^+_\mu) \tag{2.9}$$

$$W^3_\mu = cos\theta_w Z_\mu + sin\theta_w A_\mu \tag{2.10}$$

$$B_\mu = cos\theta_w A_\mu - sin\theta_w Z_\mu \tag{2.11}$$

where θ_w is the weak mixing angle. In this model all four bosons are massless. This contradicts what is observed in nature where only the photon is massless, whereas the $W^\pm$ and Z^0 vector bosons have the well defined masses given in Table 2.3. Additional explicit mass terms for $W^\pm$ and Z^0 violate the local gauge invariance of electroweak theory. For this reason, the Higgs mechanism of spontaneous symmetry breaking was formulated to allow the aforementioned bosons (as well as fermions) to have mass. The additional boson required by the Higgs mechanism was first observed at the LHC by the ATLAS [4] and CMS [5] experiments in July 2012. In electroweak theory spontaneous symmetry breaking rotates the W^i_μ and B_μ plane by θ_w, producing the Z^0 vector boson and the photon.

2.2.1 Charge Screening and Running Coupling in QED

As stated above, QED describes the interactions between charged particles via a massless photon. The strength of those interactions is determined by the fine structure constant, α. Spontaneous emission of a virtual photon, that annihilates into an electron-positron pair, can lead to the polarisation of the vacuum surrounding an electron, as positive charges are attracted to the negatively charged electron. The resulting effect of such e^-e^+ loops in the photon propagator is a screening of the negative electron charge, and thus a partial cancellation of the electric field. The effective charge of an electron is therefore dependent on probing distance, i.e. the closer you are, the smaller the effect of the polarised vacuum, and the larger effective electron charge. This means that the electromagnetic coupling is dependent on energy scale, q, and is referred to as a running coupling constant, $\alpha(q^2)$. The contribution from momentum transfers in the charge screening loops can be infinite and therefore a renormalisation scale, q_R^2, is introduced to avoid ultraviolet divergences. For this reason, a value for q_R^2 is chosen in the region $q_R^2 << q^2$. The running coupling of the fine structure constant can be expressed as a sum over all higher order corrections from virtual loops (in powers of $\ln(\frac{q^2}{q_R^2})$). For instance, to second order this can be expressed as:

$$\frac{1}{\alpha(q_R^2)} = \frac{1}{\alpha(q^2)} + \beta_0 \ln(\frac{q^2}{q_R^2}) + \dots \tag{2.12}$$

where $\beta_0 = \frac{N_f}{3\pi}$ is dependent on the number of fermion generations, $N_f = 3$. In the region $q_R^2 << q^2$, Equation 2.12 is approximated to:

$$\alpha(q^2) = \frac{\alpha(q_R^2)}{1 - \frac{\alpha(q_R^2)}{\pi}\ln(\frac{q^2}{q_R^2})} \tag{2.13}$$

2.3 Quantum Chromodynamics

Quantum Chromodynamics (QCD) describes the strong interaction between particles with colour charge. Colour charge is a property of quarks and gluons, and can take values of red (R), blue (B) or green (G). Mediated by massless gluons, the strong force is responsible for the binding together of quarks into hadrons, as mentioned in Section 2.1.1. Like QED, QCD is represented by a gauge theory, $SU(3)$, expressed by a Lagrangian invariant under local colour transformations:

$$\mathcal{L}_{QCD} = \bar{\psi_a}(i\gamma^\mu\partial_\mu - m)\psi_a + g_s(\bar{\psi_a}\gamma^\mu T_A\psi_a)G^A_\mu - \frac{1}{4}F^A_{\mu\nu}F^{\mu\nu}_A \tag{2.14}$$

The Lagrangian is a sum over indices: the colour indices, a (running from 1 to $N_c = 3$), and the colour degrees of freedom, A (running from 1 to 8, i.e. N_c^2-1). In the above equation g_s is the coupling constant of the strong interaction (analogous to α in the previous section), G^A_μ represent the gluon fields and ψ_a the colour-carrying quark fields in the fundamental triplet representation of $SU(3)$:

$$\psi(x) = \begin{pmatrix} \psi_R(x) \\ \psi_B(x) \\ \psi_G(x) \end{pmatrix} \tag{2.15}$$

The generators of $SU(3)$, T_A, are matrices that describe the couplings of the 8 types of gluon to different colour charges and are provided by the 8 Gell-Mann matrices λ_A, where $T_A = \frac{\lambda_A}{2}$. The four-gradient transform in Equation 2.3 was sufficient for the photon field. However, the gauge transformations of the gluon field can include rotations of its colour indices. Therefore, an extra term is added to the four-gradient transform:

$$G^A_\mu \rightarrow G^A_\mu + \partial_\mu\lambda^A - g_s f^{ABC}\lambda^B G^C_\mu \tag{2.16}$$

where f^{ABC} are the structure constants of $SU(3)$, and the indices A, B, C run over the 8 colour degrees of freedom. To ensure invariance under such gauge transforms, an additional term is required in the field strength tensor $F^A_{\mu\nu}$, which is expressed in terms of the gluon fields as follows:

$$F^A_{\mu\nu} = \partial_\mu G^A_\nu - \partial_\nu G^A_\mu + g_s f^{ABC} G^B_\mu G^C_\nu \tag{2.17}$$

The non-commuting third term in Equation 2.17 gives rise to the non-abelian nature of $SU(3)$ and leads to the interesting feature of gluon self-coupling (both cubic and quartic) that ultimately distinguishes QCD from QED. The implications of gluon self-coupling are discussed in more detail in the following section.

2.3.1 Running Coupling and Asymptotic Freedom in QCD

As mentioned in the previous section, QCD differs from QED in the crucial feature that gluons carry colour charge and can therefore self-interact, unlike electrically neutral photons. This means that gluons can not only emit quark-antiquark pairs to form loops, which screen the colour charge in the same manner as virtual photons discussed in Section 2.2.1, but also form virtual gluon loops. This latter phenomenon augments the colour field and therefore has the opposite effect of the quark-antiquark pairs, i.e. anti-screening. The consequence of this is that the coupling strength of QCD, α_s, is also a scale dependent, running coupling. Unlike the running coupling in QED, α_s has the inverse property that the QCD coupling strength is largest at larger distances.

The reduction of colour field strength at high energies means that at increasingly short distances the size of the force experienced by colour charges tends to zero. In this region they behave as if free. This is known as asymptotic freedom and means that in this regime perturbation theory can be applied to QCD.

To account for gluon self-coupling, the expression for the strong coupling constant must contain not only a renormalisation scale, q_R^2 (to avoid ultraviolet divergences), but also an additional term. The expansion of the coupling constant can be expressed as shown in Equation 2.12. In this case, β_0 is defined as $\beta_0 = \frac{1}{12\pi}(2N_f - 11N_c)$, where the term in N_c is an additional term to account for gluon self-interaction, and N_c is the number of colour charges. α_s can therefore be expressed as:

$$\alpha_s(q^2) = \frac{\alpha_s(q_R^2)}{1 - \frac{\alpha_s(q_R^2)}{12\pi}(2N_f - 33)ln(\frac{q^2}{q_R^2})} \tag{2.18}$$

which is commonly rearranged to give:

$$\alpha_s(q^2) = \frac{12\pi}{(33 - 2N_f)\ln(\frac{q^2}{\lambda_{QCD}^2})} \tag{2.19}$$

where λ_{QCD}^2 is the value of q_R^2 for which α_s tends to infinity, and is the limit at which perturbation theory can be applied to QCD calculations. This QCD scale represents the boundary between the perturbative and non-perturbative regions of QCD and has a value of $\sim$0.3GeV.

Protons are composite particles, therefore there are many interactions between partons during proton-proton ($p-p$) collisions at the LHC. The highest momentum transfer between partons in a proton-proton collision is termed the hard scatter. In order to calculate the hadronic cross-section of the hard scattering process, we must consider physics processes in two energy regimes, separated by the QCD scale, λ_{QCD}^2. As seen above, at energy scales greater than λ_{QCD}^2, α_s tends to zero and perturbation theory can be used to calculate the hard scatter partonic cross-section. At energies below λ_{QCD}^2 (long-distance processes), asymptotic freedom no longer holds and the constituents of the proton can no longer be resolved. In this energy region, experimentally-determined parton distribution functions (PDFs) are used to make calculations of the non-perturbative part of the hard scatter. In this manner, the two energy regimes are treated separately and combined by factorisation. Both PDFs

and factorisation are discussed in more detail in the following sections.

Interactions between proton remnants not included in the hard scatter are referred to as the "underlying event" (UE). The UE typically occurs at an energy scale lower than λ^2_{QCD} and therefore cannot be calculated from first principles using perturbation theory. Phenomenological models which are tuned to data are used to predict the behaviour of the UE. Once the hard scatter hadronic cross-section has been calculated via factorisation theorem, the UE is included to yield a prediction for the full hadronic cross-section.

2.3.2 Parton Distribution Functions

Deep inelastic scattering (DIS) of leptons off hadronic targets provides an extremely useful experimental technique to probe hadrons and reveal their quark and gluon substructure. From such experiments, we obtain a description of the momentum distribution of the quarks in a proton via the proton structure functions $F_1(x, q^2)$ and $F_2(x, q^2)$, where x is the momentum fraction of a given parton. As mentioned in Section 2.3.1, at sufficiently high energies asymptotic freedom allows the modelling of quarks within a proton as point-like particles, and as such the parton model arising from DIS can be extended to understand hadron-hadron collisions. Since the total momentum of a proton is shared among its constituent partons, it is necessary for cross-section calculations to know the momentum fraction carried by a particular parton. Such distributions of momentum fraction, x, for a quark or a gluon are known as parton distribution functions (PDFs). It is impossible to know the momentum fraction carried by a parton on an event-by-event basis, therefore PDFs are best described as the probability of a particular parton having momentum fraction between $x \to x + dx$ at a given momentum transfer, q^2. PDFs cannot be determined from perturbative calculations like the hard scatter processes in proton-proton collisions, rather they are extracted from global fits to data from DIS, Drell-Yan and jet production measurements. At high momentum

transfer the PDFs, $f_{quark}(x, q^2)$, are related to the aforementioned structure functions $F_1(x, q^2)$ and $F_2(x, q^2)$ as follows:

$$F_2(x, q^2) = \sum_i x f_{quark,i}(x, q^2) \tag{2.20}$$

where:

$$F_2(x, q^2) = 2xF_1(x, q^2) \tag{2.21}$$

and the index i runs over the quarks in a proton. Using Equations 2.20 and 2.21 we can extract the quark PDFs from the experimentally measured structure functions. This also helps us to understand the proton as consisting of "valence" and "sea" quarks. The three valence quarks, $u_v u_v d_v$, carry the electric charge and baryon quantum numbers, they radiate very many (a "sea" of) light quark-antiquark pairs ($q\bar{q}$). Since the "sea" contains quarks with mass, $m_{quark} << q^2$, we can assume it contains quarks of the three lightest flavours; u, d and s. The *Bjorken scaling hypothesis* states that F_1 and F_2 are not dependent on q^2 but rather are purely functions of momentum fraction x. Therefore, the number of u and d quarks in a proton can be expressed, as a function of momentum fraction x only, as the sum of the number of valence and sea quarks, i.e[1]:

$$u(x) = u_v(x) + u_s(x) \tag{2.22}$$

$$d(x) = d_v(x) + d_s(x) \tag{2.23}$$

$$u_s(x) = \bar{u_s}(x) = d_s(x) = \bar{d_s}(x) \approx s_s(x) \approx \bar{s_s}(x) \tag{2.24}$$

Furthermore, summing over all parton constituents of a proton it is necessary to retrieve the correct quantum numbers (charge: 1, baryon number: 1,

[1]It should be noted that in Equation 2.4 the strange quark PDFs are only approximately the same as the u and d quark PDFs, as the former are usually assumed to be suppressed with respect to the later. However, a recent study from ATLAS, whereby a PDF fit was performed using 2010 W/Z inclusive data, suggested that the strange quark PDFs are not suppressed [6].

strangeness: 0), hence the following summation laws:

$$\int_0^1 [u(x) - \bar{u}(x)]dx = 2 \tag{2.25}$$

$$\int_0^1 [d(x) - \bar{d}(x)]dx = 1 \tag{2.26}$$

$$\int_0^1 [s(x) - \bar{s}(x)]dx = 0 \tag{2.27}$$

A quark in the proton can emit a gluon and by this mechanism acquire large transverse momentum (P_T). The P_T of the parton is thus not restricted to being small, leading to logarithms of q^2. Such perturbations ultimately break the *Bjorken scaling hypothesis*. The consequence being that the structure functions are indeed dependent on momentum scale; decreasing with increasing q^2 at large values of x and exhibiting the opposite behaviour at small x.

The q^2 dependence of PDFs (directly from Equations 2.20 and 2.21) is dealt with by picking an initial momentum scale, q_0^2, and a functional form to be fit to data such as:

$$F(x, q^2 = q_0^2) = A_0(q_0^2)x^{A_1}(1-x)^{A_2}P(x) \tag{2.28}$$

where A_1 and A_2 are free parameters in the PDF fit to data, and $P(x)$ is a smooth function chosen to add flexibility to the PDF parameterisation. Constraints on the above functional form include the summation laws expressed in Equations 2.25-2.27. The Dokshitzer-Gribov-Lipatov-Atarelli-Parisi (DGLAP) [7, 8, 9, 10] equations are then employed to *evolve* the function up to the momentum scale of data, q^2.

The DGLAP equations contain a number of splitting functions, $P_{q_iq_j}$, P_{qg}, P_{gq}, P_{gg}, which describe the probability of a quark or gluon emitting a daughter quark or gluon with momentum fraction x of the longitudinal momentum of the parent parton. The splitting functions are perturbative expansions in the running coupling, α_s, in a generalised form:

$$P_{ab}(x, \alpha_s) = P_{ab}^{(0)}(x) + \frac{\alpha_s}{2\pi} P_{ab}^{(1)}(x) + ... \tag{2.29}$$

The splitting functions are the same for quarks and anti-quarks, this is a consequence of charge conjugation invariance. They are also independent of quark flavour as a consequence of flavour symmetry. They are typically calculated to next-to-leading order (NLO) and next-to-next-to-leading order (NNLO). The transverse momentum scale up to which the DGLAP equations are used to define the q^2 dependence of PDFs is called the "factorisation scale", q_F^2. This is defined as the scale which separates the long and short distance physics discussed in Section 2.3.1, i.e. emitted partons with momentum $< q_F^2$ are considered soft-processes, absorbed into the hadronic structure described by PDFs. Partons with momenta above the factorisation scale are part of the short-distance, hard scatter cross-section. The combination of the two distinct momentum regions to form the full hadronic cross-section is known as factorisation and is discussed in the following section.

The PDF description (before DGLAP evolution) of non-perturbative, soft-QCD effects (such as fragmentation, hadronisation processes and multiple-parton interactions) within a given collision at the LHC must be informed by empirical models from data.

2.3.3 Hard Scatter and Factorisation Theorem

As discussed in previous sections, the highest energy processes (above the factorisation scale, q_F^2) in a hadron-hadron collision are known as the hard-scatters. They occur at short distances, where α_s is small enough to allow the perturbative calculation of the parton-parton interaction cross-section ($\hat{\sigma_{ij}}$), while all other lower energy processes are absorbed by the PDFs of the protons in the collision. Therefore, the full hadronic cross-section for a physics process can be expressed via the factorisation theorem as:

$$\sigma = \sum_{i,j} \int dx_1 dx_2 f_i(x_1, q_F^2) f_j(x_2, q_F^2) \hat{\sigma_{ij}} \left(p_1, p_2, \alpha_s(q_R^2), \frac{q^2}{q_F^2}, \frac{q^2}{q_R^2} \right) \quad (2.30)$$

where the sum over i, j is a sum over all available partons. $f_{i,j}(x_{1,2}, q_F^2)$ are the PDFs of the partons evaluated at the factorisation scale, p_1 and p_2 are the momenta of the partons involved in the hard interaction, and q^2 is the momentum scale of the hard scatter. The renormalisation scale, q_R^2, is the momentum scale chosen to prevent divergences in QCD calculations arising from the running coupling strength of α_s, as discussed in Section 2.3.1. To avoid very large logarithms appearing in the perturbative calculations of $\hat{\sigma_{ij}}$, the factorisation and renormalisation scales are chosen to be of the order of the momentum scale of the hard scatter, i.e. typically $q_F = q_R = q$.

2.4 W and Z Boson Production

The $W^{\pm}$ and Z^0 gauge bosons were first observed at UA1 and UA2 at CERN in 1983 (via $p\bar{p}$ collisions) [11, 12]. They are the force mediators of the charged ($W^{\pm}$) and neutral (Z^0) current weak interactions, and couple to all fermions. The Standard Model decay widths of the $W^{\pm}$ and Z^0 (Γ_W=2.08 GeV and Γ_Z=2.50 GeV) are comparatively small against their masses (given in Table 2.3), so they are considered relatively stable. $W^{\pm}$ and Z^0 (referred to from now on as W and Z) can decay both leptonically and hadronically, Tables 2.4 and 2.5 give an overview of the decay modes and branching fractions (the fraction of bosons which decay by a specific decay mode) for W and Z respectively. The total cross-section for a given final state is therefore found by multiplying the vector boson production cross-section by the relevant branching ratio (BR), for example:

$$\hat{\sigma}(q\bar{q} \to Z \to l^+ l^-) = \hat{\sigma}(q\bar{q} \to Z) BR(Z \to l^+ l^-) \quad (2.31)$$

The W and Z production cross-sections can be derived by treating them as Drell-Yan[2] cross-sections, with the subprocess $q\bar{q} \rightarrow \gamma^* \rightarrow l^+l^-$ replaced by $q\bar{q} \rightarrow W \rightarrow l\nu$ and $q\bar{q} \rightarrow Z \rightarrow l^+l^-$ respectively. At lowest order, the cross-section for the Drell-Yan mechanism mediated by a photon is expressed as:

$$\hat{\sigma}\left(q(p_1)\bar{q}(p_2) \rightarrow l^+l^-\right) = \frac{4\pi\alpha^2}{3\hat{s}}\frac{1}{N}Q_q^2 \tag{2.32}$$

where Q_q^2 is the quark energy, $\hat{s}$ is the centre of mass energy, $(p_1+p_2)^2$, α is the electromagnetic coupling and the 1/N term arises as an average over the colour states of initial quarks (only quarks and antiquarks of the same colour can annihilate). Equation 2.32 can be extended to express the production of either a lepton pair or a lepton and a neutrino by quark-antiquark annihilation. For example, at energies around the Z mass, M_Z, terms for s-channel Z exchange are added to Equation 2.32 which becomes:

$$\hat{\sigma}\left(q(p_1)\bar{q}(p_2) \rightarrow l^+l^-\right) = \frac{4\pi\alpha_s^2}{3\hat{s}}\frac{1}{N}\left(Q_q^2 - 2Q_qV_lV_q\chi_1(\hat{s}) + (A_l^2+V_l^2)(A_q^2+V_q^2)\chi_2(\hat{s})\right) \tag{2.33}$$

where A and V are the axial and vector couplings of quarks and leptons to Z. χ_1 and χ_2 represent the Z/γ^* interference and the Z exchange amplitude respectively, given by:

$$\chi_1(\hat{s}) = \kappa\frac{\hat{s}(\hat{s}-M_Z^2)}{(\hat{s}-M_Z^2)^2+\Gamma_Z^2M_Z^2} \tag{2.34}$$

$$\chi_2(\hat{s}) = \kappa\frac{\hat{s}^2}{(\hat{s}-M_Z^2)^2+\Gamma_Z^2M_Z^2} \tag{2.35}$$

$$\kappa = \frac{\sqrt{2}G_FM_Z^2}{4\pi\alpha} \tag{2.36}$$

[2]The Drell-Yan process describes quark-antiquark annihilation (arising from hadron-hadron scattering) creating a virtual photon or Z, which in turn decay into a pair of leptons of opposite charge.

where G_F is the Fermi constant. At $\hat{s} \approx M_Z^2$, the χ_2 term dominates in Equation 2.33. Furthermore, as a result of the aforementioned small Z decay width, the narrow width approximation allows us to replace the Breit-Wigner distribution in χ_2 with a delta function, i.e:

$$\frac{1}{(\hat{s} - M_Z^2)^2 + M_Z^2\Gamma_Z^2} \approx \frac{\pi}{M_Z\Gamma_Z}\delta(\hat{s} - M_Z^2) \tag{2.37}$$

Finally, integrating over lepton-pair masses around M_Z (since the quark-antiquark pairs will have a spectrum of centre of mass energies) yields:

$$\begin{aligned}\int_{(M_Z-\Delta)^2}^{(M_Z+\Delta)^2} dM^2 \frac{d\hat{\sigma}}{dM^2} \approx \frac{\pi}{N}\sqrt{2}G_F M_Z^2(A_q^2 + V_q^2)\frac{\Gamma(Z \to l^+l^-)}{\Gamma_Z}\delta(\hat{s} - M_Z^2) \\ = \hat{\sigma}(q\bar{q} \to Z)BR(Z \to l^+l^-)\end{aligned} \tag{2.38}$$

where $|M - M_Z| < \Delta$ and $\Gamma_Z << \Delta << M_Z$, $\Gamma(Z \to l^+l^-)$ is the decay width of the Z to leptons only. From Equation 2.38 (and setting $N = 3$) we can extract the cross-section for Z production from quark-antiquark annihilation:

$$\hat{\sigma}(q\bar{q} \to Z) = \frac{\pi}{3}\sqrt{2}G_F M_Z^2(A_q^2 + V_q^2)\delta(\hat{s} - M_Z^2) \tag{2.39}$$

Similarly, the analogous cross-section for W production is found to be:

$$\hat{\sigma}^{q\bar{q}' \to W} = \frac{\pi}{3}\sqrt{2}G_F M_W^2|V_{qq'}|^2\delta(\hat{s} - M_W^2) \tag{2.40}$$

where in this case $V_{qq'}$ relates to the probability of transition between q and q', i.e the relevant element of the CKM mixing matrix between quark families [13, 14]. In this treatment of the cross-section for W production the narrow width approximation has once again been used to replace the Breit-Wigner distribution with a delta function. Under this approximation the transverse mass distribution for W decay is cut at M_W. In practice Γ_W is finite and thus the endpoint of the transverse mass distribution extends beyond M_W.

In high energy hadron-hadron collisions at the LHC, the final state of the hard scatter process will often contain extra quark-antiquark pairs or gluons.

$W^+(W^-)$ Decay Mode	Branching Fraction
$e^+\nu_e$ ($e^-\bar{\nu}e$)	$(10.75 \pm 0.13)\%$
$\mu^+\nu_\mu$ ($\mu^-\bar{\nu_\mu}$)	$(10.57 \pm 0.15)\%$
$\tau^+\nu_\tau$ ($\tau^-\bar{\nu_\tau}$)	$(11.25 \pm 0.20)\%$
Hadrons	$(67.60 \pm 0.27)\%$

Table 2.4: Branching fractions for W decay modes [3].

Z^0 Decay Mode	Branching Fraction
e^+e^-	$(3.363 \pm 0.004)\%$
$\mu^+\mu^-$	$(3.366 \pm 0.007)\%$
$\tau^+\tau^-$	$(3.367 \pm 0.008)\%$
Invisible ($\nu\bar{\nu}$)	$(20.00 \pm 0.06)\%$
Hadrons	$(69.91 \pm 0.06)\%$

Table 2.5: Branching ratios for Z decay modes [3].

Thus, the picture painted above is somewhat complicated both theoretically and experimentally. The following sections outline the theoretical approach to such final state objects and the experimental tools developed to measure the cross-sections of such processes.

2.4.1 Production with Associated Hadronic Jets

The final state of a hard scatter process in which a W or Z is produced, and decays into two leptons, can also include extra coloured partons, i.e. quarks and gluons. At high energies, quark-antiquark pairs begin to separate and

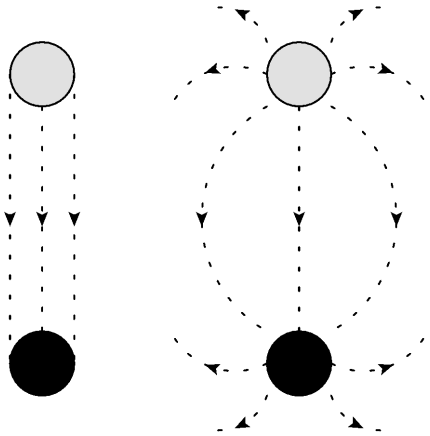

Figure 2.1: The QCD colour field (between a $q\bar{q}$ pair) with $V(r) \sim r$ (left) and the QED Coulomb field (between an e^+e^- pair) with $V(r) \sim 1/r$ (right).

the running of the strong coupling constant is such that the coupling strength between the two quarks increases with distance (as discussed in Section 2.3.1). The virtual gluons mediating the force between the separating quarks also carry colour charge and consequently self-interact, the effect of which is a squeezing of the gluon field between the quarks into a narrow flux tube (or QCD string). This is in contrast with QED for which there is no self-interaction of the mediating photons and therefore nothing preventing the Coulomb field lines between two electric charges spreading out, Figure 2.1 represents this pictorially.

The energy density per unit length of the so-called colour tube is constant. Therefore, with increasing distance, r, between the separating quarks, so does the potential energy of the two quark system increase, i.e. $V(r) \sim \lambda r$. This is the reason why quarks are not observed in free states, rather exist in combined colour singlet states as colourless hadrons, the phenomenon formally known as "colour confinement". As the quarks continue to separate, and their potential energy increases, it becomes energetically favourable to emit another quark-antiquark pair, in a direction almost collinear with the parent quark. The emission of the quark-antiquark pair occurs via the radiation of a gluon. In this way, the colour tube is fragmented into two shorter tubes as the colour

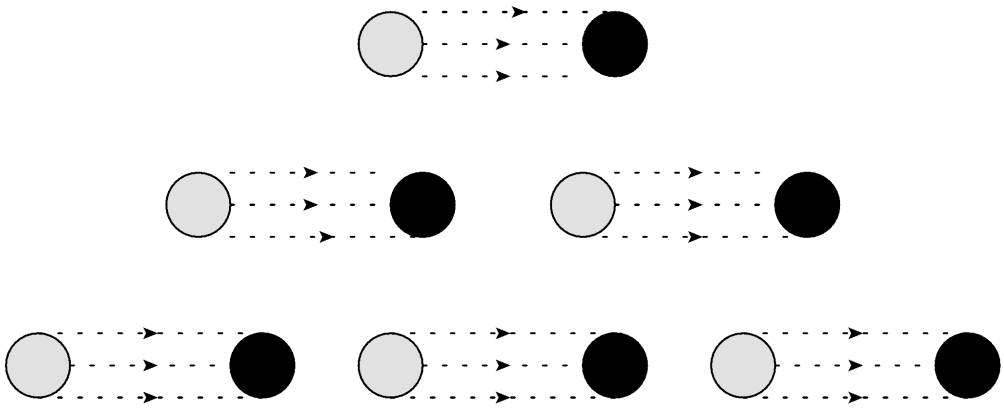

Figure 2.2: Formation of jets via splitting of $q\bar{q}$ pairs, producing a parton shower.

field experienced between the initial quarks is screened by the newly created pair. This process of fragmentation (depicted in Figure 2.2) is known as parton showering. The parton shower continues as the quark-antiquark pairs separate and in turn produce further pairs, each time of decreasing energy. What remains is a collimated "jet" of low-momentum quarks and gluons which combine (due to colour confinement, and via hadronisation) to colourless hadrons.

Jets of hadrons are what is experimentally observed in a particle detector. They provide a very powerful tool by which we can infer the existence of final state quarks and gluons from a hard scatter process. Section 2.5 describes how hadronic jets are experimentally defined and how jet-finding algorithms are used to detect them.

2.4.2 Multi-jet Cross-Sections

Figure 2.3 shows the subprocess by which a W or Z is produced in a hadron-hadron collision in association with 1 hadronic jet from a final state gluon.

In the case of W production, the factorised hadronic cross-section calculation for σ_{W+1j} can be rearranged and expressed as an integral over phase space:

$$\frac{d\sigma}{dq^2 dy dP_T^2} \sim \frac{1}{s} \int dy_g f_u(x_1, q^2) f_{\bar{d}}(x_2, q^2) \frac{|\mathcal{M}|^2}{\hat{s}} \tag{2.41}$$

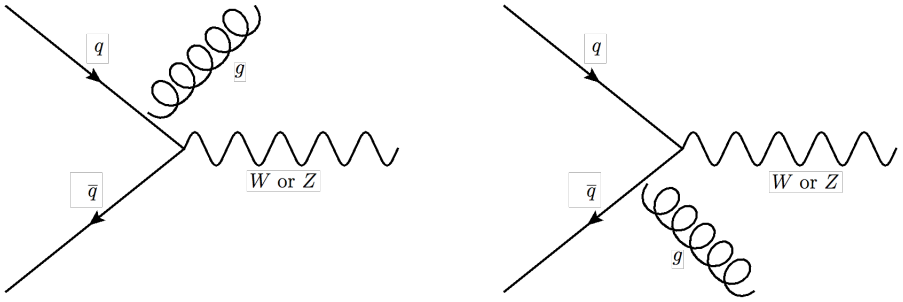

Figure 2.3: Lowest order diagrams for W or Z production with 1 associated hadronic jet in a hadron-hadron collision.

where P_T is transverse momentum, s is the centre-of-mass energy, and y is the quantity known as rapidity, defined as:

$$y = \frac{1}{2} ln \frac{E_i + P_{i,z}}{E_i - P_{i,z}} \tag{2.42}$$

The cross-section calculation contains matrix elements of the form:

$$|\mathcal{M}^{u\bar{d}\to W+g}|^2 \sim (\frac{\hat{t}^2 + \hat{u}^2 + 2q^2\hat{s}}{\hat{t}\hat{u}}) \tag{2.43}$$

where $\hat{s} = s_{u\bar{d}}$, $\hat{t} = s_{ug}$ and $\hat{u} = s_{\bar{d}g}$, thus the P_T of the gluon is expressed as $P_T^2 = \hat{t}\hat{u}/\hat{s}$. Problems arise when the final state parton is either collinear with the initial quarks, or becomes "soft" ($E_{parton} \to 0$), leading to $\hat{t} = 0$ or $\hat{u} = 0$. In these cases, the calculations contain divergences at the singularities (those from soft partons are termed "infrared" divergences). In order to avoid such divergences, restrictions are imposed on the phase space over which the cross-section is calculated. This can be illustrated by considering the integral over phase space of Equation 2.41 in the limit where $\hat{s} \to q^2$ and the P_T of the W is small. Here Equation 2.41 can be approximated to:

$$\frac{d\sigma}{d\mu^2 dy dP_T^2} \sim \frac{log(s/P_T^2)}{P_T^2} \tag{2.44}$$

From the above it is clear that unless a minimum P_T requirement on the gluon is applied ($P_{T_{min}}$), Equation 2.43 will diverge. Therefore, the cross-section result becomes proportional to $log(s/P_{T_{min}}^2)$. The full perturbative

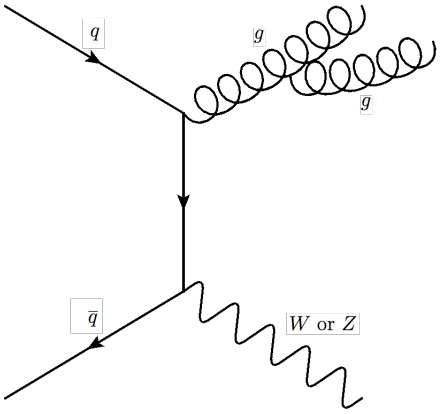

Figure 2.4: Final state configuration containing a W and 2 partons.

expansion for σ_{W+1j} calculations at high energies is thus an expansion in $\alpha_s log(\dots)$. The logarithm takes arguments dependent upon the jet definition parameters, e.g. the aforementioned minimum P_T, jet cone size and jet separation. The significance of the latter two quantities becomes clear when considering the process shown in Figure 2.4, where the event can be reconstructed as containing 0, 1 or 2 jets, depending on how a jet is defined.

Following the treatment of cross-section calculations outlined above, the full cross-section for the production of a W or Z boson, in association with hadronic jets, can be built from the sum of its multi-jet components, e.g:

$$\sigma_W = \sigma_{W+0j} + \sigma_{W+1j} + \sigma_{W+2j} + \sigma_{W+3j} + \dots \tag{2.45}$$

where:

$$\sigma_{W+0j} = a_0 + \alpha_s a_1 + \alpha_s^2 a_2 + \dots \tag{2.46}$$

$$\sigma_{W+1j} = \alpha_s b_1 + \alpha_s^2 b_2 + \dots \tag{2.47}$$

$$\sigma_{W+2j} = \alpha_s^2 c_2 + \dots \tag{2.48}$$

and a_i, b_i, c_i are the logarithmic functions discussed above. Finally, it is worthy of note that while the perturbative expansions are dependent upon the jet definition parameters, the sum at each order is independent.

2.5 Jet Reconstruction Algorithms

At the level of experiment, final state partons can only be inferred by the measurement of jets of hadrons which deposit energy in the calorimeters of a particle detector. In order to make valid comparisons between measured data and theoretical predictions, hadronic jets must be defined and measured in a consistent way across parton, hadron and detector levels. The general principle of a jet algorithm is to form a jet by combining final state hadrons and summing their 4-momenta.

There are certain general requirements that a successful jet algorithm must satisfy, such as being as independent of detector effects as possible. Additionally, the output of the algorithm must be invariant when treating soft and collinear partons in order to avoid divergences in cross-section calculations, of the type discussed in Section 2.4.2. This requirement is important not only in the theoretical treatment described above, but also experimentally since detectors cannot resolve either soft or collinear jets.

Jet algorithms can be broadly categorised by how the combination of final state hadrons is approached. There are two main types of jet algorithm: cone and cluster algorithms.

2.5.1 Cone Algorithms

Cone algorithms take a relatively simple approach to combining jet constituents: a "seed" particle above a specific P_T threshold is chosen within a cone of radius R and the 4-momenta of all particles that fall within the cone are summed. This procedure forms a "trial" jet, the direction of which becomes the axis for a redefined cone, and again all particles within the cone are combined and the 4-momentum of the trial jet is recalculated. Iterations continue until the direction of the jet is unchanged and is thus considered stable.

Complications arise when two cones overlap, in this case a "split-merge" procedure is applied by which jets that share hadrons are either merged into

one jet or the shared hadron is assigned to the jet whose axis it is closest to. This decision is made on the basis of a threshold parameter, this is a function of the percentage of P_T shared between the overlapping jets. The split-merge procedure is affected by soft partons, rendering cone algorithms exposed to infrared divergences and thus unfavourable for comparisons between data and theory.

2.5.2 Cluster Algorithms

The preferred approach at the LHC is to employ cluster jet algorithms. The idea is to recombine pairs of hadrons into one until all final state hadrons have been considered. Distance parameters d_{ij} and d_{iB} are defined to determine which particles are to be combined to form a jet. d_{ij} represents the distance between particles i and j, and d_{iB} represents the distance between particle i and the LHC beam. They are defined as:

$$d_{ij} = min(P_{T_i}^{2p}, P_{T_j}^{2p}) \frac{(\Delta R_{ij})^2}{R^2} \tag{2.49}$$

$$d_{iB} = P_{T_i}^{2p} \tag{2.50}$$

where p and R are parameters of the algorithm. ΔR_{ij} is defined as:

$$(\Delta R_{ij})^2 = (y_i - y_j)^2 + (\phi_i - \phi_j)^2 \tag{2.51}$$

In the above equations ϕ_i is the azimuthal angle of particle i and y is rapidity.

For a set value of the radius parameter R, d_{ij} and d_{iB} are calculated for all pairs of objects and the smallest distance is determined. If this is d_{ij}, objects i and j are combined into one pseudo jet, if d_{iB} is the smallest value then i is considered a complete jet and removed from the list of objects. d_{ij} and d_{iB} are then recalculated and the procedure repeats until all objects have been removed.

The choice of parameter p influences the relative influence of the energy to geometrical scales. This will of course influence the recombination procedure

and algorithms of this type can be subcategorised according to their choice of p. p=1 yields the $k_\perp$ algorithm [15], this implementation merges the softest objects first and works backwards to merge the hardest objects. In this way it attempts to approximate a reversal of parton showering, as described in Section 2.4.1. Choosing p=0, as in the Cambridge/Aachen algorithm [16], removes any dependence on the P_T of an object, so objects that have the smallest ΔR are merged first. It is sensitive to the distribution of soft objects and often produces jets with irregular shapes. Finally, a choice of p=-1 yields the anti-$k_\perp$ jet algorithm [17] which proceeds by merging hard objects then successively combining softer objects in the region $\Delta R < R$ of the hard object. The means that for anti-$k_\perp$, the shape of the final complete jets is unaffected by soft constituents. The jets will therefore be very well defined and roughly circular in the $y - \phi$ plane. This feature leads to easier calibration with the calorimeters of a detector. For this reason, anti-$k_\perp$ algorithms are favoured by the ATLAS experiment and anti-$k_\perp$ with a radius parameter of 0.4 are used for jet definition and selection throughout the analysis described in this thesis.

Figure 2.5 shows a comparison between the three different types of recombination jet algorithms, and one cone algorithm (SISCone). Each had the same particle inputs and value of the R parameter. All four reconstruct the same two jets with the highest P_T (shown in red and green), but the particles that comprise the jets differs between each algorithm. This means that the shape of the jets is quite varied, the uniform shape of the anti-$k_\perp$ algorithm jets is particularly clear, compared to the rather irregular shape of the $k_\perp$ algorithm jets.

2.6 Monte Carlo Generators

Monte Carlo generators are computer programs designed to simulate real physics processes according to a particular theoretical model, and to calculate the cross-section of said process within a defined kinematic region. The

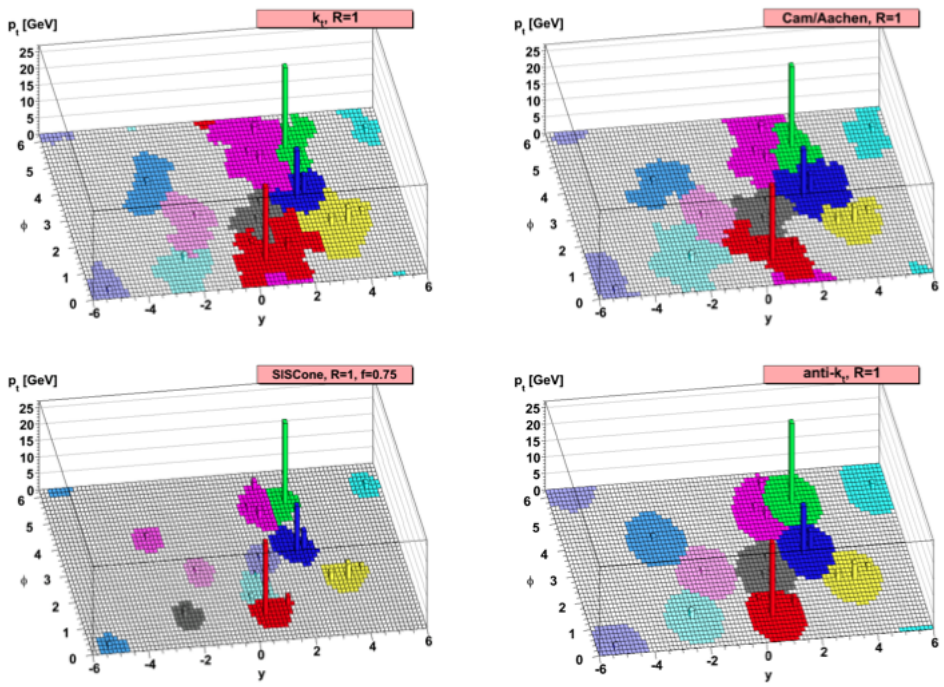

Figure 2.5: Comparison of the performance of 4 different jet algorithms in clustering a sample parton-level event (generated with HERWIG [18]) with many additional random soft particles [19].

simulations use random number generators to perform phase space integrations, thereby randomly sampling the cross-section over phase space.

For proton-proton collisions a generator proceeds on an event-by-event basis by first modelling the hard sub-process, then adding initial and final state bremstrahlung radiation via gluons. This is followed by the parton showers (resulting from bremstrahlung), their hadronisation, and the subsequent decay of the colourless hadrons. Finally, interactions and decays of all proton remnants (known as the underlying event) are simulated. The 4-vector information of all simulated particles is outputted.

This is the first stage of Monte Carlo event simulation, what remains is to account for detector effects (i.e. the interaction of particles in the volume of the detector). This is achieved by passing the hadron level objects (as 4-vectors) through a simulation (GEANT4 [20] in the case of ATLAS) of the materials in the detector and their location. The final output of this stage is in the same format as raw data collected by the detector (e.g. as charges measured on tracker wires, electronic pulses in the calorimeter anodes etc.) and can therefore be reconstructed in the same way as raw data. In this way, a full simulation of how an event would be observed in the detector is achieved. The Monte Carlo events can then be used in an analysis for direct comparison between theoretical models and experimental data.

A number of different generators are available, each of which simulate different theoretical models by employing different matrix elements, PDFs, evolution equations and models for parton showering and hadronisation. One of the aims of the analysis presented in this thesis is to provide a precise test of how well certain state-of-the-art theoretical predictions (as implemented through Monte Carlo generators) describe the measured data, in the region of perturbative QCD. The generators most pertinent to this analysis are described below. HERWIG, ALPGEN and SHERPA are all leading-order Monte Carlo generators.

2.6.1 HERWIG

HERWIG is a general-purpose event generator for high energy processes which places a particular emphasis on detailed simulation of parton showers. The evolution of the parton shower is ordered angularly and a cluster model for jet hadronisation is utilised. HERWIG v6.520 [18] (as used in this analysis) requires an interface with JIMMY v4.31 [21] to provide the underlying event modelling, but HERWIG++, contains an in-built underlying event algorithm.

2.6.2 ALPGEN

ALPGEN is specifically designed to model hard processes with multiple partons in hadronic collisions. Events with up to 6 final state partons are simulated via leading-order matrix elements, yielding a very useful tool for the study of final states with several hard and well separated jets. In the analysis presented in this thesis ALPGEN v2.13 [22] (employing CTEQ6L1 PDFs [23]) is used and is interfaced with both HERWIG v6.520 (to provide the parton shower and fragmentation modelling) and JIMMY v4.31 (to model the underlying event).

2.6.3 SHERPA

SHERPA is a general-purpose tool for the calculation of both hard scattering processes within the Standard Model and also various new physics models. Like ALPGEN, it employs leading-order matrix elements to calculate the cross-section of processes with multiple hard jets in the final state. However, it differs from ALPGEN in that it utilises self-contained algorithms for the modelling of the parton shower, hadronisation and underlying event. SHERPA v1.4.0 [24] (with CT10 PDFs [25]) is used in this analysis.

2.6.4 BLACKHAT

BLACKHAT [26, 27, 28] is an automated program for performing next-to-leading order (NLO) QCD calculations for events with high final state multiplicity. It provides perturbative QCD predictions for W and Z production in association with up to 4 jets via the computation of virtual one-loop amplitudes. BLACKHAT is combined with SHERPA, which provides the real emission part of the calculation.

The inclusion of NLO calculations in theoretical predictions of W+jets and Z+jets production has the advantage of greatly reducing the factorisation and renormalisation dependencies suffered by leading-order predictions.

Chapter 3

The LHC and The ATLAS Detector

3.1 The LHC

Located at the European Organisation for Nuclear Research (CERN) on the Franco-Swiss border, the Large Hadron Collider (LHC) is a particle accelerator of 26.7 km circumference situated underground, at depths between 45-170 m below surface level. It is primarily designed to collide proton beams at a peak centre of mass energy of 14 TeV. The protons must first undergo a series of accelerations to increase their energy and create the bunches of which the beam is comprised. The process begins with LinacII, a linear accelerator in which the application of an electric field ionises hydrogen atoms to yield free protons that are subsequently accelerated to an energy of 50 MeV. The energetic protons are then injected into the Proton Synchrotron Booster (PSB), an intermediary circular accelerator that increases the proton energy to 1.4 GeV before injection into the larger Proton Synchrotron (PS). The PS squeezes the proton beam into bunches with 2 ns separation and accelerates the protons to an energy of 25 GeV. The final stage before entering the main LHC ring is injection into a larger synchrotron known as the Super Proton Synchrotron (SPS), the purpose

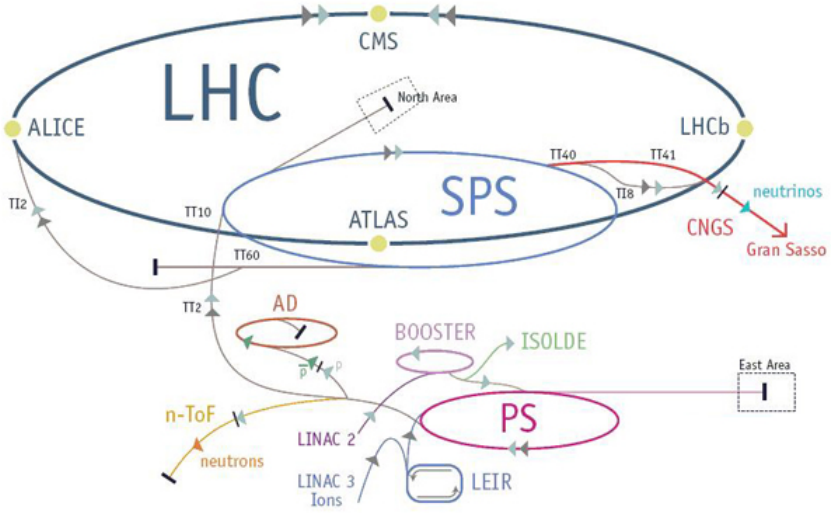

Figure 3.1: Schematic of the CERN site [29].

of which is to accelerate the protons to 450 GeV before entering into the LHC as two beams circulating in opposite directions. Radio frequency cavities within the LHC are used to accelerate the protons. The cavities contain electric fields which accelerate charged particles that pass through them. Superconducting dipole magnets provide a strong magnetic field to steer the accelerated protons around the LHC ring and quadrupole magnets focus the beam as it circulates. Once the desired beam energy is achieved, extra fine tuning is employed to focus and collide the two beams at 4 interaction points on the LHC ring. The interaction points correspond to the site of 4 particle detectors: ATLAS, CMS, LHCb and ALICE. The former two are general-purpose detectors, while the latter two have designs optimised for the study of specific physics: the properties of B mesons, and heavy-ion collisions respectively. Figure 3.1 shows a schematic of the LHC, including an overview of the various sub-accelerators discussed above.

The rate of production, R, of a given physics process is related to the corresponding cross-section[1] (σ) by $R = \mathcal{L}\sigma$, where $\mathcal{L}$ is the instantaneous luminos-

[1]The cross-section, σ, of a process is expressed as an effective area that is connected to the probability of that process occurring.

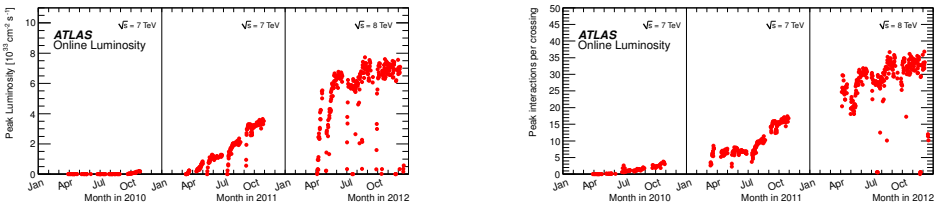

Figure 3.2: The peak luminosity (left) and the peak pile-up (right) versus time during the proton-proton runs of 2010, 2011 and 2012. Figures taken from ATLAS public results [30].

ity, a quantity proportional to the beam intensity. The total luminosity is the time integration of instantaneous luminosity. A large instantaneous luminosity is desirable, particularly when studying processes with small cross-sections. This can be achieved by increasing 3 quantities; the number of bunches, the proton density per bunch or the beam focus. Instantaneous luminosity is related to the number of bunches (n_b), the number of protons in the colliding bunches (n_1, n_2), and the horizontal and vertical widths of the beam profile (σ_x and σ_y respectively) by $\mathcal{L} = \frac{n_b f_r n_1 n_2}{2\pi\sigma_x\sigma_y}$, where f_r is the rotation frequency of the beam. The challenge presented with increased instantaneous luminosity is the increase in particle interactions occurring simultaneously with the hard scatter process in which we are interested, otherwise known as pile-up events. This relation is illustrated in Figure 3.2, as the peak luminosity increases over time, so does the peak number of interactions per crossing.

3.2 The ATLAS Detector

A Toroidal LHC ApparatuS (ATLAS) is a general-purpose detector located at one of the collision points on the LHC ring. ATLAS has a very broad physics programme and is designed to observe many particles with high precision, which in turns facilitates the inference of those particles that cannot be directly detected. The detector consists of four major components, moving out from the interaction point they are: the Inner Detector used for high precision tracking of charged particles close to the interaction point, the Elec-

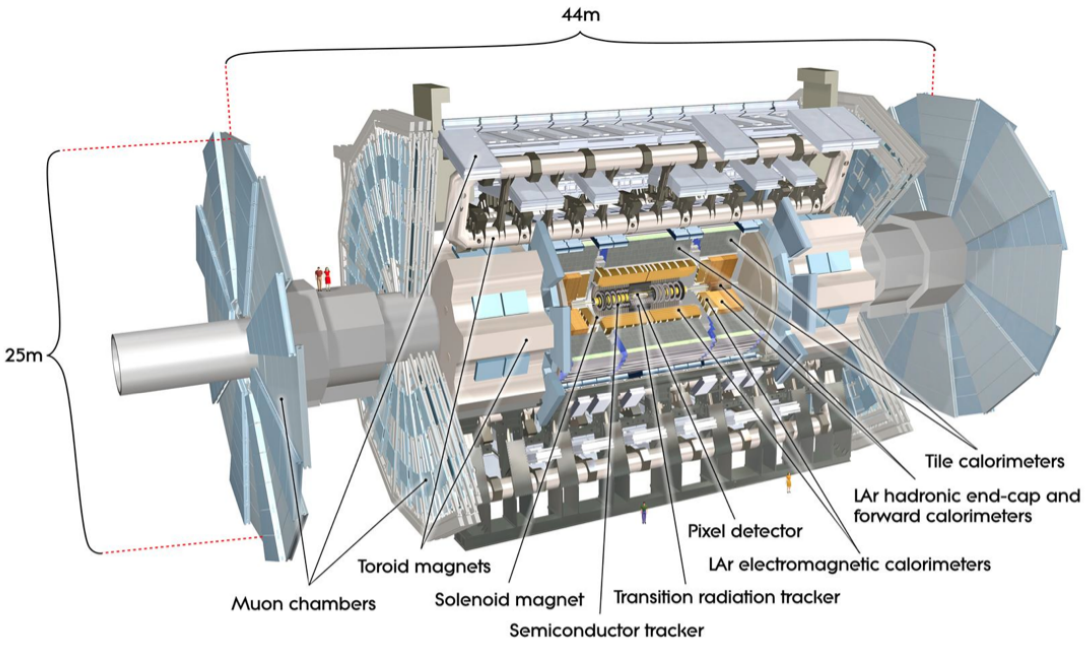

Figure 3.3: Schematic of the ATLAS detector [31].

tromagnetic and Hadronic Calorimeters for measuring the energy deposits of electrons/photons and hadrons respectively, and the Muon Spectrometer for identifying and measuring muons. Figure 3.3 depicts the arrangement of the above components in the detector.

Momentum measurements of charged particles are achieved through the ATLAS magnet system: the solenoid magnet which encloses the Inner Detector and the toroidal magnet system contained within the Muon Spectrometer. The magnets serve the purpose of bending the trajectory of charged particles. The curvature of the bent track is proportional to the momentum of the particle and the direction of curvature reveals its charge.

3.2.1 Coordinate System

The ATLAS detector employs a right-handed coordinate system. The z-axis is defined along the beam pipe, positive in a anti-clockwise direction around the LHC ring. The x-y plane is perpendicular to the z-axis (intersecting at

0), positive x points towards the centre of the LHC ring and positive y points upwards. Transverse quantities[2], such as momentum (P_T) and energy (E_T), are defined in the x-y plane, i.e. perpendicular to the beam line. The azimuthal angle, ϕ, covers the range [-π,+π] around the beam pipe, measuring ϕ=0 along x-axis and increasing clockwise when looking in the direction of positive z. The polar angle, θ, is the angle from the beam axis, it is more commonly expressed in relation to pseudorapidity, η = -ln(tan(θ/2)). η is an approximation of rapidity[3], y, in which zero particle mass is assumed, i.e. in the high-energy limit. η is a preferred coordinate in particle physics because particle production from the interaction point is approximately constant as a function of η

The impact parameters d_0 and z_0 are respectively the transverse distance to the beam axis and the z position of a track, both measured at the point of closest approach [32].

3.2.2 The Inner Detector

The innermost component of the ATLAS detector is the Inner Detector (ID), contained within the central solenoid magnet which provides a nominal magnetic field of 2 T. As mentioned above, the magnetic field bends the trajectory of charged particles passing through the ID and thus allows measurements of particle momentum and charge.

The ID consists of three subcomponents, moving out from the centre they are; silicon pixel detectors, semiconductor tracking (SCT) detectors and transition radiation (TRT) detectors. The arrangement of the inner detector subcomponents is shown in Figure 3.4. The LHC produces very high track den-

[2]Transverse quantities are used because in LHC collisions there will be momentum along the beam axis left over from the beam particles (since protons are composite particles). So the transverse quantities will give the only reasonable measure of objects from interacting partons.

[3]Rapidity is related to the energy and scalar momentum of a particle of non-zero mass by $y = \frac{1}{2} ln \frac{E+p_z c}{E-p_z c}$, where p_z is the momentum along the beam axis.

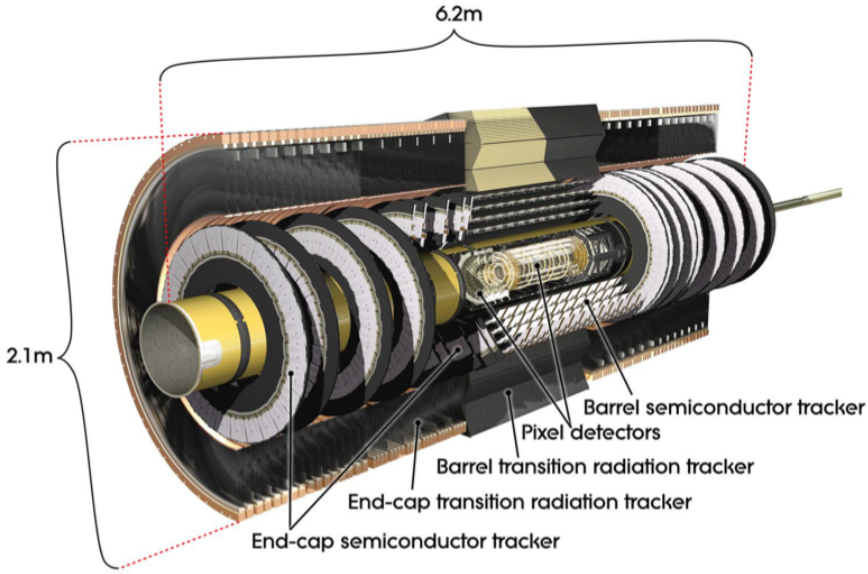

Figure 3.4: Schematic of the ATLAS Inner Detector [33].

sities at the interaction points, therefore the fine-granularity pixel and SCT detectors are employed at the inner radii to ensure high resolution for momentum and vertex measurements. The TRT provides continuous tracking in the outer radii of the ID. The combination of detectors in the ID facilitates high precision momentum measurements, pattern recognition and both primary and secondary vertex measurements for charged tracks above a nominal P_T threshold of approximately 0.5 GeV. In addition, the ID provides electron identification over $|\eta|< 2$ and between energies of 0.5 GeV and 150 GeV [34]. The ID covers an angular range of $|\eta|\geq 2.5$ [35].

3.2.2.1 The Pixel Detector

Designed to provide high precision measurements, the Pixel Detector lies in the region closest to the interaction point. This highly modular detector consists of 1744 silicon-pixel sensors, each sensor contains 47232 pixels, has a thickness of 250 μm, and dimensions 19×63 mm. 90% of the pixels are of nominal size 50×400 μm, the remainder lie in the regions of the front-end readout chips on the pixel sensor and are larger (50×600 μm). The pixel sensors are overlapped

and mounted on staves which are arranged to form thee concentric barrels at radii 50.5, 88.5 and 122.5 mm, thus providing three precision measurements per particle track. The $|\eta|<2.5$ angular coverage of the pixel detector is completed with end-caps on each side of the barrel.

The fine-granularity of this section of the ID determines the resolution on the impact parameters (z_0 and d_0) and the ability to detect the secondary vertexes from the decay of short-lived particles, such as B hadrons and τ-leptons (important for heavy flavour and τ-tagging respectively) [36].

3.2.2.2 The Semiconductor Tracker

Surrounding the Pixel Detector are a series of silicon micro-strip detectors that comprise the Semiconductor Tracker (SCT). The SCT is built from 4088 modules, the modules consist of four silicon detectors of dimension 636×640 mm, with a thickness of 285±15 μm and a strip pitch of 80 μm. On each module, two silicon detectors are aligned in the azimuthal angle, ϕ, that provide measurements in $R-\phi$. Two such pairs are set back-to-back at a stereo angle of 40 mrad to provide a measurement in z. The spatial resolution of each module in the barrel is 17 μm in $R-\phi$ and 580 μm in z, the resolution in the end-caps is 17 μm in $R-\phi$ and 580 μm in R [37]. The double-sided modules are arranged on four concentric carbon fibre cylinders that carry the cooling system, at radii of 299, 371, 443 and 514 mm. This forms 8 silicon detector layers providing 8 measurements per particle track [38]. End-caps complete the $|\eta|<2.5$ angular coverage of the SCT.

The SCT provides precision track measurements in the $R-\phi$ and z coordinates, and contributes to the measurements of the Pixel Detector. Together the two sub-detectors are referred to as the Precision Tracker [39].

3.2.2.3 Lorentz Angle in The SCT

As mentioned in the previous section, the Inner Detector is surrounded by a solenoid magnet that produces a nominal magnetic field of 2 T. The presence of a very strong magnetic field means that charge-carrying particles passing through the silicon detectors in the SCT will experience a Lorentz force, causing them to drift. The Lorentz angle, ϕ_L, is the angle by which the charge carriers are deflected. It is dependent on their mobility and the size of the external magnetic field. For a magnetic field B, ϕ_L is expressed as:

$$tan\phi_L = \mu_H B = \gamma \mu_d B \tag{3.1}$$

where μ_H is the Hall mobility[4], μ_d is the drift mobility of the charge carrier and γ is the Hall factor (of the order 1). The mobility is dependent on the bias voltage of the silicon sensors and their temperature, ϕ_L is therefore also dependent on these quantities. Theoretical values for ϕ_L, for SCT layers 0, 1 and 2 (which have a temperature -2°C) and layer 3 (at 4.5°C), are 3.88°±0.28° and 3.71°±0.27° respectively. These predictions were reached via the Jacoboni-Calani model for drift mobility [40, 41].

When a charged particle passes through the SCT, the number of adjacent strips (per layer and per module) that are hit is known as the cluster size. For a zero magnetic field this quantity should be at a minimum when the incident angle, ϕ, is zero (ϕ is measured in the plane defined by the normal to the wafer and the axis perpendicular to the strip direction). When a magnetic field is present and the Lorentz force causes the charged particles to drift, the cluster size minimum will no longer be at zero, rather at ϕ_L. The Lorentz angle can thus be extracted by considering the mean number of strip hits in an event, i.e. the cluster width, against ϕ and performing a fit to find the value of ϕ for

[4]Mobility is a quantity that characterises how quickly an electron or hole (the mathematical opposite of an electron, i.e. the absence of an electron) can move through a metal or semiconductor. Mobility is most commonly measured via the Hall effect, and the resultant measurement known as the Hall mobility.

which the cluster width is minimum.

Track Selection: The track selection on data was designed to be loose to ensure a statistically significant sample of good quality tracks. The drift direction of charged particles passing through the silicon detectors in the SCT end-cap modules is almost perpendicular to the magnetic field. Therefore, the Lorentz force experienced by a particle in the end-caps, and the resultant drift, will be negligible. For this reason only tracks in the barrel were included in the data to be fitted. The track selection was as follows:

- Track $P_T > 500$ MeV.
- $|d_0$ with respect to the primary vertex$|<$ 1mm.
- At least 7 hits in the SCT barrel.
- At least 1 hit in the Pixel Detector.
- Negatively charged tracks only: due to the angle at which the silicon sensors are tilted with respect to the beam axis, only negative tracks have a minimum in cluster size. Positive tracks will have an incident angle greater than zero.

Silicon Sensors of Differing Crystal Orientation: The majority of modules in the SCT are comprised of silicon sensors with <111> crystal orientation (see Figure 3.5). However, a small number of modules (93) have sensors with <100> orientation. The latter have a fairly even distribution in η throughout the SCT barrel. Figure 3.6 is an $\eta - \phi$ map showing the position of the sensors with <100> crystal orientation. Due to the different orientation of the silicon crystal plane, it is expected that the Lorentz angle for <100> sensors will be different than for <111> sensors. The data sample was split into two subsamples: those with <111> sensors and those with <100> sensors. The Lorentz angle was extracted separately for each.

Fit: The fitting function used to find the minimum of the cluster width (the distribution is as a function of ϕ) was an empirical function used in previous studies [42], and took the form:

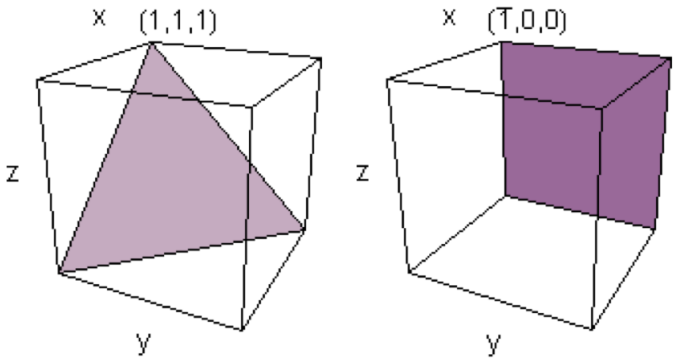

Figure 3.5: <111> and <100> crystal orientations.

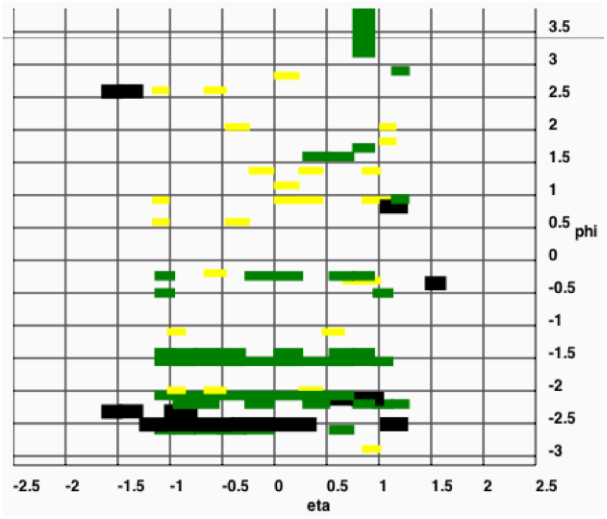

Figure 3.6: $\eta - \phi$ map showing the position of the SCT modules with silicon sensors of <100> crystal orientation. Black: Layer 0; Green: Layer 2; Yellow: Layer 3.

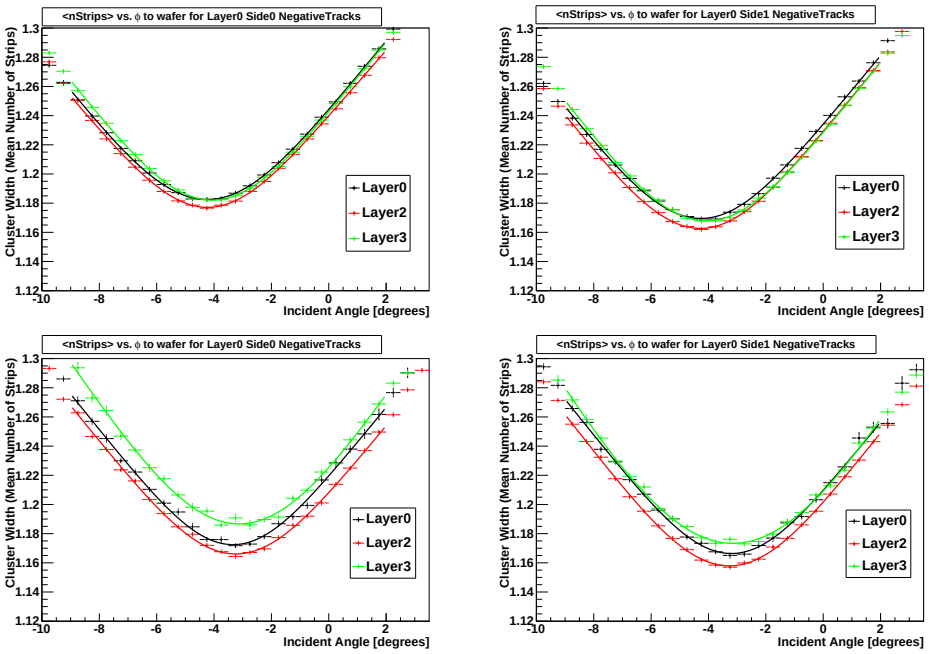

Figure 3.7: Fits to cluster width vs incident angle for silicon modules in the three layers of the SCT barrel. Left: Side 0; Right: Side 1; Top: <111> modules; Bottom: <100> modules.

$$\begin{aligned} f(\phi) &= (a|\tan\phi - \tan\phi_L| + b) \otimes \text{Gaussian}(\phi) \\ &= \int_{-\infty}^{infty} (a|\tan\phi - \tan\phi_L| + b) \frac{1}{\sqrt{2\pi}\sigma} exp(-\frac{(\phi - \phi')^2}{2\sigma^2}) d\phi' \end{aligned} \tag{3.2}$$

where ϕ_L, a, b and σ are four free parameters of the fit, corresponding to the Lorentz angle, the gradient of the distribution, the minimum cluster width and the smearing effect (from diffusion of electric charge in the silicon modules) respectively. The fit was performed between a ϕ range of [-9, 2] degrees. The choice of fit range was arrived at following an optimisation study described in [42]. As mentioned above, the SCT barrel modules are arranged on double sided staves in three concentric layers, therefore the fit was performed separately for each side and layer, yielding a separate Lorentz angle for each. Figure 3.7 shows the fits for the sample of <111> and <100> modules.

Systematic Uncertainty: A systematic uncertainty on this method was derived by performing the analysis on data from cosmic rays passing through

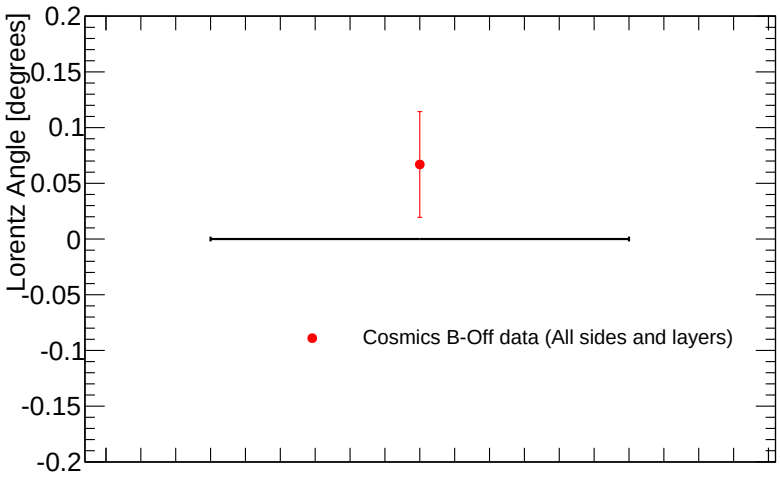

Figure 3.8: Lorentz angle result for cosmic ray data taken when he magnetic field was off. The fit was performed on a combined profile of all sides and layers. The error bar on this measurement is the statistical error from the fit.

the detector when the magnetic field was turned off. Under these conditions, the Lorentz angle is expected to be zero across all sides and layers. Therefore, the offset from zero of the result obtained by fitting to this data can be taken as a systematic uncertainty on the procedure of the Lorentz angle extraction. Cosmic ray data from all SCT sides and layers were combined to increase statistics and the fit was performed as described above. The Lorentz angle extracted from the fit is shown in Figure 3.8, a clear offset from zero can be seen. From this result, two systematic bounds were considered; a lower bound which corresponded to the offset of the data point from 0 (7%) and a more conservative upper bound corresponding to the offset of the upper statistical error band on this result from 0 (11.5%).

Lorentz Angle Results: Figure 3.9 shows the values of the Lorentz angle extracted for each side/layer and for <111> and <100> modules, with the lower and upper systematic uncertainty bands. The Lorentz angle values do not agree well with the model prediction. Only a few data points are just consistent with the model within the upper systematic band. It is understood that

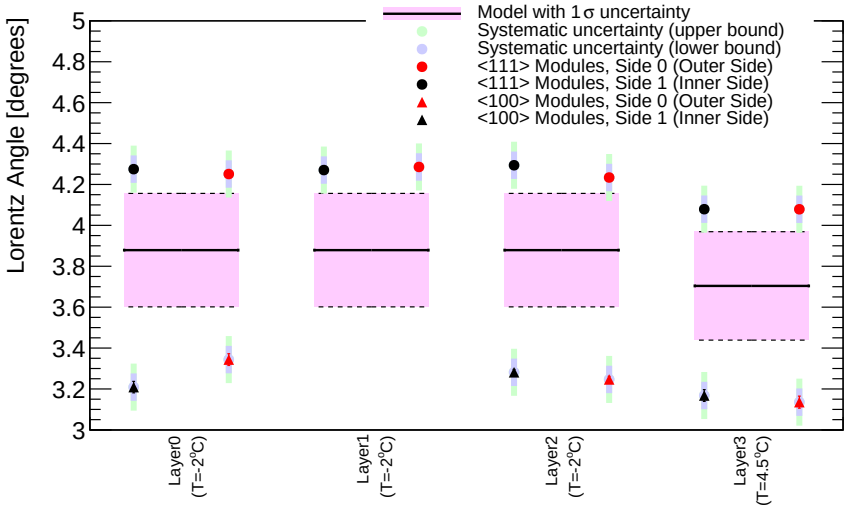

Figure 3.9: Lorentz angle results for separate sides and layers, and for <111> and <100> modules. The systematic uncertainty band is derived from the study on cosmic ray events

the Jacoboni-Canali model is applicable only for silicon with <111> crystal orientation and inadequately describes the drift mobility for <100> sensors. The remaining large discrepancy between the Lorentz angle for <111> sensors and the Jacoboni-Canali model prediction is yet to be understood. A separate study using a different model for mobility (the Becker-Fretwurst-Klanner model [43]) has been conducted. The Becker-Fretwurst-Klanner model is applicable to both <111> and <100> sensors, but large discrepancies with data are still observed for the Lorentz angle[5]. The large amount of data provided by the LHC presents a unique opportunity for deeper understanding of the predictions mentioned above.

3.2.2.4 The Transition Radiation Tracker

The final component of the Inner Detector is the Transition Radiation Tracker (TRT). The TRT is based on straw drift tube detectors: 4 mm diameter tubes filled with a gas mixture of 70% Xe, 27% CO2 and 3% O2. Each tube acts as the cathode and contains a coaxial anode; tungsten wire of 31 μm diam-

[5]Studies are ongoing to understand the discrepancies, including interaction with the authors of both predictions.

eter plated with 0.5-0.7 μm of gold. Approximately 50,000 straws, 144 cm in length, are arranged around the barrel in 36 layers (providing 36 measurements) between radii of 554 and 1082 mm, and are embedded in a matrix of polypropylene fibres [44].

A charged particle passing through the straw will ionise the gas within, allowing drift time measurements of the liberated electrons to the central anode. In this way, each straw of the TRT provides a spatial resolution of 130 μm. Charged particles with relativistic energies passing from one material to another, with a different refractive index, undergo a change in velocity and produce transition radiation in the form of photons. In this way, a particle passing through the TRT from the drift straws to the polypropylene fibres will emit transition radiation. The amount of radiation emitted is proportional to the change in velocity of the particle and as such can be used to identify type of particles, e.g. an electron passing through the TRT will produce more radiation than a hadron. The output electronic channels of the TRT have two independent thresholds; a lower threshold used for tracking hits, and a higher threshold used to identify photons from transition radiation.

Despite the coarser granularity (with respect to the Pixel Detector and the SCT) and thus lower precision of the subdetector, the TRT contributes to the tracking and momentum measurements of the Inner Detector, by providing a large surface area which increases the track length and the number of hits in the detector. The ability of the inner detector to identify electrons is augmented by measurements of transition radiation.

3.2.3 Electromagnetic Calorimeter

The ATLAS calorimetry is divided into two major subdetectors; the Electromagnetic Calorimeter (ECal) and the Hadronic Calorimeter (HCal). Closest to the interaction point, the ECal consists of alternating layers of absorber and detector material, lead and liquid argon (LAr) respectively. The layers

are arranged in an accordion-shaped geometry, providing full symmetry in ϕ without azimuthal cracks.

When a charged particle traverses the absorber material, it loses energy via Bremsstrahlung radiation due to deflection in atomic fields. Photons emitted via Bremsstrahlung will interact with the detector atoms and lose energy via production of e^+e^- pairs, which will in turn cause ionisation in the LAr volume. This process continues as a cascade of increasingly low energy photons and electrons, yielding an electromagnetic shower across many layers of the ECal.

The ECal covers the η range $|\eta|< 3.2$ and, as for the ID, is divided into barrel ($|\eta|< 1.475$) and end-cap ($1.375 < |\eta|< 3.2$) components. The barrel is comprised of two half barrels separated by a gap of 4 mm at z=0. It has a constant LAr gap thickness of 2.1 mm and a total thickness of over 24 radiation lengths (X_0). Each end-cap consists of two coaxial wheels, the LAr gap thickness increases with radius and the total thickness of the end-caps is over 26 X_0. There is a large amount of non-sensitive material at the boundary between the ECal barrel and end-caps. This is defined as the "crack region" of $1.37 < |\eta|< 1.52$ and is excluded from the electron channel selection of this measurement (full details are given in Chapter 4).

The region of precision physics in ATLAS is $|\eta|< 2.5$, in this region the ECal is segmented into three longitudinal sampling sections. The $\Delta\eta \times \Delta\phi$ granularity of the sampling sections is 0.003×0.01, 0.025×0.025 and 0.05×0.025 [45]. The first of these sections is known as the strip section, it acts as a pre-electromagnetic shower detector to enhance the separation in identification between γ/π^0 and e/π and provide precision position measurements.

Preceding the ECal is a pre-sampling detector which consists of a LAr layer of 1.1 mm thickness in the barrel and 0.5 mm in the end-caps. This acts to correct for the energy lost by a charged particle in the material between the interaction point and the front face of the ECal (a distance of around $2X_0$ for $|\eta|< 1.8$) [45].

3.2.4 Hadronic Calorimeter

Surrounding the ECal is the Hadronic Calorimeter (HCal), designed to measure hadronic activity in the detector. The HCal covers the η range $|\eta|< 4.9$ and consists of three subcomponents; a scintillating tile barrel, LAr hadronic endcaps (HEC) and a forward calorimeter (FCal, also made of LAr). The tile barrel, HEC and FCal cover η ranges of $|\eta|< 1.0$, $1.5 < |\eta|< 3.2$ and $3.1 < |\eta|< 4.9$ respectively. An extension to the tile barrel covers the range $0.8 < |\eta|< 1.7$.

The HCal works on a similar principle as the ECal, consisting of alternating layers of absorber and active material. The former produces particle interactions, resulting in cascades that are measured by ionisation of the latter. Hadrons interact with the absorber material via the strong force producing a cascade of hadrons. The resultant hadronic showers are larger than the electromagnetic equivalent. The HCal must be thick enough to contain hadronic showers and reduce punch-through radiation into the Muon Spectrometer. The HCal has a thickness of 11 radiation lengths (λ), sufficient to provide good resolution for high energy jets.

The tile region of the HCal is designed to provide precise measurements of the angle and energy of hadronic jets. The tile barrel extends from a radius of 2.28 to 4.25 mm from the interaction point and consists of alternating layers of iron absorber and plastic scintillating tiles of 3mm thickness. Two sides of the scintillating tubes read out to photomultiplier tubes by wavelength-shifting fibres. As in the ECal, the tile barrel is segmented into three longitudinal sampling layers of 1.4, 4.0 and 1.8 λ, and $\Delta\eta \times \Delta\phi$ granularity of 0.1×0.1, 0.1×0.1 and 0.2×0.1 [46].

The HEC consists of two independent wheels positioned behind each endcap, and built from 32 identical wedge-shaped modules. The modules in the wheel closest to the interaction point are made from 25 mm copper plates, the outer wheel is made from 50 mm copper plates. The gap between the two

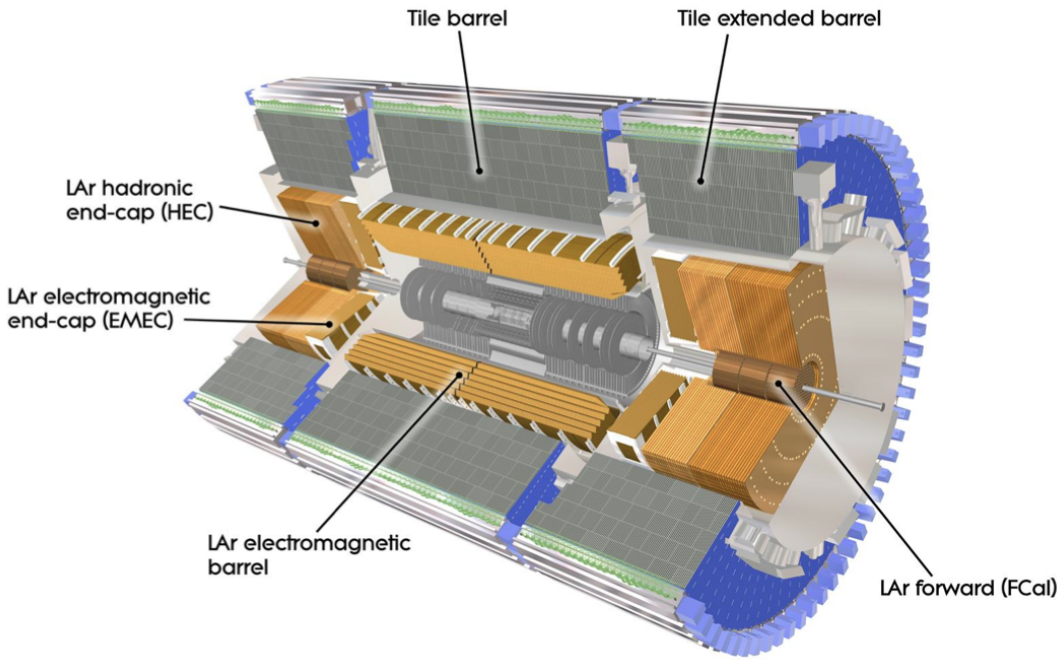

Figure 3.10: Schematic of the ATLAS Calorimetry [47].

wheels is 8.5 mm and filled with LAr. Each of the wheels is divided into two longitudinal segments of granularity; 0.1×0.1 for $1.5 < |\eta| < 2.5$, and 0.2×0.2 for $2.5 < |\eta| < 3.2$ [46].

The forward calorimeter (FCal) covers an η range of $3.1 < |\eta| < 4.9$. The front end of the FCal is positioned 4.7 m from the interaction point. The FCal consists of three modules; the first is made of copper and the remaining two are made of tungsten, designed to measure electromagnetic and hadronic activity respectively. Each module is a matrix of the relevant material, with regularly spaced gaps filled with high positive voltage rods and grounded tubes, and LAr in the gaps between. The FCal is used, among other measurements, to observe forward jets in ATLAS. The FCal occupies a small volume within ATLAS, this is compensated for by high density material. The FCal has a thickness of 10 λ.

Figure 3.10 shows a schematic of the ATLAS calorimetry, indicating the position of the components discussed above.

3.2.5 Muon Spectrometer

The outermost component of ATLAS is the Muon Spectrometer, designed to detect and make measurements of muons that traverse the preceding parts of the detector whilst losing little energy. The Muon Spectrometer combines a system of superconducting toroidal magnets with high precision muon tracking ionisation chambers.

The magnet system provides a magnetic field that is mostly orthogonal to the trajectory of the muon. Measurements of the momentum and charge of a muon passing through the Muon Spectrometer are made on the same principle as those of charged particles passing through the ID. The magnetic field serves to bend the trajectory of a muon as it traverses the spectrometer, the track curvature and direction yield the momentum and charge of the muon. The magnets are divided into two sections; the large barrel toroid which covers an η range of $|\eta| < 1.0$, and the end-cap toroids covering $1.4 < |\eta| < 2.7$. In the intermediate region between the barrel and end-cap toroids ($1.0 < |\eta| < 1.4$) muons are bent by both [48].

The tracking chambers in the barrel of the Muon Spectrometer cover $|\eta| < 1.0$ and are arranged in three concentric cylinders around the beam pipe at radii of 5, 7.5 and 10 m. The end-cap tracking chambers cover $1.0 < |\eta| < 2.7$ and are arranged vertically in four disks at 7, 10 and between 21-23 m from the interaction point. The tracking chambers are of four types: Monitored Drift-Tube chambers (MDTs), Cathode Strip Chambers (CSCs), Resistive Plate Chambers (RPCs) and Thin Gap Chambers (TGCs). The MDTs and CSCs are used for precision tracking, whereas the RPCs and TGCs are used for triggering in the barrel and end-caps respectively.

The MDTs cover an η range of $|\eta| < 2.7$ and provide precision muon track measurements. They consist of 30 mm diameter aluminium tubes of 400 μm thickness filled with a mixture of 93% Ar and 7% CO_2, with a coaxial tungsten-rhenium anode wire. The MDTs have a spatial resolution of 35 μm in z and

measure the coordinates of the muon in the plane of bending. The CSCs are positioned close to the interaction point and cover $2.0 < |\eta| < 2.7$. They are equipped with high granularity to withstand the high particle flux in this region of the detector. They are multi-wire proportional chambers filled with a mixture of 80% Ar and 20% CO_2 and achieve a spatial resolution of 50 μm in the plane of bending [49].

The RPC and TGC trigger chambers serve a number of purposes; to identify bunch-crossing, to trigger with a well defined P_T and to measure a second muon spatial coordinate in a direction orthogonal to that measured by the chambers upstream [50]. The RPCs cover $|\eta| < 1.05$ and provide triggering for the Muon Spectrometer barrel. Like the MDTs, the RPCs are arranged in three concentric cylinders to provide measurements within the magnetic field and at the inner and outer field boundaries. The RPCs have a spatial resolution of 10mm in z and ϕ. The TGCs cover $|\eta| > 1.4$ and are positioned in the end-caps. The position of the magnet cryostats in this region prevents measurements inside the field volume, therefore the chambers are arranged to perform a point-like measurement to determine muon momentum. The spatial resolution of the TGCs is between 2-6 mm in R and between 3-7 mm in ϕ.

Figure 3.11 is a schematic in which the position of the various Muon Spectrometer components is shown.

3.2.6 Trigger System

When operating at design conditions, the LHC produces events at a rate of around 40 MHz. This rate of data generation is too high for everything to be recorded, therefore ATLAS employs a trigger system to reduce the rate of data taking to a manageable level, at which data can be permanently recorded. The general principle of the ATLAS trigger system is to reduce the rate of selected events from 40 MHz to around 200 Hz by rejecting "uninteresting" events, while retaining high trigger efficiencies for physics processes that are

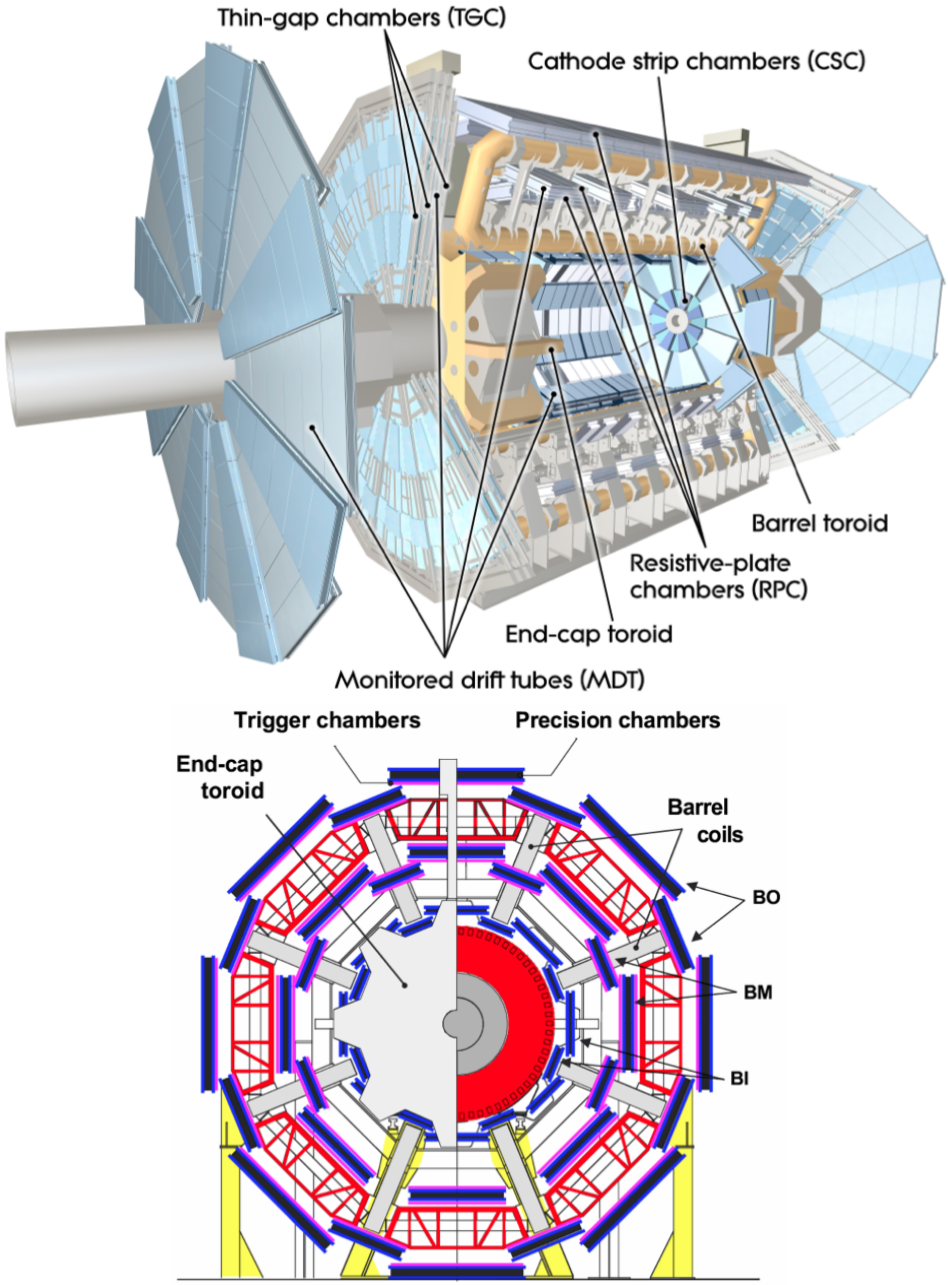

Figure 3.11: Schematic of the ATLAS Muon Spectrometer showing the position of the muon chambers (top) [51] and their arrangement in the x-y plane (bottom) [52].

part of the ATLAS physics programme. The ATLAS trigger system is based on three levels of online event selection; the hardware-based Level 1 (L1), and the software-based Level 2 (L2) and Event Filter (EF). The latter two are collectively known as the High Level Trigger (HLT). Each trigger level refines the event selection by using more detailed detector information and taking more time to make the decision of which events to keep and which to discard.

The hardware-based L1 trigger reduces the rate to about 75 kHz by making an initial decision based on reduced granularity information from a subset of detectors. Information from the calorimeters are used to search for high P_T electrons, photons, jets and taus, in addition to large E_T and E_T^{miss}. High P_T muons are searched for using information from the RPC and TGC trigger chambers in the Muon Spectrometer, as mentioned in Section 3.2.5. The L1 trigger defines a Region of Interest (RoI) in $\eta-\phi$ space around a selected object and this information is seeded to the L2 trigger. Measured from the time of collisions to the time of the trigger decision, the L1 trigger has a latency period of approximately 2μs [53].

The L2 trigger refines the decision made by the L1 trigger by using full detector information to partially reconstruct events within the RoI and reduce the rate to approximately 3.5 kHz. The selection rate for electrons is reduced by requiring a match between a high P_T track in the ID and one in the electromagnetic calorimeter. The muon selection rate is reduced by using the ID and the precision muon chambers to sharpen the muon P_T threshold. The latency period for the L2 trigger is approximately 40 ms [53].

The final level of the trigger system is the Event Filter (EF) which further refines and finalises the selection of physics objects from information seeded from L2 and reduces the rate to around 200 Hz. The EF employs offline algorithms adapted to an online environment, to allow for a near-full event reconstruction, and has a latency period of around 4 s [53]. Events passing the EF are then written to tape and stored for offline analysis.

The ATLAS trigger system has a central trigger processor which imple-

ments a "trigger menu". The menu is a number of different triggers, each of which designed to select specific physics objects. The final data rate of 200 Hz is split among each of triggers on the menu. Due to limitations in bandwidth many triggers are prescaled, i.e. only a fraction of the events that pass the trigger are stored.

For the analysis presented in this thesis, separate triggers were used to select electron and muon candidate events. The exact trigger used for each selection was dependant on data taking period (more details in Section 4.2). For electron candidate events the triggers used selected events with at least one electron. Electron candidates were also required to have P_T of at least 20 GeV (or 22 GeV, depending on data taking period) at the EF. Muon candidate events were triggered on by requiring at least one muon with P_T of at least 18 GeV at the EF.

Chapter 4

Detector Level Study of W+jets and Z+jets

The data used in this analysis were collected by the ATLAS detector during proton-proton collisions conducted at a centre of mass energy of 7 TeV throughout the 2011 LHC data taking run. This dataset corresponds to an integrated luminosity of 4.6 fb^{-1}. Data was collected during periods of stable beam operation, with all ATLAS sub-detectors and magnets (detailed in the previous section) fully operational. A good run list (GRL) [54] was implemented as part of the event selection. It was required that the only runs used were those during which all parts of the detector relevant to the analysis were in stable operation. The GRL was common to $W \to l\nu$ + jets and $Z \to ll$ + jets selections in both the electron and muon channels.

4.1 Monte Carlo Simulation

Monte Carlo simulations were used in this analysis to model $W \to l\nu$ + jets and $Z \to ll$ + jets signal processes, and to subtract the contribution of certain background processes that still contaminate the data selected. Among the background processes are other electroweak decays, whereby W+jets or Z+jets events decay to a final state with a tau lepton ($W \to \tau\nu, Z \to \tau\tau$). These pro-

cesses contribute a source of fake leptons, either through the mismeasurement of jets or leptonic tau decays. Another electroweak background are di-boson events (those with WW, ZZ, WZ). Di-boson processes contribute a source of background via missed extra leptons and also through jet mismeasurement.

Monte Carlo was also used for the simulation of $Z \to ll$ events that are present as a background to the $W \to l\nu$ selections. Fake E_T^{miss} can occur in an event if a lepton is not reconstructed due to trigger or detector inefficiencies. A lepton can also be missed if outside the detector acceptance. $W \to l\nu$ events were also treated as a background to the $Z \to ll$ selections.

$W \to l\nu$ + jets and $Z \to ll$ + jets signal processes (and $W \to \tau\nu, Z \to \tau\tau$ backgrounds), were simulated using ALPGEN v2.13 [22] interfaced with HERWIG v6.520 [18] (to provide the parton shower) and to JIMMY v4.31 [21] (to model the contribution from the underlying event, using the AUET2-CTEQ6L1 tune [55]). CTEQ6L1 [23] PDFs were employed and the PHOTOS program [56] was used to simulate final state QED radiation in ALPGEN. Di-boson processes were simulated using HERWIG with the AUET2-LO** (MRSTMCal) tune [55]. Signal samples for V+jets processes generated using SHERPA v1.40 with CT10 [25] PDFs were also used for comparison to the ALPGEN signal samples[1].

Events with a single top quark in the final state present a small source of background contamination to the signal sample. Single top backgrounds (including Wt production) were simulated using ACERMC [57] interfaced with PYTHIA [58].

As discussed in Section 2.6, all samples were passed through the GEANT4 full simulation of the ATLAS detector and trigger. The full analysis selection described in Section 4.2 was then applied to each of the samples, after which they were normalised to data luminosity (4.6 fb^{-1}). Table 4.1 presents an overview of the Monte Carlo samples use in this analysis.

All Monte Carlo samples were normalised to the inclusive cross-section from

[1]SHERPA differs from ALPGEN in that it has a self contained parton shower algorithm.

Process	Generator	Cross-section (nb)	$\int \mathcal{L}$ (fb^{-1})	Note
$W \to e\nu$	ALPGEN(+HERWIG)	10.46	0.84/3.19/8.30/8.29/24.0/50.0	
$W \to \mu\nu$	ALPGEN(+HERWIG)	10.46	0.84/3.19/8.30/8.29/24.0/50.0	
$W \to e\nu$	SHERPA, v1.4	10.46	1.91	
$W \to \mu\nu$	SHERPA, v1.4	10.46	1.91	
$W \to \tau\nu$	ALPGEN(+HERWIG)	10.46	0.41/1.60/8.26/8.28/8.06/7.74	
Z/$^*\gamma\to ee$	ALPGEN(+HERWIG)	1.07	7.92/7.95/39.42/41.65/48.19	M_{ll} >40GeV
Z/$^*\gamma\to \mu\mu$	ALPGEN(+HERWIG)	1.07	7.92/7.95/39.42/41.65/48.19	M_{ll} >40GeV
Z/$^*\gamma\to ee$	SHERPA, v1.4	1.07	9.34	M_{ll} >40GeV
Z/$^*\gamma\to \mu\mu$	SHERPA, v1.4	1.07	9.34	M_{ll} >40GeV
Z/$^*\gamma\to \tau\tau$	ALPGEN(+HERWIG)	1.07	12.71/19.82/19.82/36.42/40.28/43.27	M_{ll} >40GeV
WZ	HERWIG	17.5x10^{-3}	459.27	
ZZ	HERWIG	6.49x10^{-3}	57.17	
WW	HERWIG	4.50x10^{-2}	182.48	
$t\bar{t}$	ALPGEN(+HERWIG)	0.1773	21.8/15.6/9.8/52.5/63.4/30.0 (lep. lep.)	
			15.8/25.6/9.3/84.0/9.0/8.6 (lep. had.)	
Single top, t-channel	ACER+PYTHIA	6.97x10^{-3}	28.68	
Single top, s-channel	ACER+PYTHIA	5.0x10^{-4}	1998.59	

Table 4.1: Monte Carlo samples of simulated events used in this analysis. Effective luminosities for those samples with separate components for different numbers of partons (0-5) are shown where necessary.

the highest-order pQCD calculation available. The value of each cross-section is given in Table 4.1.

4.2 Event Selection

A strong motivation for performing a $\frac{\text{W+jets}}{\text{Z+jets}}$ ratio analysis with respect to individual cross-section measurements is the cancellation of experimental systematic uncertainties. Therefore, a guiding principe of the event selection was consistency (where possible) across both lepton channels for both W$\to l\nu$ + jets and $Z \to ll$ + jets events. The selection of W$\to l\nu$ + jets events was

defined to achieve the largest possible fiducial coverage in the ATLAS detector for electrons, muons and jets. The selection of $Z \to ll$ + jets events was defined in a similar way in order to synchronise the cancellation of experimental uncertainties when forming the ratio of $\frac{\text{W+jets}}{\text{Z+jets}}$ events.

Before any lepton selection a general preselection was applied to each event, requiring at least one primary vertex[2] with at least three associated tracks. The initial vertex requirements were to ensure a reduction of non-collision backgrounds.

The liquid argon (LAr) calorimeters can sometimes have short noise bursts during data taking. Events for which this is the case were also removed as part of the preselection. These events affect data only and were removed individually rather than incorporated into the GRL. A correction is then applied for the missing events, such that no bias in luminosity is introduced.

The following sections detail the selection criteria for electrons, muons, W and Z bosons, and jets. The event selection is summarised in Tables 4.3 and 4.4. The number of events predicted by Monte Carlo and data-driven background estimations (described in Chapter 5) are compared with the total number of events observed in data in Tables 4.5 and 4.6.

4.2.1 Electron Selection

Electrons are reconstructed in the ATLAS detector by matching clusters of energy deposited in the electromagnetic calorimeter to tracks formed in the inner detector. In this analysis, electrons candidates were reconstructed following the "tight++" identification criteria which imposes various cuts on electron objects including track quality (e.g. the minimum number of hits in various parts of the inner detector). The "tight++" criteria also includes requirements on the shape of the electromagnetic shower in the calorimetry, and the

[2]The primary vertex is the scattering vertex with the highest P_T sum of all associated tracks in an event.

aforementioned track-cluster matching. The full definition of the "tight++" selection is detailed in [59].

Triggers were applied to select electron candidate events with at least one reconstructed electron object in the event. The trigger also required that the electron candidates have transverse energy of at least 20 GeV for data taking periods D-I and 22 GeV for periods K-M. The same triggers were used for both W$\rightarrow e\nu$ and $Z \rightarrow ee$ selections. The specific electron triggers employed for different data-taking periods are shown in Table 4.2.

In both lepton channels, fiducial volume cuts were applied for the selection of leptons; a requirement on the transverse momentum, P_T, ensured that the event was above the trigger turn on curve and lies on the trigger efficiency plateau. An $|\eta|$ requirement ensured that the lepton was within the acceptance of the inner detector. For this analysis, the electron fiducial requirements were $P_T > 25$ GeV and $|\eta| < 2.47$, excluding the electromagnetic calorimeter barrel-end-cap transition region of $1.37 < |\eta| < 1.52$.

Also for both lepton channels, events with multiple jets will produce leptons in the final state from semileptonic hadronic decays. Such leptons will not be isolated, rather accompanied by hadronic activity in the detector. To reduce these background processes, isolation requirements were applied to the leading lepton (defined as that with the largest P_T) for the W$\rightarrow l\nu$ event selection, and the two leading leptons for the selection of $Z \rightarrow ll$ events. In the electron channel this took the form of a combination of calorimeter and track-based isolation requirements, each of which was dependent on the P_T and η of the leading electron.

4.2.2 Muon Selection

This analysis employed the STACO algorithm [60] to reconstruct muons. This algorithm matches and combines inner detector (ID) and muon spectrometer (MS) tracks by a statistical averaging of the ID and MS track parameters

Selection	Triggers
W$\rightarrow e\nu$	e20 medium (D-I), e22 medium (K), e22vh medium1 (L-M)
Z$\rightarrow ee$	e20 medium (D-I), e22 medium (K), e22vh medium1 (L-M)
W$\rightarrow \mu\nu$	EF mu18 MG or EF mu18 (D-I), EF mu18 MG medium or EF mu18 medium (J-M)
Z$\rightarrow \mu\mu$	EF mu18 MG or EF mu18 (D-I), EF mu18 MG medium or EF mu18 medium (J-M)

Table 4.2: Electron and muon triggers used for the W$\rightarrow l\nu$ and Z$\rightarrow ll$ event selection. The letters in brackets refer to the data-taking period.

[61]. As with the electron selection, various quality requirements were placed on candidate muons, such as a minimum amount of hits in the sub-detectors (detailed in full in [61]). Muon triggers requiring at least one muon with transverse momentum of at least 18 GeV were applied, the exact trigger dependent on data taking period. As in the electron channel, the same triggers were used for both W$\rightarrow \mu\nu$ and $Z \rightarrow \mu\mu$ selections (see Table 4.2). The fiducial volume cuts on the P_T and $|\eta|$ of muon candidates were $P_T > 25$ GeV and $|\eta| < 2.4$.

Track-based isolation requirements were applied in the muon channel with the same motivation as for those in the electron channel. A cone was defined around the leading muon, with $\Delta R \equiv \sqrt{(\Delta\phi)^2 + (\Delta\eta)^2} = 0.2$. For the muon to pass the isolation cut, the sum of the P_T of all tracks within the cone had to be less than 10% of the P_T of the leading muon, i.e $\Sigma P_T^{cone20}/P_T^{\mu} < 0.1$. A further isolation cut was applied to the leading muon, requiring that the impact parameter significance was $|d_0/\sigma(d_0)| < 3.0$, where d_0 is the impact parameter with respect to the primary vertex, and $\sigma(d_0)$ is its uncertainty.

4.2.3 W$\rightarrow l\nu$ events

Since neutrinos pass through the ATLAS detector without causing any ionisation, their existence in an event can only be inferred through the existence of missing transverse energy (E_T^{miss}) in the final state. It is therefore not possible to reconstruct the W mass peak by calculating the invariant mass of the two

decay products. Instead, a different quantity, the transverse mass (M_T) of the lepton and the missing energy, is used to reconstruct W boson candidates. M_T is defined by the P_T and direction of both the lepton and the missing momentum, and is given by the expression:

$$M_T = \sqrt{2P_T^l P_T^\nu (1 - cos(\phi^l - \phi^\nu))} \tag{4.1}$$

where P_T^ν is the E_T^{miss} in the event and ϕ^ν its ϕ component. Events passed the W$\rightarrow l\nu$ selection if they had $E_T^{miss} > 25$ GeV and $M_T > 40$ GeV. Distributions for the transverse mass, E_T^{miss} and the transverse momentum of the selected W in the electron channel are shown in Figure 4.1.

4.2.4 $Z \rightarrow ll$ events

Z$\rightarrow ll$ candidate events were required to have exactly two oppositely charged leptons of the same flavour. Unlike W$\rightarrow l\nu$, both decay products from Z$\rightarrow ll$ events can be identified in the volume of the detector, so the Z mass peak can be reconstructed by calculating the invariant mass, M_{ll}, of the two final state leptons, given by the formula:

$$M_{ll} = m_{l_1}^2 + m_{l_2}^2 + 2(E_{l_1}E_{l_2} - \vec{p_{l_1}} \cdot \vec{p_{l_2}}) \tag{4.2}$$

The invariant mass for the Z selection was required to be $66 \leq M_{ll} \leq 116$ GeV. All lepton pairs were also required to be separated by $\Delta R(l_1, l_2) > 0.2$, where $\Delta R(l_1, l_2) \equiv \sqrt{(\phi_{l_1} - \phi_{l_2})^2 + (\eta_{l_1} - \eta_{l_2})^2}$. Figure 4.2 shows the distributions of Z invariant mass and transverse momentum in the electron channel.

4.2.5 Jet Selection

As mentioned in Section 2.5.2, hadronic jets in this analysis were reconstructed using the anti-$k_\perp$ cluster algorithm with radius parameter R = 0.4. The algorithm takes as inputs topological clusters of energy deposited in the detector calorimeters. Jets were required to have $P_T^{jet} > 30$ GeV and rapidity $|y^{jet}|<$

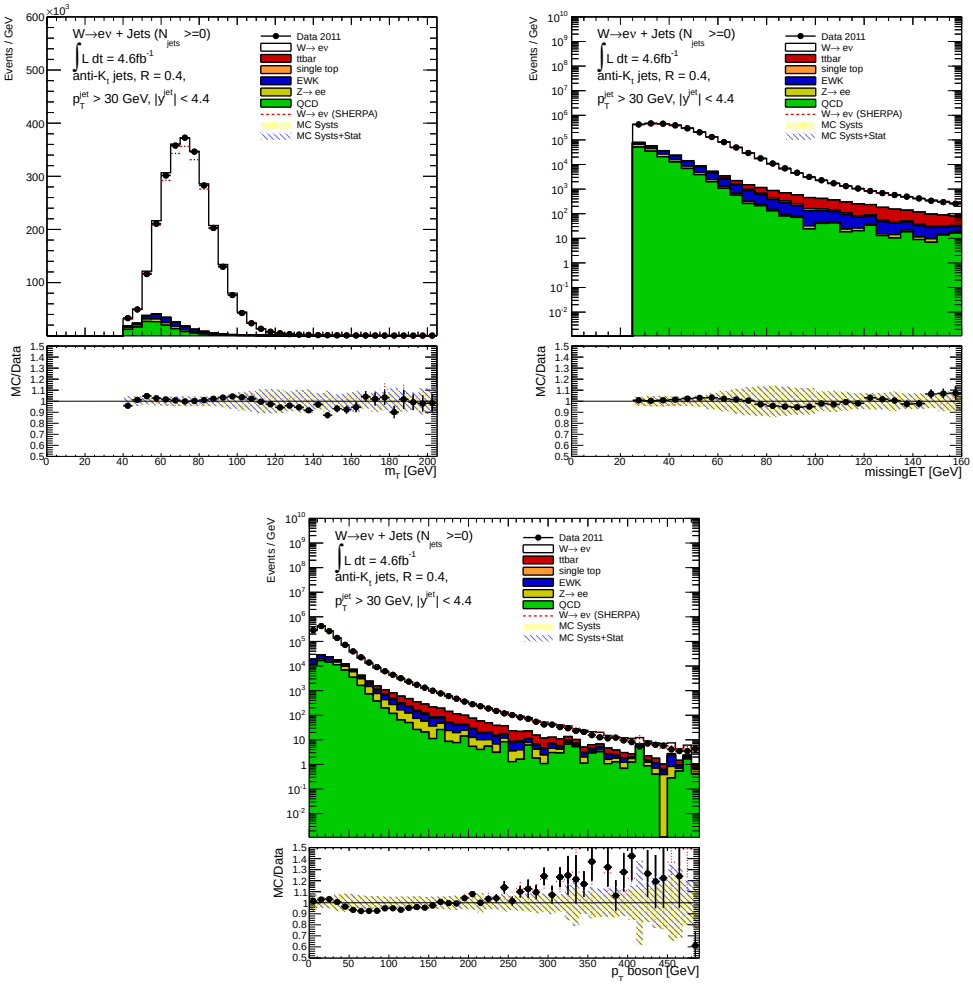

Figure 4.1: Transverse mass (M_T), E_T^{miss} and W boson P_T distributions in the $W \to e\nu$ channel. The error band consists of all detector level systematics discussed in Section 4.4 and those associated with the data-driven QCD and $t\bar{t}$ background estimations discussed in Sections 5.1.3 and 5.2.4 respectively.

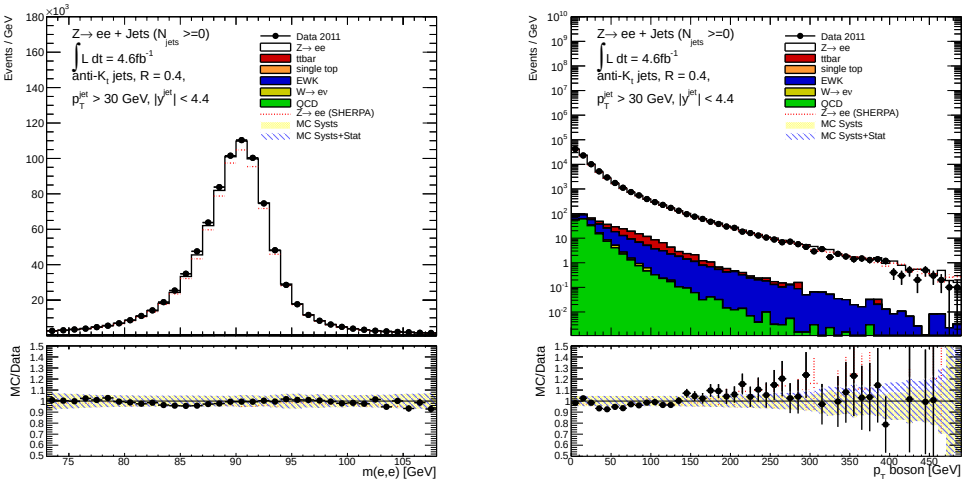

Figure 4.2: Z boson invariant mass and P_T distributions in the $Z \rightarrow ee$ channel. The error band consists of all detector level systematics discussed in Section 4.4 and those associated with the data-driven QCD background estimation discussed in Section 5.1.3.

4.4. To avoid the misidentification of leptons as jets, a jet-lepton isolation requirement was imposed that removed any jet within $\Delta R < 0.5$ of the leading lepton in the W channel, and the first and second leading leptons in the Z channel.

To remove jets from pile-up events (extra proton-proton interactions in the same bunch crossing as the hard scatter process), a cut was placed on the jet vertex fraction (JVF). JVF is a measure of the fraction of the P_T sum of tracks associated with a jet that come from the hard scatter process (i.e. originating from the primary vertex), divided by the P_T sum of all tracks associated with the jet (as illustrated in Figure 4.3). Only jets that satisfied JVF > 0.75 (i.e. at least 75% of the track P_T associated with the jet originated from the primary vertex) passed the selection. This cut was applied to all jets within $|\eta| < 2.4$, to be within the acceptance of the tracker.

Preselection
≥ 1 primary vertex, $N_{tracks} \geq 3$
LAr noise burst veto
Electron Selection
Cluster-based reconstruction algorithm
tight++ electron ID
Passes e20_medium (periods D-I), e22_medium (K), e22vh_medium1 (L-M) triggers
$P_T > 25$GeV
$\|\eta\| < 2.47$ (excluding $1.37 < \|\eta\| < 1.52$ barrel-endcap transition region)
Electron isolation
Muon Selection
STACO combined muon
Passes EF_mu18_MG or EF_mu18 (periods D-I),
EF_mu18_MG_medium or EF_mu18_medium (J-M)
$P_T > 25$GeV
$\|\eta\| < 2.4$
Muon isolation: $\Sigma P_T^{cone20}/P_T^{\mu} < 0.1$
$\|d_0/\sigma(d_0)\| < 3.0$

Table 4.3: Event preselection and lepton selections, common to both $W \to l\nu$ and $Z \to ll$ channels.

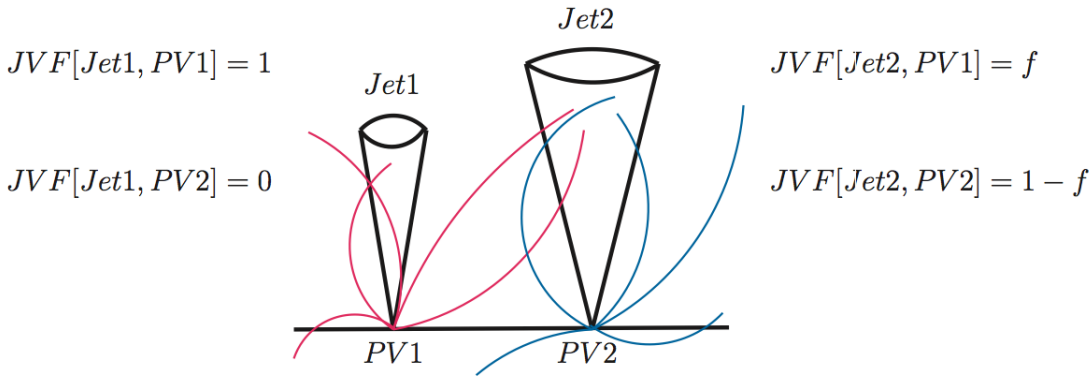

Figure 4.3: Illustration of the jet vertex fraction, here f refers to the fraction of P_T within Jet 2 that belongs to tracks originating from vertex PV1.

W$\rightarrow l\nu$ Selection
Exactly one lepton
$E_T^{miss} > 25$GeV
$M_T > 40$GeV
Z$\rightarrow ll$ Selection
Exactly 2 oppositely charged leptons
$66 \leq M_{ll} \leq 116$GeV
Lepton separation: $\Delta R(l_1, l_2) > 0.2$
Jet Selection
$P_T^{jet} > 30$GeV
$\lvert y^{jet}\rvert < 4.4$
Jet isolation: $\Delta R(l, jet) > 0.5$
Pile-up removal: $\lvert JVF\rvert > 0.75$, if $\eta < 2.4$

Table 4.4: Vector boson and jet selections, common to both electron and muon channels.

	N_{jet}=0	N_{jet}=1	N_{jet}=2	N_{jet}=3	N_{jet}=4
			$W \to e\nu$ + jets		
W$\to e\nu$	10 400 000 ± 639 000	1180 000 ± 85 800	260 000 ± 19 900	52 100 ± 4600	10 300 ± 1030
Z$\to ee$	32 400 ± 3490	114 000 ± 11 400	23 300 ± 2500	6110 ± 720	1510 ± 201
$t\bar{t}$	444 ± 52	3850 ± 360	12 000 ± 974	15 700 ± 1190	12 800 ± 498
multi-jet	448 000 ± 72 200	169 000 ± 16 700	41 000 ± 3760	9810 ± 871	1950 ± 269
electroweak	201 000 ± 11 900	39 300 ± 2120	11 600 ± 696	2690 ± 199	525 ± 45
single top	604 ± 47	2850 ± 140	4350 ± 170	1850 ± 95	618 ± 41
Total Predicted	11 100 000 ± 643 000	1 510 000 ± 98 800	352 000 ± 23 500	88 300 ± 5620	27 700 ± 1370
Total Observed	10 878 398	1 548 000	361 957	91 212	28 076

			$Z \to ee$ + jets		
Z$\to ee$	752 129 ± 46 613	95 492 ± 6848	21 236 ± 1651	4389 ± 379	909 ± 89
W$\to e\nu$	60 ± 10	17.8 ± 4.5	1.7 ± 1.1	1.1 ± 0.9	0.2 ± 0.2
$t\bar{t}$	27.4 ± 5.2	213 ± 28	424 ± 52	215 ± 28	79 ± 11
multi-jet	1468 ± 301	198 ± 102	97 ± 50	22 ± 11	5.5 ± 2.9
electroweak	778 ± 34	503 ± 26	278 ± 18	65.7 ± 5.6	11.8 ± 1.3
single top	2.3 ± 0.3	3.1 ± 0.4	1.5 ± 0.3	0.6 ± 0.2	0.2 ± 0.1
Total Predicted	754 465 ± 46 587	96 427 ± 6883	22 038 ± 1665	4693 ± 390	1006 ± 93
Total Observed	761 280	99 991	22 471	4729	1050

Table 4.5: Event yield table to show the number of events predicted by Monte Carlo simulation and data-driven methods (multi-jet events and $t\bar{t}$ events for 3 and 4 jets), compared with the total number of events observed in data. Top: W$\to e\nu$ + jets event selection; Bottom: Z$\to ee$ + jets event selection.

	N_{jet}=0	N_{jet}=1	N_{jet}=2	N_{jet}=3	N_{jet}=4
$W \to \mu\nu$ + jets					
W$\to \mu\nu$	12 400 000 ± 768 000	1 400 000 ± 102 000	300 000 ± 23 200	59 800 ± 5230	11 900 ± 1200
Z$\to \mu\mu$	450 000 ± 27 900	60 100 ± 4640	13 400 ± 1150	2860 ± 288	599 ± 69
$t\bar{t}$	375 ± 42	3380 ± 329	12 000 ± 990	18 700 ± 1240	13 900 ± 488
multi-jet	203 000 ± 6800	193 000 ± 3120	39 300 ± 723	9160 ± 302	2030 ± 122
electroweak	259 000 ± 15 200	45 400 ± 2520	12 900 ± 769	2850 ± 208	574 ± 57
single top	700 ± 53	3150 ± 157	4680 ± 186	1970 ± 100	646 ± 44
Total Predicted	13 300 000 ± 770 000	1 700 000 ± 104 000	383 000 ± 23 800	95 400 ± 5680	29 600 ± 1340
Total Observed	13 414 400	1 758 239	403 146	99 749	30 400
$Z \to \mu\mu$ + jets					
Z$\to \mu\mu$	1 300 000 ± 79 300	166 000 ± 11 800	36 100 ± 2777	7372 ± 640	1472 ± 145
W$\to \mu\nu$	251 ± 23	128 ± 12	44.3 ± 5.5	14.9 ± 2.4	3.1 ± 0.8
$t\bar{t}$	59.1 ± 8.80	448 ± 52	820 ± 86	491 ± 50	220 ± 24
multi-jet	4360 ± 955	820 ± 192	326 ± 97	91 ± 28	29.7 ± 9.7
electroweak	1420 ± 60	890 ± 43	480 ± 30	110.4 ± 8.7	19.8 ± 2.0
single top	15.3 ± 1.20	48.9 ± 2.50	24.1 ± 1.5	9.2 ± 0.9	2.4 ± 0.4
Total Predicted	1 300 000 ± 79 300	168 000 ± 11 800	37 794 ± 2820	8089 ± 662	1747 ± 157
Total Observed	1 302 010	171 200	38 618	8397	1864

Table 4.6: Event yield table to show the number of events predicted by Monte Carlo simulation and data-driven methods (multi-jet events and $t\bar{t}$ events for 3 and 4 jets), compared with the total number of events observed in data. Top: W$\to \mu\nu$ + jets event selection; Bottom: Z$\to \mu\mu$ + jets event selection.

4.3 Jet Calibration

As we shall see in subsequent sections, the way in which jets are calibrated by the ATLAS collaboration contributes the largest source of systematic uncertainty on the final measurements of this analysis. This section outlines the jet calibration techniques employed for the ATLAS detector.

The ATLAS calorimeters are calibrated using test beam measurements with electrons in order to correctly measure energy from electromagnetic showers. They are thus calibrated to the electromagnetic (EM) scale[3] to achieve the best response to electromagnetic showers [62]. When reconstructing jets, ATLAS suffers from non-compensation, i.e. there is energy deposited in the calorimeters from hadron showers that goes undetected (e.g. energy lost in nuclear breakdowns or excitations). Therefore, there is a lower response to hadrons. A jet-energy scale (JES) correction is thus applied to correct for this effect. Correcting the JES to the EM scale is known as EM+JES calibration. Furthermore, EM+JES also corrects for energy lost in regions of the detector with poor instrumentation, and lost via calorimeter and jet reconstruction inefficiencies [63, 64]. Before the JES is calculated and applied, jets origin corrections are applied, as are corrections to account for pile-up effects.

4.3.1 Jet Origin and Pile-up Corrections

Jets reconstructed from calorimeter clusters are initially assumed to have originated in the geometrical centre of the detector. It is therefore necessary to correct the jet inputs to point to the primary vertex (as defined in Section 4.2) and recalculate the jet 4-momentum. This correction improves the angular resolution and also slightly improves the jet P_T resolution.

Energy associated with additional interactions not originating from the hard scatter ("pile-up" events) must also be corrected for. An average energy correction is therefore subtracted from EM scale jets. The correction is derived

[3]The Z resonance is used to set the absolute energy scale [62].

from minimum bias data and is calculated as a function of the number of vertices in an event and jet η.

4.3.2 Jet Energy Scale

Following the former two jet corrections, EM+JES calibration is applied. The JES correction is derived using Monte Carlo simulated events (a PYTHIA6 di-jet sample using the AMBT1 tune[65]). It is calculated by first matching individual particle-level jets (defined using final-state particles) to individual jets that have been reconstructed in the calorimetry (defined using the full detector information). The final correction for the calorimeter energy response is obtained by dividing the energy of the particle-level jet by the EM scale energy of the calorimeter jet to which it has been matched.

The calibration concludes with a small η-dependent correction to remove any direction bias, resulting from jets reconstructed in regions of the detector with a lower energy response due to dead material. Without this correction, the 4-momentum sum of the clusters contributing to the reconstruction of a jet will be biased towards regions of the detector with higher response. This correction is a function of energy and η. It is typically $\sim$1% in most detector regions, but it can be as large as 7% in the crack regions between the barrel and the forward calorimetry [63, 64].

4.4 Detector Level Systematic Uncertainties

This section presents a breakdown of the sources of systematic uncertainty on the measurements of W+jets and Z+jets events at detector level. Uncertainties pertaining to the evaluation of jet-energy scale and the resolution of jet energy, and of missing transverse energy in the detector are common to both electron and muon channels.

Each of the systematic uncertainties described below (with the exception of

the Monte Carlo background uncertainties) was evaluated by a dedicated ATLAS subgroup. They provided the size of the relevant uncertainty and a general prescription on how to apply it to an analysis. The ATLAS **Jet/EtMiss Performance** group provided the jet-energy scale, jet-energy resolution and E_T^{miss} systematics, the **Egamma Performance** and **Muon Combined Performance** groups provided the electron and muon systematics respectively.

For each source of systematic uncertainty, the effect on the detector-level results was evaluated by varying the Monte Carlo correction factors (e.g. the jet-energy scale corrections discussed in the following section) for signal and background processes up and down by one sigma, and applying the event selection described above. The up and down variations were applied and evaluated separately for each uncertainty. This propagates the uncertainty through the analysis, the results of which can be compared with the nominal results to derive the relative effect of each uncertainty. Where a background was estimated using a data-driven technique (see Chapter 5), the effect of each uncertainty on the estimation was evaluated by performing the fit for each systematic variation of the Monte Carlo templates. Figure 4.4 shows the relative size of the electron and muon channel systematic uncertainties described in this section, for the exclusive jet multiplicity distributions. Tables 4.7 and 4.8 relate the systematic uncertainties for both the electron and muon channels in exclusive jet multiplicity bins.

4.4.1 Jet Energy Scale Uncertainty

Uncertainties related to the jet calibration, e.g. jet-energy scale corrections, contribute the largest source of systematic uncertainty at detector level in the separate lepton channels. These uncertainties are common to both W + jets and Z + jets channels, and therefore largely cancel in the ratio. Jet-energy scale uncertainties considered in this analysis can be sub-categorised into four main sources:

- Uncertainties associated with the methods of calibration.
- Uncertainties on the pile-up correction.
- Uncertainties due to the presence of jets close to the calibrated jet.
- Uncertainties arising from differences in jet flavour composition and response between the MC samples used for calibration and those used in the analysis.

Uncertainties due to methods used for jet calibration are evaluated in three ways [66]:

4.4.1.1 η-Intercalibration

Jets in the central region of the detector are reconstructed with a higher precision than forward jets due to the higher tracking precision in the inner detector. Therefore, the systematic uncertainty from JES is lower for jets in the central region. To ensure uniform response throughout the detector, the jets in the forward region are calibrated against the well-measured jets in the central region. This was achieved by balancing the P_T of a di-jet system with one central and one forward jet, this is known as η-intercalibration. The uncertainty associated with this jet calibration was evaluated as the RMS spread of the Monte Carlo predictions used for the study around the data points. This is because Monte Carlo predictions for the jet response significantly differ and for this quantity there is no reason for trusting one over the other.

4.4.1.2 Single-hadron response at large P_T

The uncertainty in EM+JES calibration arising from the calorimeter response to isolated hadrons is evaluated by taking the ratio of the energy deposited in the calorimeter, by the isolated hadron, to its momentum. This is calculated from the associated track in the inner detector. The deviation of Monte Carlo predictions from data for the value of <E/p> is taken as a jet-energy scale uncertainty.

4.4.1.3 Non-closure

Once JES corrections have been calculated, they can be re-applied to the nominal sample of reconstructed-level Monte Carlo jets from which they were derived and compared to Monte Carlo jets reconstructed at particle level. If the corrections are calculated perfectly the ratio of P_T distributions for the corrected jets and particle-level jets should yield unity. The largest deviation from unity in the jet P_T and energy is taken as a systematic uncertainty.

4.4.2 Jet-energy Resolution

Jet-energy resolution (JER) relates to the width of the jet response in the detector, and is calculated with fully calibrated jets. This is achieved via two techniques involving di-jet systems with a back-to-back topology ($\Delta\phi > 2.8$), in which both jets are in the same region of the detector and therefore subject to the same detector response. The first involves measuring the P_T asymmetry $((P_{T_{jet1}} - P_{T_{jet2}})/(P_{T_{jet1}} + P_{T_{jet2}}))$. The second method used to determine the jet-energy resolution is a bisector technique. It involves constructing a balance P_T vector which is the vector sum of the di-jet system in question and projecting onto the di-jet η and ϕ axes [67].

As for JES uncertainties, JER uncertainties are evaluated by comparing the results of the above measurements from data and Monte Carlo.

4.4.3 Missing Transverse Energy

The missing transverse energy, E_T^{miss}, in an event is calculated by combining measurements of all the physics objects (electrons, muons and jets) in an event, with the addition of soft terms which account for energy depositions in the calorimeter not directly included in the aforementioned physics objects [68]. Uncertainties in the missing transverse energy are derived from uncertainties in the resolution and scale of the soft terms that contribute to the E_T^{miss} calculation. Any change to the physics objects are also propagated into

the E_T^{miss} calculation. A prescription is provided to shift the E_T^{miss} up and down by its resolution. Separate up and down variations are applied to the soft terms and the physics objects. This is because the systematic uncertainty on these terms is treated as uncorrelated. Uncertainties on E_T^{miss} only affect the W+jets channel, since no E_T^{miss} requirement is included in the Z+jets event selection.

4.4.4 Lepton Systematic Uncertainties

Lepton energy uncertainties are derived using data-Monte Carlo comparisons from tag and probe studies. Tag and probe is a common method for measuring lepton efficiencies, whereby $Z \to ll$ events are selected to provide a clean sample of leptons. One lepton, the tag, must pass strict identification cuts while the other, the probe, has few or no selection requirements. The invariant mass of the two leptons must also be near the Z mass peak. By this method the probe lepton is considered unbiased and can therefore be used for energy calibration and efficiency studies

4.4.4.1 Electron Uncertainties

Both the electron-energy scale and resolution are measured using data and Monte Carlo; the two are compared and the latter is then scaled to the data. Systematic uncertainties on the tag and probe method used to derive the scale factors are evaluated using Monte Carlo and can be generally separated into five terms [59]:

- A statistical component from the limited statistics of the samples used to conduct the study.
- A method component (i.e. non-closure).
- Uncertainty from the choice of generator used to conduct the study.
- A material budget component derived by varying the ATLAS geometry used to conduct the study and comparing with results using the standard

ATLAS geometry.

- A pre-sampler component.

Electron reconstruction, identification and trigger scale factors are also derived using a tag and probe technique, with data and Monte Carlo predictions [59]. The reconstruction and identification scale factors each have 7 associated systematic components. These are subcategorised into six correlated components and one uncorrelated. The uncorrelated components are the dominant source of uncertainty on the electron scale factors. The electron uncertainties are somewhat cancelled in the ratio of W+jets to Z+jets events. However, a full cancellation is not achieved due to different numbers of electrons in the final state of W+jets and Z+jets events. In any case, each individual uncertainty in each channel is fully propagated through the analysis before forming the final ratios.

4.4.4.2 Muon Uncertainties

As with the electron channel, muon uncertainties are derived using a tag and probe technique, in this case with $Z \rightarrow \mu\mu$ events [61]. Scale factors are applied for muon P_T resolution of the inner detector and muon spectrometer, P_T scale, reconstruction and trigger efficiencies. Systematic uncertainties are associated with each of the aforementioned muon scale factors and are evaluated using similar methods to those described for the electron channel. All muon systematics are small compared to others in the analysis.

4.4.5 Uncertainties on Monte Carlo Backgrounds

As mentioned in Section 4.1, each Monte Carlo sample used was normalised to the relevant (N)NLO cross-section[4]. Each background processes modelled by

[4]The NNLO cross-section calculation for hadronic Z production was calculated using the FEWZ 2.0 program [69] and the NNLO calculation for top pair production was provided by the top++ 2.0 program [70].

Monte Carlo will therefore have an uncertainty associated with the uncertainty on that normalisation. The cross-section uncertainty for electroweak processes is ∼5% (arising from scale and PDF uncertainties in the NNLO prediction). For WW and ZZ diboson backgrounds the uncertainty is also 5%, and 7% for WZ (taken from [71]). For single top backgrounds the t-channel has a 3.4% associated uncertainty and 4% for the s-channel.

The $t\bar{t}$ background for the Z+jets channel was also estimated using Monte Carlo simulation provided by ALPGEN+HERWIG+JIMMY. The uncertainty on this background includes a normalisation uncertainty of 6% (taken from [72]). Another uncertainty is included which accounts for shape differences in the predictions. The uncertainty on the final result was evaluated for each distribution by performing the unfolding (as described in Chapter 6) using an alternative $t\bar{t}$ sample provided by POWHEG+PYTHIA and taking the difference between that result and the result achieved using the nominal ALPGEN+HERWIG+JIMMY $t\bar{t}$ sample.

4.5 Detector Level Distributions

Figures 4.5, 4.6 and 4.7 show the exclusive jet multiplicity, leading jet P_T and leading jet rapidity distributions respectively, in the electron and muon channels, for both $W \rightarrow l\nu$ + jets and $Z \rightarrow ll$ + jets events. Included are the data-driven background estimations discussed in Chapter 5. The systematic uncertainty band includes all detector level systematics discussed in Section 4.4, and the systematics associated with the background estimations as discussed in Sections 5.1.3 and 5.2.4. In each plot the "MC/Data" ratio underneath the main plot is the ratio of selected data to ALPGEN signal plus background predictions from Monte Carlo and data-driven techniques. The red dotted line in the ratio represents a corresponding ratio in which SHERPA signal has replaced ALPGEN+HERWIG.

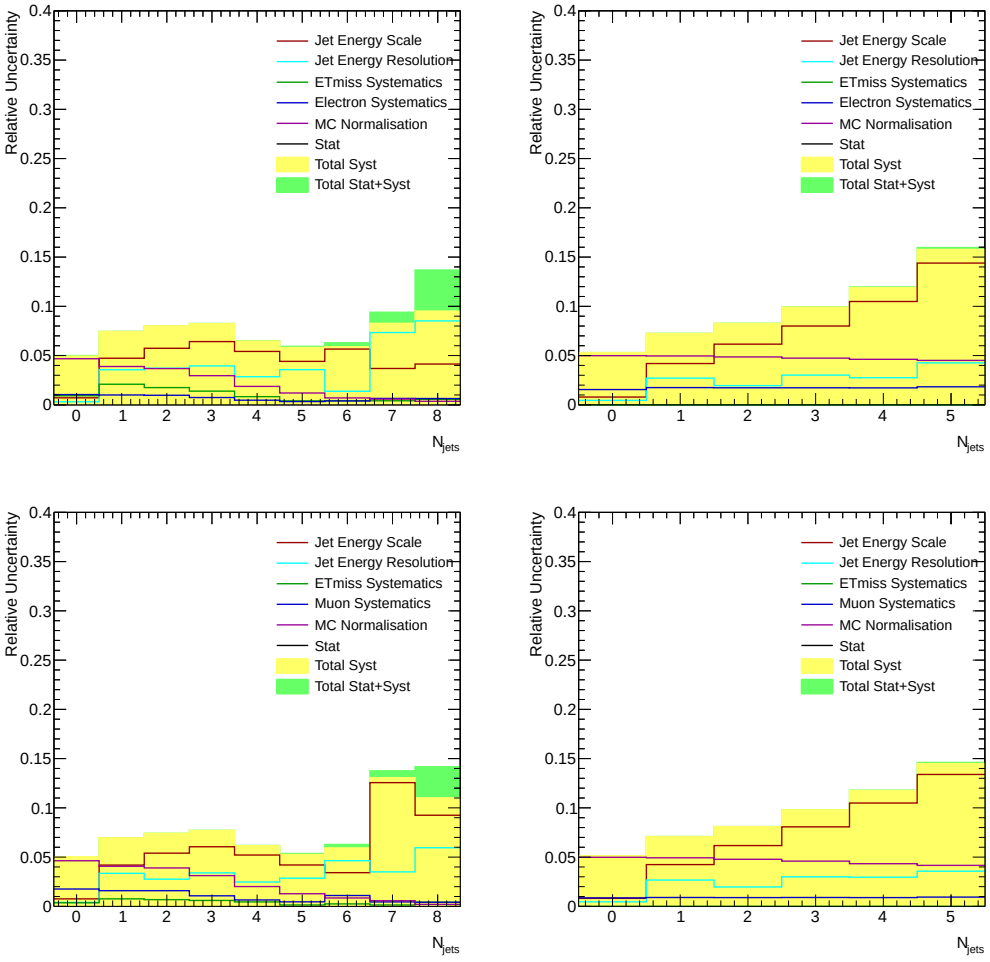

Figure 4.4: Electron and muon channel detector level systematic uncertainties for exclusive jet multiplicity. Top: Electron channel; Bottom: Muon channel; Left: W+jets channel; Right: Z+jets channel.

Systematic	N_{jet}=0	N_{jet}=1	N_{jet}=2	N_{jet}=3	N_{jet}=4	N_{jet}=5	N_{jet}=6	N_{jet}=7	N_{jet}=8
$W \to e\nu$ + jets									
JES	0.71	4.73	5.74	6.42	5.42	4.41	5.66	3.69	4.14
JER	0.31	3.56	3.72	3.95	2.85	3.57	1.38	7.34	8.52
E_T^{miss}	0.92	2.09	1.75	1.39	0.83	0.4	0.42	0.41	0.56
Electron	1.04	1.0	0.97	0.74	0.47	0.33	0.39	0.65	0.64
MC	4.68	3.89	3.68	2.96	1.87	1.2	0.7	0.58	0.36
Total Syst	4.94	7.45	8.02	8.24	6.47	5.82	5.89	8.27	9.51
Stat	0.78	0.13	0.18	0.36	0.65	1.15	2.22	4.46	9.83
Syst+Stat	5.00	7.45	8.02	8.25	6.50	5.93	6.23	9.40	13.68
$Z \to ee$ + jets									
JES	0.79	4.19	6.16	8.0	10.49	14.39	14.06	14.68	25.17
JER	0.45	2.71	1.95	3.02	2.75	4.26	4.62	20.78	19.71
E_T^{miss}	0.0	0.0	0.0	0.0	0.0	0.0	0.0	0.0	0.0
Electron	1.55	1.75	1.73	1.73	1.72	1.73	1.8	1.64	1.88
MC	4.99	4.96	4.86	4.74	4.62	4.51	4.42	4.4	4.48
Total Syst	5.30	7.25	8.26	9.92	11.91	15.77	15.55	25.87	32.33
Stat	0.09	0.24	0.29	0.58	1.21	2.45	5.63	12.98	27.95
Syst+Stat	5.30	7.25	8.27	9.94	11.97	15.96	16.53	28.94	42.74

Table 4.7: Detector level systematic uncertainties in the electron channel, values quoted as total percentage error.

Systematic	N_{jet}=0	N_{jet}=1	N_{jet}=2	N_{jet}=3	N_{jet}=4	N_{jet}=5	N_{jet}=6	N_{jet}=7	N_{jet}=8
					$W \to \mu\nu$				
JES	0.76	4.19	5.4	6.05	5.21	4.2	3.42	12.56	9.25
JER	0.4	3.35	2.76	3.4	2.47	2.86	4.64	3.5	5.95
E_T^{miss}	0.36	0.76	0.68	0.6	0.45	0.14	0.25	0.14	0.41
Muon	1.76	1.59	1.59	1.07	0.65	0.46	1.1	0.45	0.42
MC	4.63	4.07	3.9	3.12	2.01	1.28	0.85	0.57	0.29
Total Syst	5.04	6.96	7.41	7.71	6.15	5.26	5.93	13.05	11.01
Stat	0.06	0.09	0.14	0.31	0.57	1.05	2.06	4.34	8.92
Syst+Stat	5.04	6.96	7.41	7.71	6.18	5.36	6.28	13.76	14.17
					$Z \to \mu\mu$				
JES	0.81	4.24	6.17	8.07	10.49	13.39	15.24	20.86	15.36
JER	0.46	2.67	1.97	3.0	2.96	3.57	5.75	5.76	15.97
E_T^{miss}	0.0	0.0	0.0	0.0	0.0	0.0	0.0	0.0	0.0
Muon	0.86	0.9	0.89	0.9	0.89	0.94	0.94	0.89	0.88
MC	4.98	4.93	4.77	4.59	4.33	4.16	3.88	4.02	4.54
Total Syst	5.13	7.08	8.09	9.79	11.76	14.50	16.77	22.02	22.63
Stat	0.06	0.16	0.21	0.42	0.88	1.84	4.24	11.22	21.67
Syst+Stat	5.14	7.08	8.10	9.80	11.79	14.61	17.29	24.72	31.33

Table 4.8: Detector level systematic uncertainties in the muon channel, values quoted as total percentage error.

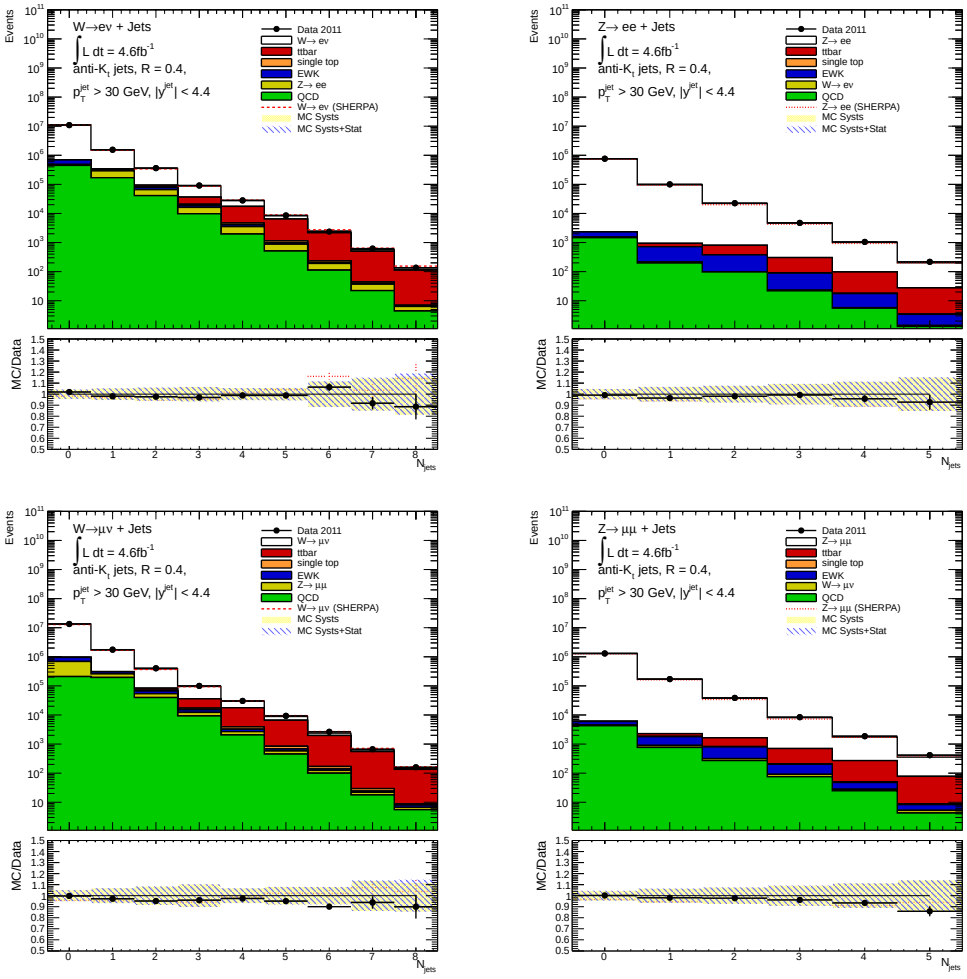

Figure 4.5: Detector level kinematic distributions (including data-driven backgrounds) for exclusive jet multiplicity. Left: W+jets channel; Right: Z+jets channel; Top: Electron channel; Bottom: Muon channel.

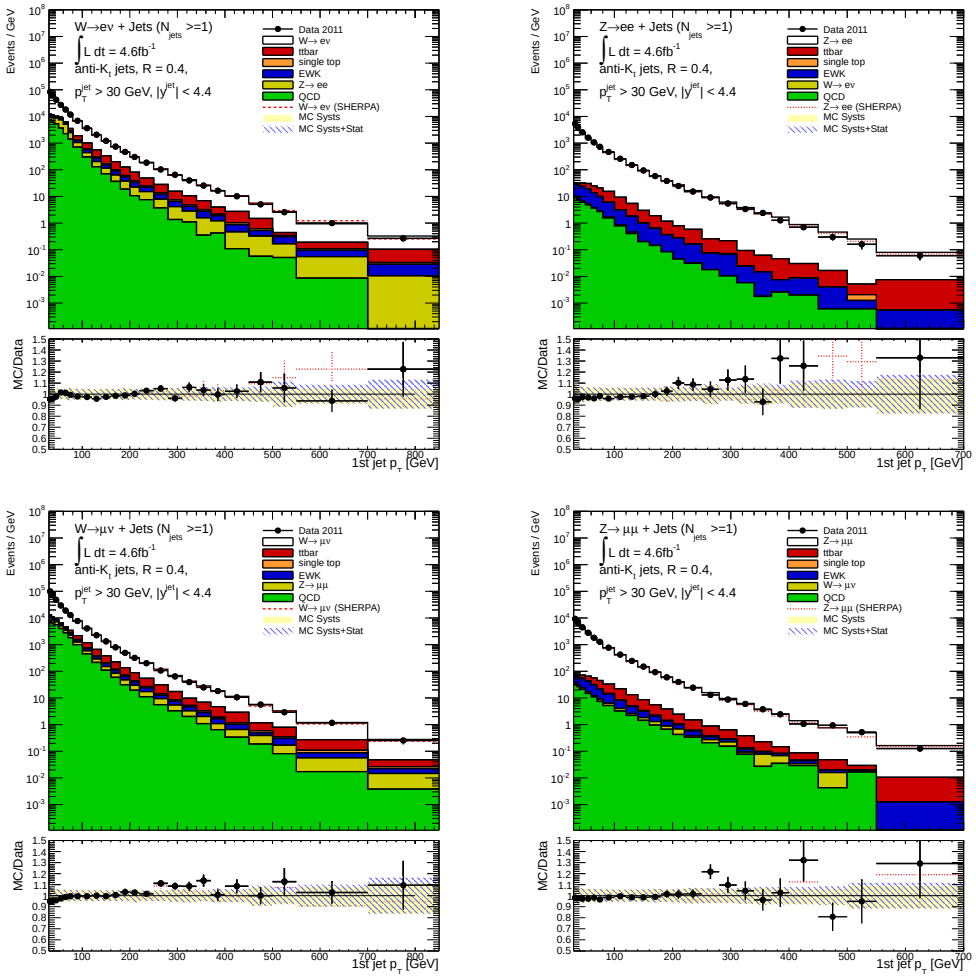

Figure 4.6: Detector level kinematic distributions (including data-driven backgrounds) for leading jet P_T. Left: W+jets channel; Right: Z+jets channel; Top: Electron channel; Bottom: Muon channel.

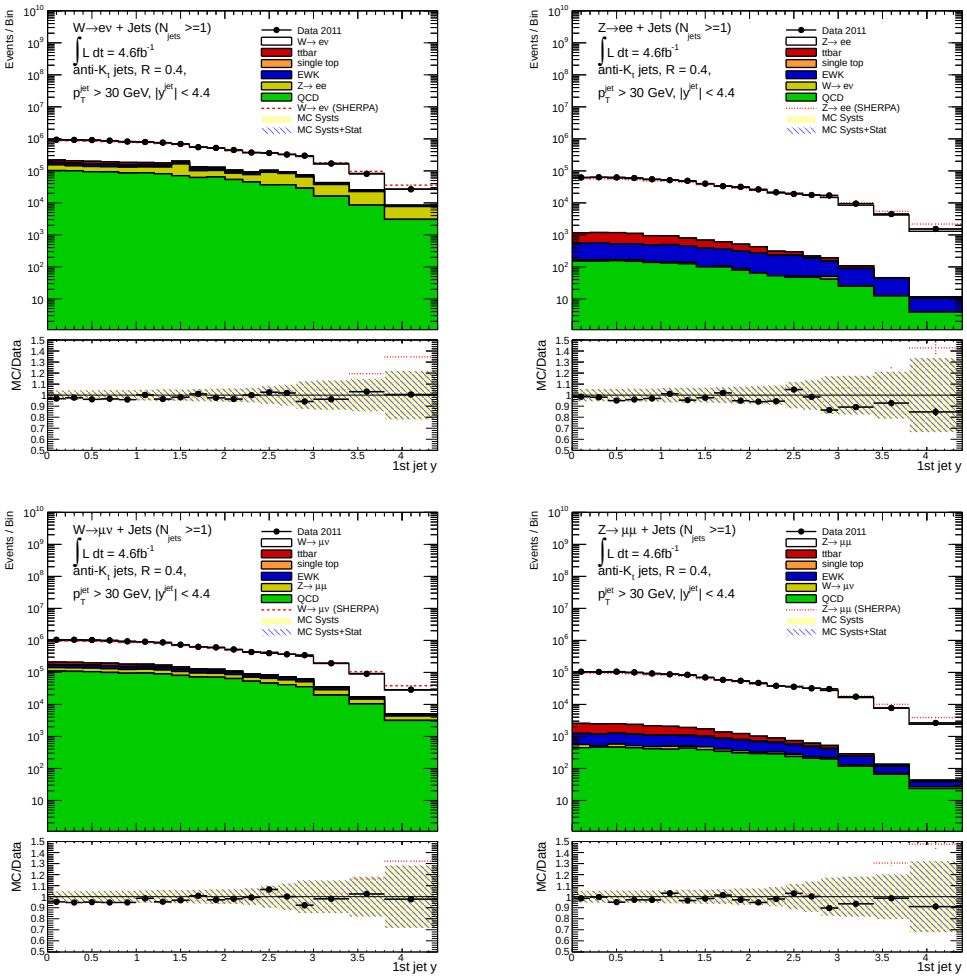

Figure 4.7: Detector level kinematic distributions (including data-driven backgrounds) for leading jet rapidity. Left: W+jets channel; Right: Z+jets channel; Top: Electron channel; Bottom: Muon channel.

Chapter 5

Background Characterisation

This chapter details the data-driven techniques developed for this analysis to estimate the size and shape of certain physics processes that are backgrounds to the signal events. They are QCD events for the $W \to l\nu$ + jets and $Z \to ll$ + jets channels, and $t\bar{t}$ events for the $W \to l\nu$ + jets channel[1].

5.1 Data-Driven QCD Background

Multi-jet events from QCD processes can have final state signatures indistinguishable from the signal processes of this analysis, and will contaminate the signal event selection. It was important to understand the rate at which such processes occur. In order to subtract this contribution from the signal selection we needed to estimate the size and shape of the QCD background contribution for each variable measured in this analysis. We achieved a QCD background characterisation via a data-driven technique. Such an approach

[1]The author's contribution to this part of the analysis was to adapt existing code in order to provide the muon channel QCD estimate for each variable in the analysis, for both $W \to \mu\nu$ + jets and $Z \to \mu\mu$ + jets channels. The author also provided the evaluation of the systematic uncertainties on the QCD estimation method in the muon channel (discussed in detail in Section 5.1.3), and the full propagation of the detector-level systematic uncertainties (described in Section 4.4) through the muon channel QCD estimation.

was taken due to the large uncertainties which accompany Monte Carlo simulations of hadronic backgrounds. For each lepton and boson channel, the basic technique was the same, and can be broken down into 4 stages; (i) selection of QCD control sample, (ii) extraction of control template shape, (iii) a fit to find normalisation scale factors and (iv) estimation of the background size and shape for each kinematic variable.

Selection of control sample: The first stage was to select a set of data which was enriched in QCD events while maintaining similar kinematic properties as the signal selection. This set of data was termed the "control" sample. Contamination of the QCD control sample from signal events, and events from electroweak and top background processes was evaluated by applying the control sample selection to Monte Carlo simulation modelling the relevant processes[2]. This sample will be referred to as $(\text{Sig+Bkg})^{\text{CS}}$.

Shape of Control Template: A variable was then chosen with the power to discriminate between the shape of QCD events and the Sig+Bkg events selected with the signal selection, referred to here as $(\text{Sig+Bkg})^{\text{SS}}$ (where "SS" refers to the signal selection). The QCD control template was found by subtracting $(\text{Sig+Bkg})^{\text{CS}}$ from the control sample for the distribution of the chosen variable. The subtraction was a bin-by-bin subtraction of histograms.

Extraction of normalisation scale factors: The control template and the $(\text{Sig+Bkg})^{\text{SS}}$ template were fit to the data distribution from the signal selection, data^{SS}. The fit determined the relative contribution of QCD events and $(\text{Sig+Bkg})^{\text{SS}}$ events in data^{SS}. This provided normalisation scale factors for the rate of QCD events with respect to the total number of signal data events.

[2] A study to determine the effect of using a data driven $t\bar{t}$ estimate (as described in Section 5.3) in place of Monte Carlo for this template concluded that it had a negligible impact on the QCD fractions obtained by the fit, thus Monte Carlo was used.

Estimation of the QCD background for each variable: Finally, the size and shape of the QCD contribution was extracted for each kinematic variable studied in this analysis. This was achieved by applying the control sample selection to data and subtracting $(\text{Sig+Bkg})^{\text{CS}}$ to find the shape of the QCD background. The background shape for each distribution was then scaled by the normalisation scale factors determined from the fit.

The details of the control sample selection and the fit, and their associated systematic uncertainties, are discussed in the following subsections for both lepton and both boson channels.

5.1.1 Muon Channel

QCD events that contaminate the $W \to \mu\nu$ + jets and $Z \to \mu\mu$ + jets signals are primarily heavy flavour events decaying to real muons. This is because the muon isolation requirements in the event selection (Section 4.2.2) were designed to reject other types of multi-jet events. As mentioned above, the Monte Carlo simulations of hadronic backgrounds are accompanied by large uncertainties arising from the difficulty in modelling the rate at which isolated muons are falsely reconstructed from a jet or a muon within a jet, and from uncertainties on the cross-section of such hadronic processes. For this reason, a data driven technique was employed in this analysis to model the contribution of QCD background processes. The variables used to discriminate between signal and background were E_T^{miss} and invariant mass ($M_{\mu\mu}$) in the $W \to \mu\nu$ + jets and $Z \to \mu\mu$ + jets channels respectively. As mentioned above, a QCD-enriched control sample was selected from data. A control template was then extracted and was fit to the E_T^{miss} distribution in the $W \to \mu\nu$ + jets channel and to the $M_{\mu\mu}$ distribution in the $Z \to \mu\mu$ + jets channel.

5.1.1.1 Selection of Control Sample

It was required of the QCD control samples that they be enriched in QCD events, while maintaining similar kinematic properties to the QCD events which contaminate the data signal sample. With this in mind, the $W \rightarrow \mu\nu$ + jets channel QCD enriched data sample was selected by requiring all events to pass the full $W \rightarrow \mu\nu$ + jets event selection, as described in Section 4.2.

The main change to the W signal event selection to obtain a QCD-enriched control sample was to reverse the isolation requirement on the leading muon[3], but restricting the isolation to a window. The requirement (termed "restricted anti-isolation") was that the P_T sum of all tracks within a $\phi - \eta$ cone of 0.2 around the leading muon, as a fraction of leading muon P_T, was between 10-50%, i.e. $0.1 < \Sigma P_T^{cone20}/P_T^{\mu} < 0.5$. The muon isolation requirement on the impact parameter (d_0) significance was still applied. The "restricted" requirement was applied to reduce contamination from Sig+Bkg processes.

A number of alternative selection criteria were investigated and evaluated in terms of the QCD fraction they yielded and the relative contamination from W+jets signal only, and Sig+Bkg processes. This is discussed in the following section.

In the $Z \rightarrow \mu\mu$ + jets channel, the control sample was selected by applying the full $Z \rightarrow \mu\mu$ + jets event selection with an anti-isolation muon selection. Due to lower statistics, the anti-isolation requirement was not "restricted" ($\Sigma P_T^{cone20}/P_T^{\mu} > 0.1$ was applied) and the d_0 significance isolation requirement was also removed.

The QCD control template for W(Z) was formed by performing a bin-by-bin histogram subtraction of the E_T^{miss} ($M_{\mu\mu}$) distribution for $(\text{Sig+Bkg})^{\text{CS}}$ from the control sample E_T^{miss} ($M_{\mu\mu}$) distribution.

In the $W \rightarrow \mu\nu$ + jets channel, one change was made for the purposes of

[3]As discussed in Section 4.2.2, the muon isolation requirement for the nominal signal selection was $< \Sigma P_T^{cone20}/P_T^{\mu} < 0.1$

the fit, to both the signal and control sample selections. The E_T^{miss} requirement was removed (while still requiring the transverse mass, $M_T > 40$GeV). QCD events do not contain high P_T neutrinos and thus peak at lower values of E_T^{miss}. Therefore, the removal of the E_T^{miss} requirement exploited the shape difference between the control and (Sig+Bkg)$^{\mathrm{SS}}$ templates at low E_T^{miss}. This was primarily for the purpose of performing the fit to find the relevant contribution of each, but also further enriched the control sample in QCD events.

5.1.1.2 Alternative Control Sample Selection

For the $W \to \mu\nu$ + jets channel, a number of different combinations of the isolation requirements were investigated as potential alternatives to the restricted anti-isolation with d_0 significance requirement (**RestrAntiIsoWithD0**) that was used in the analysis. The alternative QCD control sample requirements were as follows:

- **AntiD0WithIso**: Reversed d_0 significance (fails $d_0/\sigma_{d_0} < 3$), includes signal isolation cut.
- **AntiD0WithIso_D0Window**: Reversed d_0 significance, includes signal isolation cut and additional requirement of $0.1 < |d_0| < 0.4$.
- **AntiD0NoIso**: Reversed d_0 significance, no isolation requirement.
- **AntiIsoNoD0**: Reversed signal isolation requirement ($\Sigma P_T^{cone20}/P_T^{\mu} > 0.1$), no d_0 significance requirement.
- **AntiIsoWithD0**: Reversed signal isolation, includes $d_0/\sigma_{d_0} < 3$ cut.
- **RestrAntiIso**: Restricted reversed signal isolation within $0.1 < \Sigma P_T^{cone20}/P_T^{\mu} < 0.5$ window.
- **RestrAntiIsoWithD0**: Restricted reversed signal isolation within window, includes d_0 significance cut.

For each control sample selection, the QCD fractions (ratio of QCD events in data to the total number of data events) were extracted by fitting the control sample template and the (Sig+Bkg)$^{\mathrm{SS}}$ template to the data$^{\mathrm{SS}}$ distribution. The

signal only and Sig+Bkg contaminations were also determined for each control sample selection.

The control sample should provide a high QCD fraction while maintaining tolerable contamination. Table 5.1 shows the QCD fraction yielded by fits using the control sample selections listed above, along with signal only and Sig+Bkg contaminations. The AntiD0WithIso and AntiD0noIso selections were deemed unsuitable due to large signal contamination in the selected control sample. AntiD0WithIso_D0Window was rejected due to a large background contamination and was thus more dependent on the Monte Carlo modelling of diboson and $t\bar{t}$ processes. Of the remaining two selections, both of which employ the restricted anti-isolation requirement, RestrAntiIsoWithD0 was chosen as the nominal template following comparison studies with heavy flavour $b\bar{b}$ and $c\bar{c}$ Monte Carlo samples generated using Pythia. For this study, the shape of the $b\bar{b}$ and $c\bar{c}$ leading jet P_T distribution for each selection was compared with the shape of the distribution from the signal selection. The RestrAntiIsoWithD0 control sample was found to be most similar with the signal selection distribution.

5.1.1.3 Fit Results

The fit was performed (using the TFractionFitter class in ROOT [73]) by fitting the QCD control template and the (Sig+Bkg)^{SS} template to the data^{SS} distribution. In the $W \rightarrow \mu\nu$ + jets channel, the fit was performed on the E_T^{miss} distribution within the range [15, 70] GeV and in the $Z \rightarrow \mu\mu$ + jets channel on the invariant mass, $M_{\mu\mu}$, distribution within the range [45, 150] GeV. The normalisation of each template was varied to obtain the best fit with the data distribution, thus determining the fraction of QCD and Sig+Bkg events entering the data signal selection. This provided scale factors for the total normalisation of the shape of QCD events.

The fits in both channels were performed in bins of exclusive jet multiplicity, yielding a separate normalisation scale factor for each. In the $W \rightarrow \mu\nu$ + jets

Template	N_{jet}=0	N_{jet}=1	N_{jet}=2	N_{jet}=3	N_{jet}=4	N_{jet}=5
QCD Fraction (%)						
AntiD0WithIso	0.0414	0.1397	0.1314	0.1265	0.1066	0.0665
AntiD0WithIso_D0Window	0.0250	0.1274	0.1176	0.1129	0.0870	0.0488
AntiD0NoIso	0.0257	0.1281	0.1160	0.1121	0.0832	0.0506
AntiIsoNoD0	0.0211	0.1241	0.1122	0.1084	0.0807	0.0489
AntiIsoWithD0	0.0222	0.1228	0.1106	0.1066	0.0802	0.0484
RestrAntiIso	0.0211	0.1201	0.1088	0.1041	0.0776	0.0493
RestrAntiIsoWithD0	0.0223	0.1193	0.1082	0.1027	0.0754	0.0497
Signal Contamination (%)						
AntiD0WithIso	33.03	3.98	3.54	2.73	2.54	2.11
AntiD0WithIso_D0Window	11.9	1.16	1.06	0.73	0.54	0.44
AntiD0NoIso	14.21	0.62	0.4	0.28	0.24	0.18
AntiIsoNoD0	7.18	0.48	0.4	0.32	0.27	0.23
AntiIsoWithD0	10.39	0.8	0.72	0.61	0.54	0.47
RestrAntiIso	8.36	0.71	0.71	0.62	0.55	0.5
RestrAntiIsoWithD0	12.0	1.16	1.25	1.14	1.04	0.98
Sig+Bkg Contamination (%)						
AntiD0WithIso	44.15	7.2	7.87	9.4	13.71	19.64
AntiD0WithIso_D0Window	23.51	3.33	3.73	4.54	6.4	11.15
RestrAntiIso	9.39	0.88	1.11	1.82	3.38	5.85
RestrAntiIsoWithD0	13.41	1.41	1.79	2.68	4.78	8.13

Table 5.1: QCD fraction, signal contamination and total contamination for various QCD template candidates in the $W \to \mu\nu$ + jets channel.

	N_{jet}=0	N_{jet}=1	N_{jet}=2	N_{jet}=3	N_{jet}=4	N_{jet}=5
QCD Fraction (W)	0.0174	0.1168	0.1051	0.0984	0.0701	0.0483
QCD Fraction (Z)	0.0036	0.0052	0.0087	-	-	-

Table 5.2: Nominal QCD fractions obtained from the template fits for exclusive jet multiplicity bins in the $W \to \mu\nu$ + jets (once the E_T^{miss} requirement had been reapplied) and $Z \to \mu\mu$ + jets channels.

channel, the fit was performed for exactly 0-5 jets and in the $Z \to \mu\mu$ + jets channel for 0-2 jets. For exclusive jet multiplicities above 5 (or above 2 in the $Z \to \mu\mu$ + jets channel), the QCD template statistics are insufficient for a stable fit. Therefore, the scale factor for exactly 5 jets (or exactly 2 jets for the $Z \to \mu\mu$ + jets channel) was applied to all higher jet multiplicity bins.

Figures 5.1 and 5.2 respectively show the E_T^{miss} and $M_{\mu\mu}$ distributions for data (with the E_T^{miss} cut removed in the former) and the fit result for the QCD and Sig+Bkg event templates. Table 5.2 shows the value of the QCD fractions obtained for the exclusive jet multiplicity bins in each channel.

To obtain the shape of the QCD background for each variable considered in this analysis, the QCD control sample selection was applied to data (in the $W \to \mu\nu$ + jets channel the signal selection E_T^{miss} requirement was applied). The Sig+Bkg contamination was estimated by applying the QCD selection to the relevant Monte Carlo simulations, and a bin-by-bin histogram subtraction from the control data distribution was performed. The resultant data distributions were then scaled by the QCD normalisation factor provided by the template fits, relevant to the jet multiplicity bin. This yielded the size and shape of the QCD background contribution for each kinematic variable.

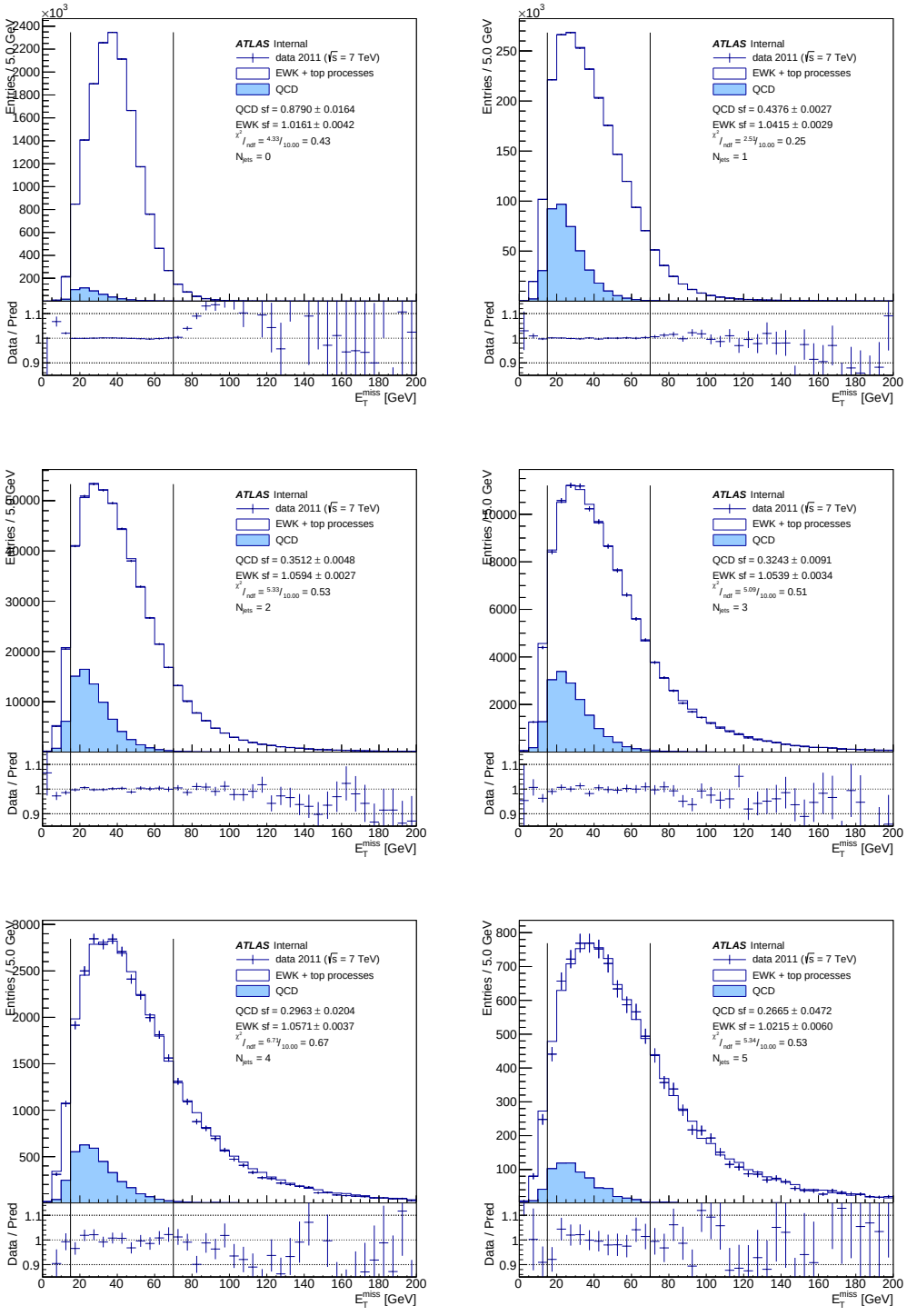

Figure 5.1: Template fits to the E_T^{miss} distribution for exclusive jet multiplicities 0-5, in the $W \to \mu\nu$ + jets channel. Here "EWK + top processes" refers to the $(\text{Sig+Bkg})^{\text{SS}}$ template.

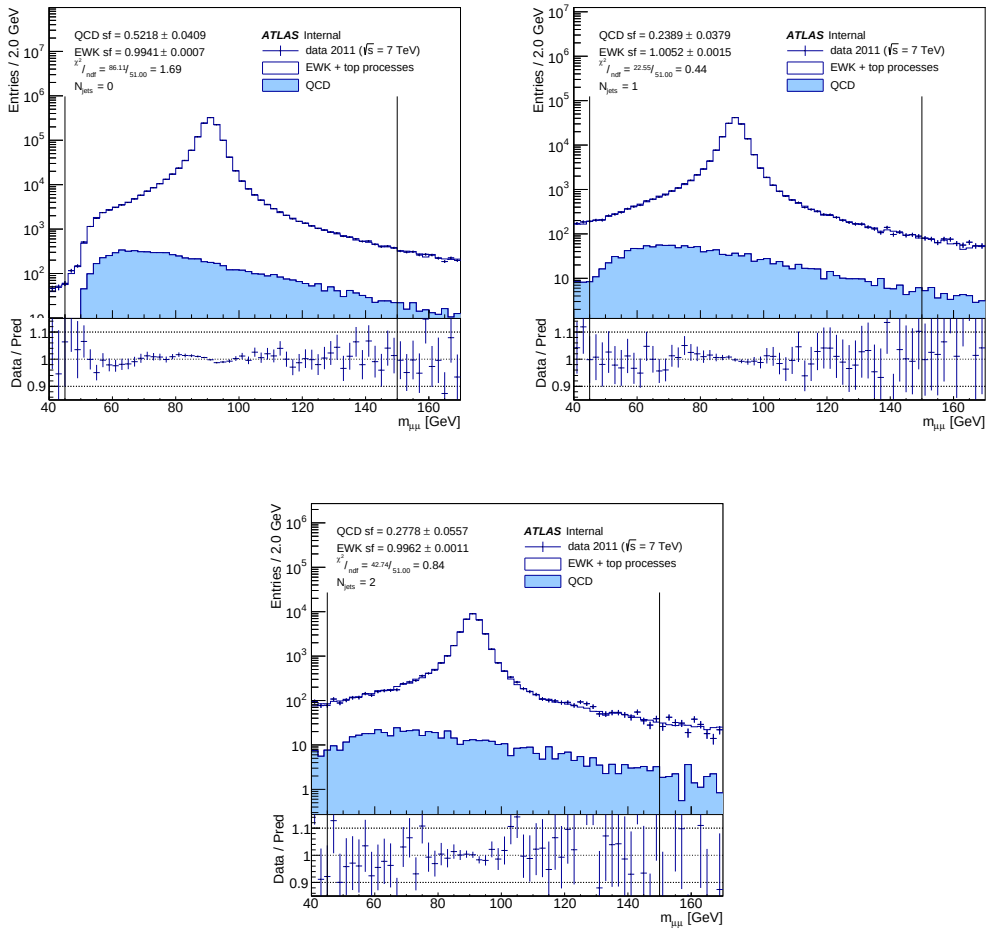

Figure 5.2: Template fits to the $M_{\mu\mu}$ distribution for exclusive jet multiplicities 0-2, in the $Z \to \mu\mu$ + jets channel. Here "EWK + top processes" refers to the $(\text{Sig+Bkg})^{\text{SS}}$ template.

5.1.2 Electron Channel

In the $W \rightarrow e\nu$ + jets channel, QCD events contaminate the signal mainly by mismeasured jets that fake an electron. A mismeasured jet can also affect the E_T^{miss} in an event. In the $Z \rightarrow ee$ + jets channel, events with two jets can contaminate the signal if both jets fake an electron and their reconstructed mass is within the invariant mass range around the Z mass peak used in the analysis. A very large Monte Carlo sample would be required to provide enough events to simulate the multi-jet background in the electron channel. For this reason, and the presence of large jet cross-section uncertainties, a data-driven technique was employed to estimate the QCD background in this channel. A similar approach was applied as in the muon channel. Again, a QCD-enriched control sample was selected from data, and a control template was extracted. Fits to the E_T^{miss} and M_{ee} distributions were then performed in the $W \rightarrow e\nu$ + jets and $Z \rightarrow ee$ + jets channels respectively.

5.1.2.1 Selection of Control Sample

The QCD control sample was selected from data acquired using "loose" electron triggers. During the 2011 ATLAS data taking period, the conditions for pile-up events changed substantially and the increase in additional jets affected the shape and rate of the QCD background. For this reason, in the electron channel the data was split into two sections, corresponding to earlier data taking periods (D-K) and later periods (L-M). The fit was performed separately for each of the datasets before combining them to provide a QCD estimate for the whole of the 2011 dataset.

For the $W \rightarrow e\nu$ + jets channel, the electron identification criteria were relaxed from the tight selection used for the signal selection. We required only that an electron pass the loose, and a subset of the medium, identification requirements, and that it failed the tight criteria. The electrons were also subjected to a calorimeter-based anti-isolation requirement that the to-

tal energy deposited within a cone of size ΔR=0.3 be more than 20% of the energy of an electron, i.e. $\Sigma E_T^{cone30}/E_T^{elec} > 0.2$. The values of this anti-isolation requirement were chosen based on four criterion: the goodness of the fit, the (Sig+Bkg)^{SS} and QCD normalisation scale factors returned from the fit, and the amount of Sig+Bkg contamination entering the QCD control sample. Variations on the anti-isolation requirement were used as alternative templates to evaluate the systematic uncertainty associated with the choice of $\Sigma E_T^{cone30}/E_T^{elec} > 0.2$.

In the $Z \rightarrow ee$ + jets channel, the control sample was selected by using a loose trigger and requiring that both electrons pass the loose identification criteria while failing the medium criteria.

5.1.2.2 Fit Results

The electron channel fit was performed in a very similar way to the muon channel fit described above. The $W \rightarrow e\nu$ + jets channel fit to E_T^{miss} (with the E_T^{miss} requirement removed) was performed over the range [15, 80] GeV for exactly 0-5 jets, and the $Z \rightarrow ee$ + jets channel fit to M_{ee} over [50, 140] GeV for exactly 0-2 jets. For the $Z \rightarrow ee$ + jets channel fit, the region around the Z mass peak was highly contaminated by signal processes and was thus dependent on Monte Carlo modelling of the signal template. For this reason the region around the Z peak was removed from the fit. Table 5.3 shows the QCD fractions obtained in exclusive jet multiplicity bins for both channels. The shape of the QCD background for each variable in the analysis was determined in exactly the same way as for the muon channel, as described in Section 5.1.1.3.

	N_{jet}=0	N_{jet}=1	N_{jet}=2	N_{jet}=3	N_{jet}=4	N_{jet}=5
QCD Fraction (W): D-K	0.0295	0.0786	0.0827	0.0803	0.0615	0.0665
QCD Fraction (W): L-M	0.0540	0.1443	0.1496	0.1370	0.0821	0.0536
QCD Fraction (W): Combined	0.0420	0.1147	0.1187	0.1112	0.0724	0.0599
QCD Fraction (Z)	0.0020	0.0021	0.0044	-	-	-

Table 5.3: Nominal QCD fractions obtained from the template fits for exclusive jet multiplicity bins in the $W \to e\nu$ + jets (once the E_T^{miss} requirement had been reapplied) and $Z \to ee$ + jets channels.

5.1.3 Systematic Uncertainties

In both lepton channels, four sources of systematic uncertainty were considered in evaluating the overall uncertainty on the QCD background estimation. An additional systematic associated with electron identification was included in the electron channel only. Furthermore, the effect of the detector-level systematic variations (i.e. those discussed in Section 4.3) on the QCD background estimate was evaluated by varying the Monte Carlo templates and repeating the fit. The latter systematic variations are not included in the QCD error band, rather they are propagated through the analysis. Figure 5.3 shows the fractional uncertainties on the QCD background associated with the method of estimation, for the $W \to \mu\nu$ + jets channel. Table 5.4 relates the corresponding breakdown in terms of percentage error on the nominal result. The QCD systematics considered were:

Fit Range: A systematic was assigned to the choice of fit range by varying the nominal fit range, performing the fit and taking an envelope of the overall maximum and minimum values from the varied fit results. In the $W \to \mu\nu$ + jets channel, the nominal fit range of [15, 70] GeV was varied by taking a

minima of 10 and 20 and a maxima of 50 and 90 GeV, all combinations with the nominal minima and maxima were considered. In the $Z \rightarrow \mu\mu$ + jets channel, the nominal range of [45, 150] GeV was varied using 40 and 50 GeV as minima and 145 and 155 GeV as maxima. For the $W \rightarrow e\nu$ + jets and $Z \rightarrow ee$ + jets channels, the nominal ranges of [15, 80] GeV and [50, 140] GeV respectively were varied using minima of 10 and 20 GeV for W, 45 and 55 Gev for Z, and maxima of 60 and 100 GeV for W, and 135 and 145 GeV for Z.

Choice of Template: Alternative templates were used to evaluate the systematic uncertainty associated with the choice of QCD control sample. The fit was performed for each template and again an envelope of the minimum and maximum deviations from the nominal fit value was taken as the overall systematic uncertainty. In the muon channel, the alternative templates were taken from those listed in Section 5.1.1.2, specifically in the $W \rightarrow \mu\nu$ +jets channel, **AntiD0WithIso_D0Window** and **RestrAntiIso** were taken as the alternatives, and for $Z \rightarrow \mu\mu$ **AntiD0NoIso** and **AntiIsoWithD0** were used. In the $W \rightarrow e\nu$ channel, alternative control sample selections were employed by varying the parameters of the nominal isolation requirement ($\Sigma E_T^{cone30}/E_T < 0.2$). The cone size was varied up and down to values of 0.4 and 0.2 respectively, and the cut value was varied to 0.15 and 0.25. The difference between calorimeter and track based isolation was also included as a source of systematic uncertainty.

Electroweak Background Modelling: A systematic associated with the choice of Monte Carlo generator for the Sig+Bkg samples was determined by using an alternative template from samples generated using SHERPA. The value of the systematic uncertainty was taken as the difference between the fit results using this template, and that generated using the nominal ALPGEN+HERWIG template. This approach was applied to both W and Z channels in each lepton channel.

Statistical Uncertainty: The final QCD background systematic uncertainty, common to both lepton channels, was the statistical uncertainty on the QCD scale factors returned by the fitting tool. This is a small uncertainty that only becomes significant in bins of higher jet multiplicity.

Electron Identification: One source of systematic uncertainty was considered in the electron channel only, this related to the choice of tight identification criteria the electron was required to fail. Alternative templates were created for which the failure of certain tight identification cuts was not required. The fit was performed for each alternative template and an envelope of the maximum and minimum deviations from the nominal result was taken as the overall systematic associated with electron identification.

Systematic	N_{jet}=0	N_{jet}=1	N_{jet}=2	N_{jet}=3	N_{jet}=4	N_{jet}=5
Fit Range Up	0.0393	0.0069	0.0092	0.0231	0.0863	0.2306
Fit Range Down	0.0289	0.0058	0.0049	0.0122	0.0033	0.0428
Template Up	0.0314	0.0327	0.0418	0.0405	0.0717	0.0
Template Down	0.0	0.0	0.0	0.0	0.0	0.0665
Statistics Up/Down	0.0186	0.0061	0.0136	0.0281	0.0689	0.1773
Bkg Modelling Up	0.0685	0.0	0.0	0.0	0.0	0.0
Bkg Modelling Down	0.0	0.0307	0.0116	0.0811	0.0326	0.0313
Total Up	0.087	0.034	0.0449	0.0544	0.1317	0.2909
Total Down	0.0344	0.0318	0.0185	0.0867	0.0763	0.1966

Table 5.4: Fractional systematic uncertainties on the QCD background estimation in the $W \to \mu\nu$ + jets channel (once the E_T^{miss} cut has been reapplied).

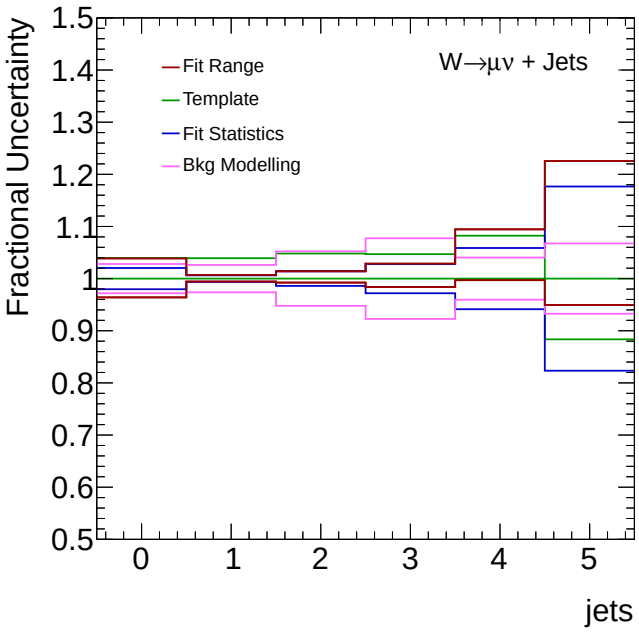

Figure 5.3: Percentage uncertainties on the nominal QCD fraction in the $W \to \mu\nu$ + jets channel.

5.2 $t\bar{t}$ Background

Figure 5.4 depicts the decay of a $t\bar{t}$ pair to a final state with two W bosons and two b quarks. When the b quarks decay hadronically, events of this type can have a final state that includes a W decaying into a lepton and neutrino, with associated hadronic jets from the b quarks. This final state signature is indistinguishable from W$\to l\nu$ + jets events this analysis aims to measure. For events with four or more jets, such decays become the dominant background process contaminating the signal in the W+jets channel. The proportion of this background increases with increasing jet multiplicity. It was therefore very important for this analysis to have a good understanding of the shape of this background.

Previous analyses estimated this background using Monte Carlo simulations. However, such estimations were plagued by large systematic uncertainties from a variety of sources, including the uncertainty on the cross-section for

top production and the propagation of the jet energy scale uncertainty through the Monte Carlo background estimate. The resultant systematic uncertainty for the W+jets analysis with 35 pb^{-1} of data was nearly 40% in the 4-jet bin. In order to reduce this large uncertainty on the $t\bar{t}$ background estimation for the W+jets channel, a data-driven technique was employed[4]. The general approach was the same as for the data-driven QCD background estimation described in Section 5.1:

1. A control sample enriched in $t\bar{t}$ events was selected from data.

2. A variable was chosen with the power to discriminate between the shape of $t\bar{t}$ events, W signal, electroweak and multi-jet QCD events (referred to here as Sig+EWK+QCD). The $t\bar{t}$ control template was extracted from the control sample by subtracting the (Sig+EWK+QCD)^{CS} distribution (formed by applying the control sample selection to Sig+EWK+QCD events) from the control sample distribution for the discriminating variable. This was a bin-by-bin histogram subtraction.

3. A maximum likelihood fit was performed to fit the $t\bar{t}$ control template and the Sig+EWK+QCD template from the signal selection (referred to as (Sig+EWK+QCD)^{SS}) to the distribution of data from the signal selection, data^{SS}. This yielded total normalisation scale factors for the contribution of $t\bar{t}$ events to data^{SS}.

4. The shape of the $t\bar{t}$ background for each kinematic variable in the analysis was extracted by applying the control sample selection to data and removing contamination by subtracting the kinematic distribution from the (Sig+EWK+QCD)^{CS} sample. Finally, the relevant normalisation

[4]For the Z channel, this analysis estimated the $t\bar{t}$ contribution using Monte Carlo simulation with samples from the ALPGEN+HERWIG+JIMMY generators. This is justified since the Z channel analysis is performed within a lower inclusive jet multiplicity range (up to 4 jets), and the Monte Carlo simulations provide a reliable estimation of $t\bar{t}$ production in this region. Furthermore, the $t\bar{t}$ background in the Z+jets channel is comparatively small.

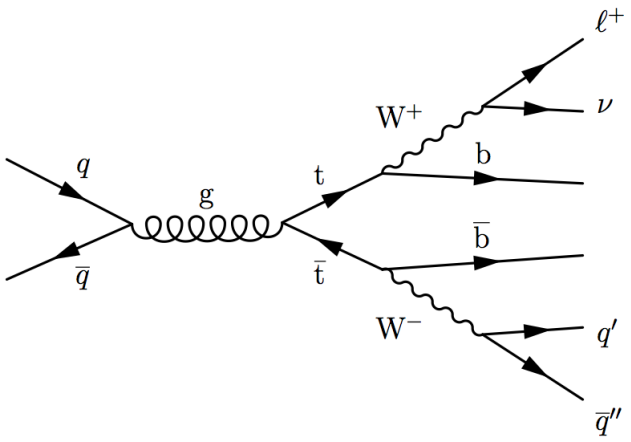

Figure 5.4: Feynman diagram depicting semileptonic top decay arising from quark-anitquark annihilation.

scale factor was applied to the control sample distribution to provide the $t\bar{t}$ background distribution for each kinematic variable.

Unlike for the QCD estimate, the primary challenge was not the selection of a suitable control sample of $t\bar{t}$ events, rather choosing a variable with the power to discriminate between the shape of $t\bar{t}$ events and the shape of our W+jets signal events. For this part of the analysis, Sig+EWK processes were modelled using Monte Carlo simulation, and the shape of QCD events was taken from the data-driven estimation described in Section 5.2.

5.2.1 Selection of Control Sample

The selection of a top enriched data control sample was readily achieved by exploiting top quark decay via $t \rightarrow Wb$. As such there are always two b quarks in the event which decay hadronically. No b-tagging requirements were included in the signal selection. Therefore, it was sufficient to require at least one b-jet in an event to select a data sample of predominantly top events that will also model well the expected kinematic distributions for top background.

The MV1 b-tagging algorithm [74] was used to select events with at least one b-jet, with three different tagging criteria (tight, medium and loose) con-

sidered. The requirement of at least two b-jets was also investigated for the control sample selection. W events from signal processes, electroweak background processes and multi-jet background processes contaminate this sample of $t\bar{t}$ events. Checking all combinatorics of tagging criteria and number of b-jets mentioned above yielded an optimal selection of medium tagging criteria and requiring at least one b-jet. This selection provided the optimal purity of the $t\bar{t}$ sample because it had an acceptable level of background contamination from W events (as estimated using Monte Carlo). Furthermore, the event selection requiring two b-jets distorted some kinematic distributions in the control sample, with respect to the signal selection.

At low jet multiplicities, the non-negligible W contamination was dominated by W+c, W+cc, W+bb events. Such events, along with single top and electroweak processes, were removed from each distribution of the control sample. This was achieved by a bin-by-bin histogram subtraction of the (Sig+EWK)^{CS} sample from the control sample. Contamination from QCD events was also subtracted using a QCD estimation from data, using the same method as described in Section 5.2 but also including the above b-tagging requirement applied to the QCD control sample selection.

The process of b-tagging introduced a small bias in the control sample with respect to a non-b-tagged inclusive $t\bar{t}$ Monte Carlo sample. The size of this bias was evaluated using Monte Carlo, by comparing the difference between distributions from an inclusive top sample with and without the b-tagging requirement applied. The bias was due to a lack of b-tagging available beyond the tracking acceptance. Correction factors were derived from ALPGEN $t\bar{t}$ Monte Carlo by taking the ratio of the number of inclusive $t\bar{t}$ events to the number of b-tagged $t\bar{t}$ events. They were then applied to the control sample to correct for this bias.

5.2.2 Discriminating Variable

A suitable variable had to be chosen which provides good separation between the shape of the $t\bar{t}$ events and signal events. A maximum likelihood fit could then be performed over this variable to estimate the normalisation of $t\bar{t}$ events to the signal data selection. This proved somewhat problematic since the top decays to a W, therefore the kinematic distributions of the two types of event are very similar. A number of different variables were considered to perform the fit, and Monte Carlo samples for W signal and $t\bar{t}$ events were used to determine the discriminating power of each variable for different jet multiplicities.

The first two variables to be considered were lepton η and top mass, calculated using 3 jets that yield the highest summed P_T. The former was tested because leptons produced in $t\bar{t}$ events are more central than those in W+jets events [75]. Lepton η provided good separation but was deemed too sensitive to the PDF used for the W signal Monte Carlo. The top mass gave the best overall separation but was also too sensitive to fluctuations in the shape of the W signal template, arising from jet energy scale and other uncertainties.

The E_T^{miss} in an event was tested and demonstrated the best power of separation for low jet multiplicities, but the top and W signal shapes became increasingly similar with increasing jet multiplicity. This is because of the two W bosons produced in $t\bar{t}$ decay, we required only one to decay leptonically. The other W boson can also decay leptonically and be a source of extra E_T^{miss}. With increasing jet multiplicity, the $t\bar{t}$ events that will be more likely to pass the signal selection will be those in which the second W boson decayed hadronically, in this case there is no extra E_T^{miss}.

The next variable considered was transverse sphericity: the summed P_T^2 in an event with respect to the event axis. The lepton and all jets passing the event selection, and the E_T^{miss} in an event are included in the momentum tensor used for the calculation of transverse sphericity. Transverse sphericity takes values between 0 (pencil-like events) and 1 (isotropic events) [75]. Because $t\bar{t}$

pairs are produced with back-to-back topology, the summed P_T^2 of all decay products is likely to be more isotropic and therefore take higher values of transverse sphericity. W signal events will be less isotropic and take lower values of transverse sphericity than $t\bar{t}$ events. Transverse sphericity provided good separation for all jet multiplicities, but the region of good separation was limited to the range [0.0, 0.4] of this variable.

The final variable considered was transformed aplanarity: defined as $e^{-8 \cdot A}$, where aplanarity $A = 3\lambda_3$ and λ_3 is the smallest eigenvalue of the normalised momentum tensor. As for transverse sphericity, the momentum tensor includes the lepton and all jets passing the selection. The choice of transformed[5] aplanarity was based on a similar rationale as for transverse sphericity, i.e. $t\bar{t}$ events will be more isotropic [75]. Transformed aplanarity provided a good overall separation and is largely stable against fluctuations in the W template arising from jet energy scale and other uncertainties. It was therefore decided to use this variable for the fit.

5.2.3 $t\bar{t}$ Fit

The fit was performed using RooFit [76]. As with the QCD estimation, the normalisation of the control and (Sig+EWK+QCD)^{SS} templates was varied to provide the best fit with the data^{SS}. The relevant normalisation scale factors for each contribution were thus extracted. At values of transposed aplanarity above 0.9 the effect of jet energy scale variations became significant, therefore the fitting range was chosen to be [0.0, 0.85]. Figure 5.5 shows the fit to transposed aplanarity in the muon W channel, for the N_{jet}=3 and N_{jet}=5 bins.

To estimate the shape and size of the $t\bar{t}$ contribution for each variable measured in this analysis, the control sample selection was first applied to data.

[5]The transformed quantity is used instead of aplanarity directly in order to increase the separation in the aplanarity distribution between $t\bar{t}$ and signal events.

The (Sig+EWK+QCD)^{CS} sample was subtracted via bin-by-bin histogram subtraction to remove contamination. The scale factors for the $t\bar{t}$ contributions extracted from the fit were then applied to data, in the relevant jet multiplicity bin.

One issue with this procedure was that, unlike the method for QCD estimation, the control sample was a subset of the data signal sample, i.e. they were not mutually exclusive. This means that the $t\bar{t}$ template was statistically correlated with data signal template. Therefore, RooFit may underestimate the statistical uncertainty on the fit. The correlation between the two templates is somewhat loosened by:

- The b-tagging correction factors (described in Section 5.2.1).
- The bin-by-bin contamination subtraction of (Sig+EWK+QCD)^{CS} from the control sample.
- The fact that the top template is only a partial subset of the full signal region.

Nevertheless, the statistical uncertainty on the method was checked by using a toy Monte Carlo procedure to evaluate the statistical correlation between the $t\bar{t}$ template and the data signal template (the full details of the procedure are described in [77]).

5.2.4 Systematic Uncertainties

Five sources of systematic uncertainty on the method for estimating the $t\bar{t}$ background were evaluated, the total systematic uncertainty associated with the method was then taken as their quadratic sum. Figure 5.6 shows the breakdown of $t\bar{t}$ systematics for the electron and muon W channels, and Table 5.5 relates the corresponding numerical breakdown, along with the $t\bar{t}$ fractions obtained from the fit. The systematics considered were:

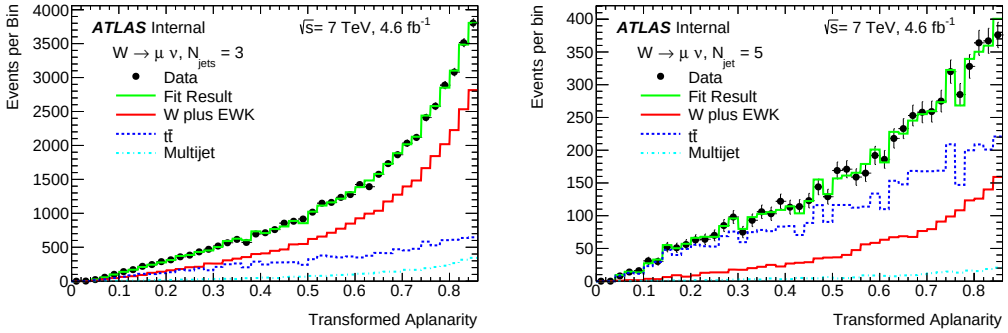

Figure 5.5: Template and results of the data-driven $t\bar{t}$ fits in the N_{jet}=3 (left) and N_{jet}=5 (right) bins, in the muon W channel. Errors on data points are statistical only. For jet multiplicity lower than 3, the $t\bar{t}$ background is taken from Monte Carlo simulation. Plots taken from [77].

Model uncertainty on the subtracted b-tagged W signal: As mentioned above, at lower jet multiplicities (3 or 4 jets) there was a significant contamination from W+c, W+cc and W+bb events which was subtracted using ALPGEN Monte Carlo. The modelling of the heavy flavour contamination has an associated systematic uncertainty which was evaluated by applying normalisation to the heavy flavour distributions. Studies showed that W+cc and W+bb distributions had similar shapes to each other in many kinematic distributions, whereas W+c were different. For this reason, one normalisation was estimated for the W+cc and W+bb contribution, and a separate one was estimated for W+c. The b-tagged data and Monte Carlo samples were compared in the 1-jet and 2-jet bins, and normalisation factors were calculated such that the total number of events in the Monte Carlo samples equalled the total in data. The normalisation factors were then applied to the relevant heavy flavour samples, and the subtraction from the control sample and subsequent fit were performed again to evaluate the overall effect of this uncertainty.

Choice of fit range: The systematic associated with the choice of fitting range was determined by varying the upper limit of the fit from 0.85 to 0.83 and 0.87.

b-tagging correction factors: As mentioned in Section 5.2.1, the b-tagging requirement in the control sample selection introduced a small bias with respect to a non-b-tagged inclusive $t\bar{t}$ sample. The correction factors that were applied to the control sample had an associated systematic uncertainty. The nominal corrections were derived using ALPGEN Monte Carlo and were compared to an alternative set of correction factors derived using POWHEG-BOX Monte Carlo. If the difference between the two sets of corrections was not statistically significant then the uncertainty on the correction was simply the statistical uncertainty on the nominal corrections, otherwise the uncertainty was taken as the size of the difference between ALPGEN and POWHEG-BOX corrections.

b-tagging uncertainty on the subtracted W signal: The control sample contamination from W signal events was estimated using Monte Carlo and subtracted from the sample of $t\bar{t}$ events. This W signal sample suffers from tagging uncertainties, the effects of which were evaluated by applying ATLAS standard uncertainties for b-tagging, c-tagging and light flavour-tagging. For each of the three sources of uncertainty, the W signal sample was varied up and down before subtraction. Each variation was performed independently, the uncertainties derived from each were then added in quadrature.

Statistical uncertainty: The statistical uncertainty on the fit was also included as a uncertainty on the value of the estimated $t\bar{t}$ background.

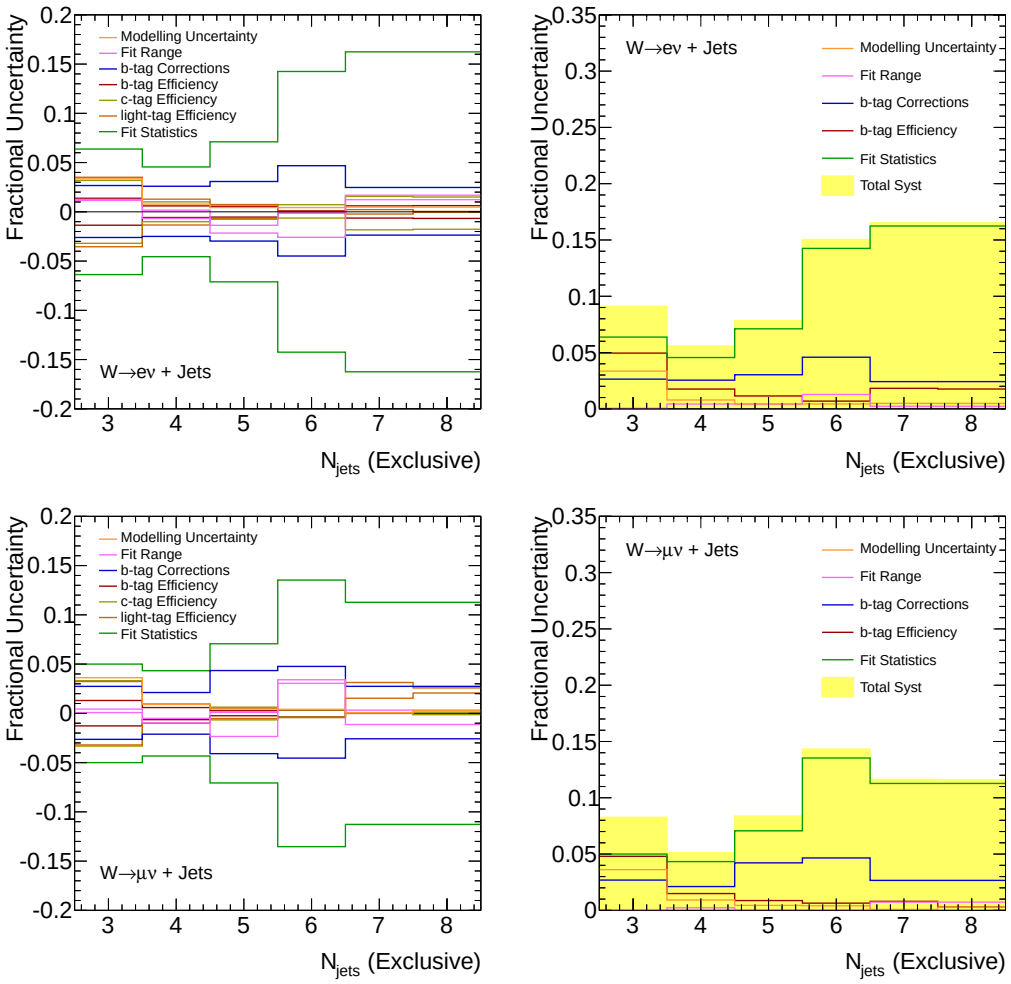

Figure 5.6: Fractional uncertainties on the nominal $t\bar{t}$ fraction in the $W \to e\nu$ + jets (top) and $W \to \mu\nu$ + jets (bottom) channels. Left: Up and Down variations for all systematics on the estimation method. Right: Fully symmeterised variations and the quadratic sum.

Systematic	N_{jet}=3	N_{jet}=4	N_{jet}=5	N_{jet}=6	N_{jet}=7
$W \to e\nu$ + jets					
Fitted top fraction	0.25	058	0.71	0.87	0.76
Model Norm. W+c	-3.22	-0.69	-0.33	-0.39	-0.03
Model Norm. W+bb(cc)	0.93	0.37	0.29	0.19	0.48
Fit Range Up	1.16	-0.68	-2.16	-2.58	1.23
Fit Range Down	1.25	0.17	-1.37	-0.04	1.69
b-Tag Corr. Up	-2.61	-2.5	-2.97	-4.49	-2.36
b-Tag Corr. Down	2.67	2.6	3.08	4.68	2.47
b-Efficiency Up	-1.36	-0.58	-0.53	0.1	-0.63
b-Efficiency Down	1.38	0.6	0.53	-0.1	0.61
c-Efficiency Up	-3.2	-1.01	-0.68	-0.63	-1.83
c-Efficiency Down	3.19	1.01	0.69	0.72	1.56
light-Efficiency Up	-3.55	-1.34	-0.74	-0.02	-0.02
light-Efficiency Down	3.51	1.28	0.74	0.04	0.22
Fit Statistics Up/Down	6.37	4.56	7.11	14.25	16.24
$W \to \mu\nu$ + jets					
Fitted top fraction	0.28	057	0.69	0.73	0.81
Model Norm. W+c	-3.54	-0.78	-0.35	-0.27	0.07
Model Norm. W+bb(cc)	0.99	0.44	0.27	0.3	0.04
Fit Range Up	0.45	-0.93	0.14	3.76	-1.12
Fit Range Down	0.0	-0.52	-2.25	3.54	0.33
b-Tag Corr. Up	-2.64	-2.03	-4.11	-4.51	-2.54
b-Tag Corr. Down	2.76	2.09	4.39	4.86	2.65
b-Efficiency Up	-1.3	-0.59	-0.25	-0.36	0.0
b-Efficiency Down	1.33	0.64	0.26	0.35	0.0
c-Efficiency Up	-3.4	-0.95	-0.63	-0.38	-0.01
c-Efficiency Down	3.4	0.95	0.64	0.37	0.01
light-Efficiency Up	-3.26	-0.98	-0.54	-0.43	1.58
light-Efficiency Down	3.27	0.99	0.53	0.38	2.89
Fit Statistics Up/Down	4.99	4.32	7.03	13.56	11.19

Table 5.5: Fitted top fractions and the systematic uncertainties (quoted as total percentage error) on the $t\bar{t}$ background estimation in the electron and muon channels.

Chapter 6

Unfolding to Particle Level

The distributions shown in Section 4.5 are presented at detector level. This analysis aims to present the ratio of the $\frac{\text{W+jets}}{\text{Z+jets}}$ cross-sections at particle level[1]. Therefore, it was necessary to correct for detector effects such as the inefficiency with which ATLAS reconstructs the vector bosons and jets in an event. The process by which measured events are corrected to particle level is called "unfolding".

The simplest form of unfolding is a bin-by-bin correction for which the ratio of the Monte Carlo particle-level and reconstructed-level distributions is formed, and used to correct each bin of the measured data distribution. The limitation of this approach is that migrations of events between bins are not correctly accounted for. The next simplest approach would be to treat the problem as one of inverting a matrix which relates particle-level and reconstructed-level quantities. Again, this approach has its limitations rendering it unsuitable for this analysis; namely that it is strongly affected by large statistical fluctuations which may in turn be interpreted as real structure. This would be a large problem, since the migration matrices were formed

[1]As described here, the leptons at particle level are "dressed", i.e. the lepton kinematics include the four-momentum of the photons radiated within a cone of radius 0.1 around the final state lepton direction. Particle-level jets are clustered from final state hadrons and their decay products, this excludes the dressed W and Z-decay products.

from Monte Carlo with limited statistics. Therefore, in this analysis, unfolding was achieved by using a Bayesian iterative procedure utilising Monte Carlo samples.

This chapter describes the rationale behind Bayesian unfolding, the method by which unfolding was performed in this analysis, and the systematic uncertainties associated with that method. Finally, unfolded electron channel data distributions are presented, for both the W+jets and Z+jets channels[2].

6.1 Bayes' Theorem

Given a probability space, P(S), with two subspaces, P(A) and P(B), Bayes' theorem of conditional probability describes the probability that an event will occur in space A, given that it has occurred in space B, provided that A and B overlap:

$$P(A \mid B) = \frac{P(A \cap B)}{P(B)} \tag{6.1}$$

Likewise, the probability that an event occurs in space B given it has occurred in space A can be written as:

$$P(B \mid A) = \frac{P(B \cap A)}{P(A)} \tag{6.2}$$

$A \cap B$ and $B \cap A$ are equivalent and as such we can combine Equations 6.1 and 6.2 to form the equation relating $P(A \mid B)$ and $P(B \mid A)$. This is known as Bayes' theorem:

[2]The plots shown in Section 6.5, and in Chapter 8, were created using a common plotting macro for the purposes of presenting the final combined ratio results, to which the author contributed some cosmetic work. They are therefore not the sole product of the author's work. For the plots shown, the author contributed the full set of electron channel unfolded data distributions, and for each distribution the full propagation of each individual systematic uncertainty source through the unfolding. Here the author also contributed the electron channel particle-level ALPGEN and SHERPA distributions, and for each distribution the corrections to BLACKHAT+SHERPA discussed in Sections 7.2.2.2 and 7.2.2.3.

$$P(A \mid B) = \frac{P(B \mid A)P(A)}{P(B)} \tag{6.3}$$

In Equation 6.3, P(A) is referred to as the *prior*, that is, the initial estimation of the probability of an event occurring in space A. $P(A \mid B)$ is referred to as the *posterior*, the updated probability of A, given what is known about P(B). Equation 6.3 can be further generalised by treating the total probability space P(S) as a sum of disjoint subsets, A_i, and as such we can form the law of total probability:

$$P(A \mid B) = \frac{P(B \mid A)P(A)}{\Sigma_i P(B \mid A_i)P(A_i)} \tag{6.4}$$

Thus Equation 6.4 can provide a powerful tool for making statistical inferences about hypotheses, given experimental observations.

6.1.1 Practical Application of Bayes' Theorem

We wish to employ Bayes' Theorem for the means of this analysis, i.e. to correct the measured data for known detector effects and acceptances, in order to retrieve the particle-level data distribution. Therefore, it is necessary to formulate Equation 6.4 in terms of binned histograms. In this case, the posteriors are elements of a Monte Carlo-based unfolding matrix, M_{ij}^{MC}. The matrix describes the probability, $P(T_I^{MC})$, of an event existing in bin i of a particle-level histogram, T_i^{MC}, given that the event lies in bin j of the reconstructed-level histogram, R_j^{MC}. Written in the nomenclature of conditional probability the unfolding matrix elements describe $P(T_i^{MC} \mid R_j^{MC})$. We can therefore rewrite Equation 6.4 in these terms to yield:

$$P(T_i^{MC} \mid R_j^{MC}) = \frac{P(R_j^{MC} \mid T_i^{MC})P(T_i^{MC})}{\Sigma_{i'} P(R_j^{MC} \mid T_{i'}^{MC})P(T_{i'}^{MC})} \tag{6.5}$$

where $P(R_j^{MC} \mid T_i^{MC})$ are elements of a response matrix, a description of the probability of measured data, given the particle-level distribution. Here

$P(T_i^{MC})$ acts as the prior knowledge and relates to elements of a 1-dimensional particle-level histogram from a suitable Monte Carlo physics model.

Finally, the unfolding matrix can be applied to the measured data distribution, R_j^{Data}, to correct for detector effects and yield the unfolded particle-level distribution:

$$U_i^{Data} = \Sigma_j P(T_i^{MC} \mid R_j^{MC})(R_j^{Data}) \tag{6.6}$$

The distribution U_i^{Data} can be then be used for comparisons with theoretical predictions. This very useful application of Bayes' theorem to the unfolding of experimental data was first proposed by D'Agostini [78].

6.2 Unfolding Method

The iterative Bayesian unfolding technique described in the previous section was implemented using the RooUnfold package [79]. RooUnfold provides a C++ based framework. It takes as inputs ROOT ntuples containing the particle-level and reconstructed-level Monte Carlo distributions (T^{MC} and R^{MC}), the response matrix (as described in the previous section) and the observed data distribution (R^{Data}) for each observable.

At this stage in the analysis, R^{Data} refers to the distribution of data events that pass the event selection described in Section 4.3, and after a bin-by-bin histogram subtraction of all background distributions. The background distributions are those estimated by Monte Carlo simulation (as described in Section 4.1), and the QCD and $t\bar{t}$ background distributions obtained through the methods described in Chapter 5.

As can be seen from Equation 6.5, the solution to the unfolding matrix depends on the particle-level Monte Carlo. In order to reduce the dependence on the particle-level distribution, as simulated using Monte Carlo, an iterative procedure was used. For the first iteration of this technique, T_i^{MC} was used as the prior in Equation 6.5. U_i^{Data} was then computed from Equation 6.6,

and was in turn used as the prior for the subsequent iteration and so on. The number of iterations performed therefore acted as a regularisation parameter, defining the relative weight of the Monte Carlo particle-level sample, compared to the data. If this regularisation parameter has a small value, it indicates favour towards Monte Carlo, with larger values favouring more the data. It is preferable to have the smallest possible dependence on a prior physics model. However, with an increasing number of iterations, the statistical uncertainty associated with the Monte Carlo sample used increases. The value of the regularisation parameter was therefore chosen to reflect the balance between reducing Monte Carlo dependence on the unfolded data and keeping the size of the statistical uncertainty tolerable (this is discussed in the following sections).

ALPGEN Monte Carlo samples were used for the unfolding procedure described in this chapter. This is because ALPGEN was found to provide a satisfactory description of the measured detector-level distributions for the lepton and jet kinematics studied in this analysis (see Chapter 4)[3].

6.2.1 Response Matrices

For this analysis, the response matrix mentioned in the previous section was a 2-dimensional histogram filled with the numbers of ALPGEN Monte Carlo events at reconstructed-level and particle-level. Reconstructed-level and particle-level Monte Carlo events were required to have passed the event selection shown in Table 6.1. A separate matrix with specific binning was created and filled for each observable to be unfolded.

Figure 6.1 shows the electron channel response matrices for exclusive jet multiplicity, leading jet P_T and leading jet rapidity, in the both the W+jets and Z+jets channels. As presented here, the reconstructed values are given

[3]From the detector level distributions it was clear that ALPGEN provides a better description of the data than SHERPA. SHERPA was used for closure tests (described in Section 6.2.3), but the uncertainty associated with the Monte Carlo model was determined using ALPGEN samples with varied parameters (described in more detail in Section 6.3.2).

Selection	Acceptance Cuts
W$\to e\nu$	1 e with $P_T > 25$ GeV and $\|\eta\| < 2.47$, 1 ν with $P_T > 25$ GeV, $m_T > 40$ GeV
W$\to \mu\nu$	1 μ with $P_T > 25$ GeV and $\|\eta\| < 2.4$, 1 ν with $P_T > 25$ GeV, $m_T > 40$ GeV
Z$\to ee$	2 OS e with $P_T > 25$ GeV and $\|\eta\| < 2.47$ (excluding $1.37 < \|\eta\| < 1.52$), $66 < m_{ee} < 116$ GeV, $\Delta R(e,e) > 0.2$
Z$\to \mu\mu$	2 OS μ with $P_T > 25$ GeV and $\|\eta\| < 2.47$ (excluding $1.37 < \|\eta\| < 1.52$), $66 < m_{\mu\mu} < 116$ GeV, $\Delta R(\mu,\mu) > 0.2$
Jets	$P_T > 30$ GeV, $\|y\| < 4.4$ and $\Delta R(jet, l) > 0.5$

Table 6.1: Fiducial regions of measurement at particle level for different channels. "OS" refers to a selection of two leptons of opposite sign, i.e. e^+e^- or $\mu^+\mu^-$.

on the vertical axis, with the corresponding particle-level (or "hadron-level"), values are given on the horizontal axis. Each column has been normalised to the total number of particle-level events (for exclusive jet multiplicity), or total number of jets (for leading jet P_T and rapidity) that pass the acceptance selection for that particular bin. Therefore, the sum of all elements in a given column represents the reconstruction efficiency for that particle-level bin.

As expected, most events lie on the diagonal of the matrix, meaning that particle-level events are reconstructed in the same bin. However, non-negligible off-diagonal elements are visible for some distributions, particularly leading jet P_T. These elements represent the case where a particle-level event or jet has been reconstructed in a different bin, this is known as "migration". For jet P_T, matrix migrations can, and do, occur into and out of regions of the jet P_T spectrum lower than the analysis selection threshold (30 GeV). To account for such migrations, the jet P_T cut for the unfolding of jet P_T distributions was loosened to 20 GeV.

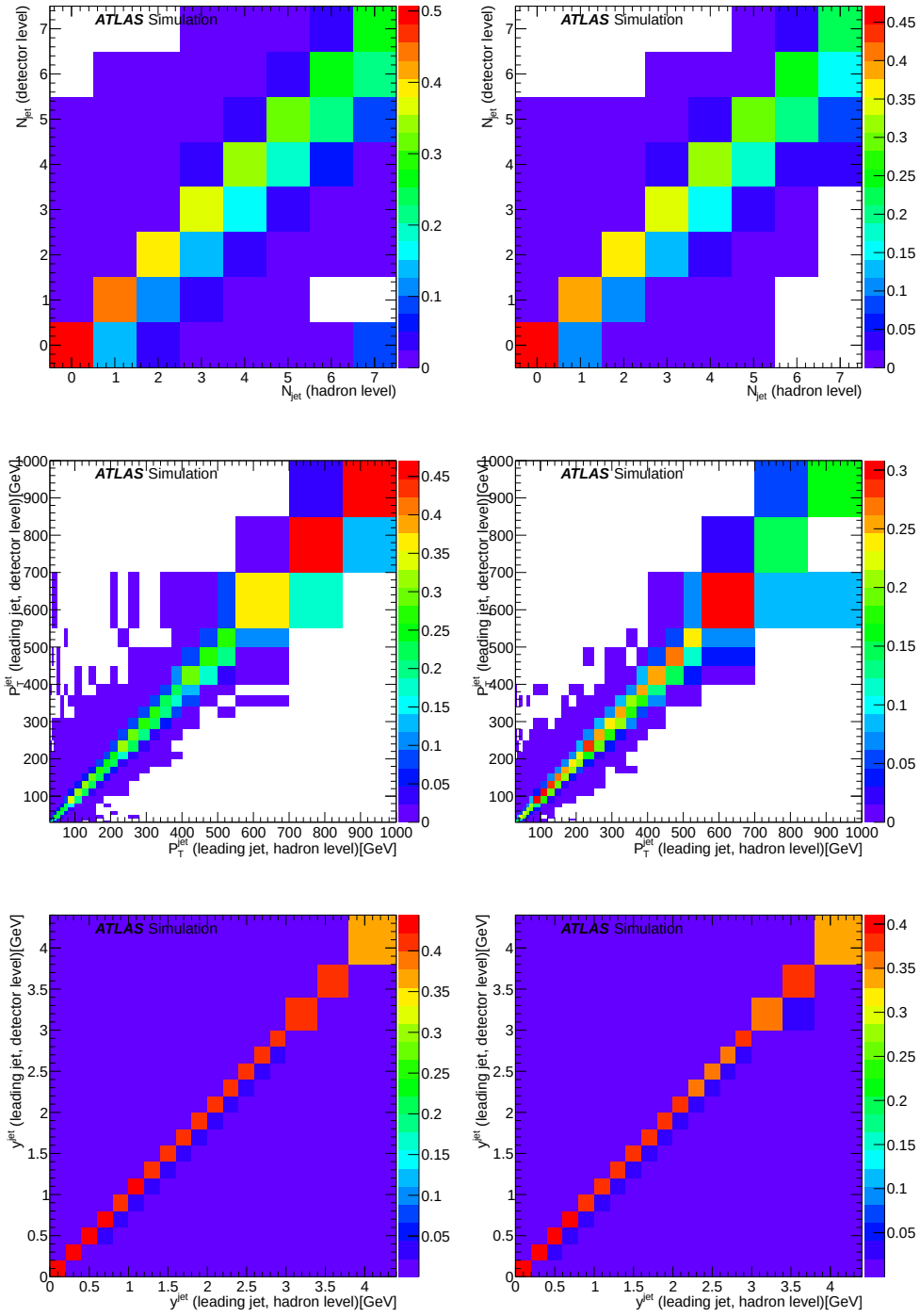

Figure 6.1: Electron channel response matrices for exclusive jet multiplicity (top), leading jet P_T (middle) and leading jet rapidity (bottom). Columns are normalised to the selection efficiency. Left: W+jets channel; Right: Z+jets channel.

6.2.2 Fake Corrections

Events outside of the analysis phase space at particle level can be reconstructed (migrate) into the fiducial phase space of the analysis at detector level. Such migrations lead to reconstructed distributions that contain extra events not present in the corresponding particle-level distribution. Excess reconstructed-level events can arise from a number of sources, including:

- Jets reconstructed above the P_T threshold of the analysis that nevertheless correspond to a particle-level jet below the threshold.
- Vector bosons passing the fiducial cuts at reconstructed level and failing at particle level.
- Pile-up jets.

A correction was calculated to account for the effect of such additional "fake" events on the unfolding procedure. A bin-by-bin fake correction was determined for each observable[4]. The correction was defined as the ratio of the number of events that pass both the reconstructed-level and particle-level selections to the total number of events that pass the selection at reconstructed level:

$$F^i_{corr} = \frac{\#\text{ events in bin } i \text{ that pass both reconstructed and particle-level selections}}{\text{Total }\#\text{ reconstructed events in bin } i} \tag{6.7}$$

The ratio was formed using ALPGEN signal Monte Carlo and applied before unfolding to both the data distribution R^{Data} (after background subtraction), and the reconstructed level Monte Carlo distribution, R^{MC}.

Figure 6.2 shows the size of the electron channel fake corrections for exclusive jet multiplicity, leading jet P_T and leading jet rapidity, in both the W+jets

[4]The fake correction was applied as a multiplicative factor, a correction close to one means the effective correction is small, i.e. the reconstructed distributions before and after correction are very similar.

and Z+jets channels. For the exclusive jet multiplicity correction, the numerator is the number of events that pass the boson selection at both reconstructed level and particle level. The denominator is the total number of events passing the boson selection at reconstructed level. For the leading jet P_T and rapidity corrections, the numerator requirements are extended to include events that not only pass the boson selection at reconstructed and particle levels, but also contain at least one reconstructed-level jet and at least one particle-level jet. The denominator in this case is the total number of reconstructed-level events passing the boson selection, with at least one reconstructed-level jet.

The rate of fake events (and therefore the size of the fake correction) is largely impacted by pile-up effects. This can be seen in Figure 6.2, in which large corrections in the low jet P_T region are observed. This is the kinematic region in which pile-up is most prominent. Furthermore, the large increase in the fake rate at a rapidity of about 2.5 represents the move from the central region of the detector to the end-caps, and a further increase in fake rate above about 3.8 represents the move from the end-caps to the forward region of the detector. The detector response for jets in the end-caps and the forward region is lower than in the central region, thus we see larger fake rates in these kinematic regions. For all distributions, the correction is consistently larger for the W+jets channel than for the Z+jets channel. This is once again is attributable to pile-up effects, which have a large impact on the reconstruction of missing transverse energy, essential for the reconstruction of the W boson.

At reconstructed-level, the jets used to build the response matrices and fake correction numerator were not required to match a particle-level jet within a specific cone. This approach corresponds to that used in the previous W+jets ATLAS analysis with the 2010 dataset [80]. In the previous Z+jets ATLAS analysis with the 2011 dataset [81], the matching procedure was employed. This alternative approach was investigated and compared with the nominal "no-matching" approach applied to this analysis. The impact was found to be negligible on the unfolded cross-section measurements.

Figure 6.3 shows the electron channel unfolded data distributions in the W+jets and Z+jets channel, for exclusive jet multiplicity, leading jet P_T and rapidity. Figure 6.4 shows the $\frac{\text{W+jets}}{\text{Z+jets}}$ ratio distributions for the same variables. The ratio cannot be directly unfolded, instead it is formed by taking the ratio of the unfolded W+jets and Z+jets distributions. Each figure presents the results achieved for unfolding with different numbers of Bayesian iterations (1-6), with comparison to particle-level results from ALPGEN Monte Carlo. For the distributions shown in Figures 6.3 and 6.4, the difference in the results obtained with different numbers of iterations is small.

6.2.3 Closure Tests

Two closure tests were used to assess the validity of the unfolding procedure, as performed by the RooUnfold framework. The first involved replacing the data distribution used as input to RooUnfold with the corresponding ALPGEN Monte Carlo distribution at reconstructed level, i.e. replacing R^{Data} with R^{MC}. All other unfolding inputs (response matrix, fake correction, ALPGEN particle-level and reconstructed-level distributions) were unchanged. The same ALPGEN sample was used both in place of R^{Data} and for the construction of the unfolding matrix. Therefore, it was expected that the resulting unfolded distribution will agree very well with the corresponding ALPGEN particle-level distribution, across all bins and for all variables. The second closure test acted as a check of the dependancy of the unfolded results on the chosen Monte Carlo physics model, by using the reconstructed-level distribution modelled by SHERPA in place of R^{Data}, instead of the distribution modelled by ALPGEN.

Both closure tests were performed for 1-6 Bayesian iterations, the results for the electron channel are shown in Figures 6.5, 6.6 and 6.7, for exclusive jet multiplicity, leading jet P_T and rapidity. Results are shown in the W+jets, Z+jets and $\frac{\text{W+jets}}{\text{Z+jets}}$ channels. As expected, for the ALPGEN closure test there is perfect agreement between the unfolded reconstructed-level ALPGEN distri-

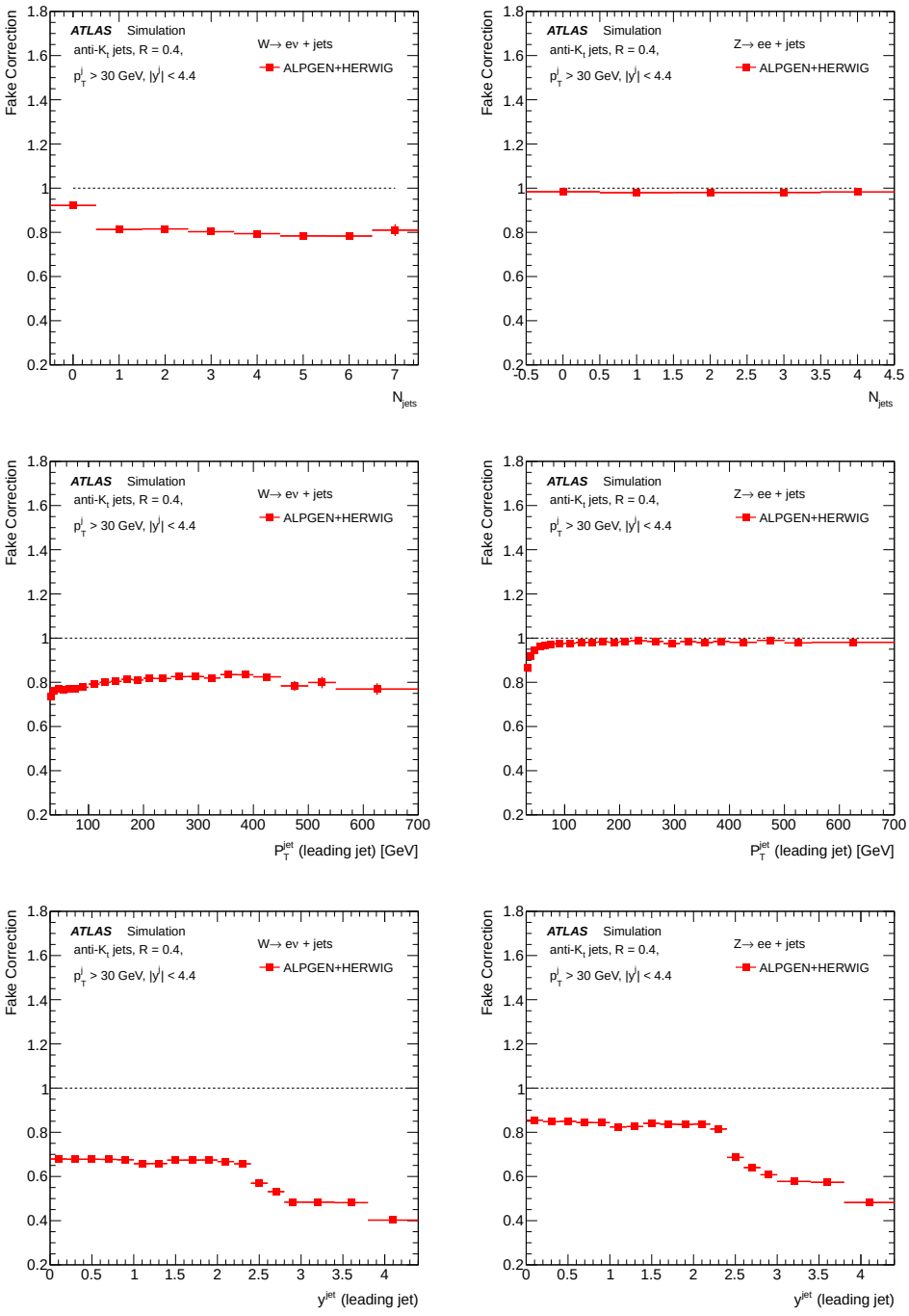

Figure 6.2: Electron channel bin-by-bin fake correction factors for exclusive jet multiplicity (top), leading jet P_T (middle) and leading jet rapidity (bottom). Left: W+jets channel; Right: Z+jets channel.

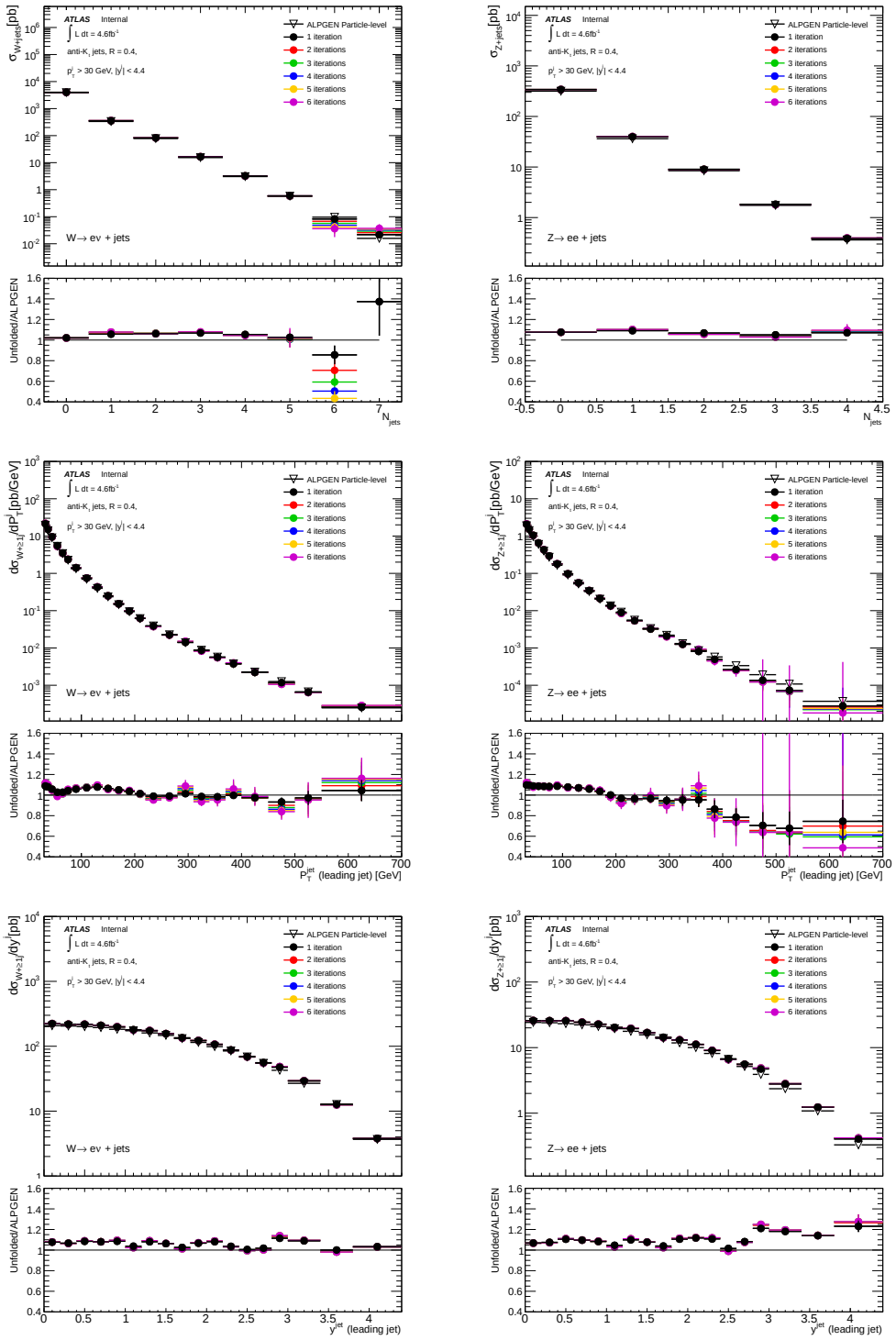

Figure 6.3: Electron channel unfolded data distributions for exclusive jet multiplicity (top), leading jet P_T (middle) and leading jet rapidity (bottom). Left: W+jets channel; Right: Z+jets channel. Results are shown for unfolding with 1-6 Bayesian iterations and are compared to the corresponding particle-level ALPGEN Monte Carlo distribution.

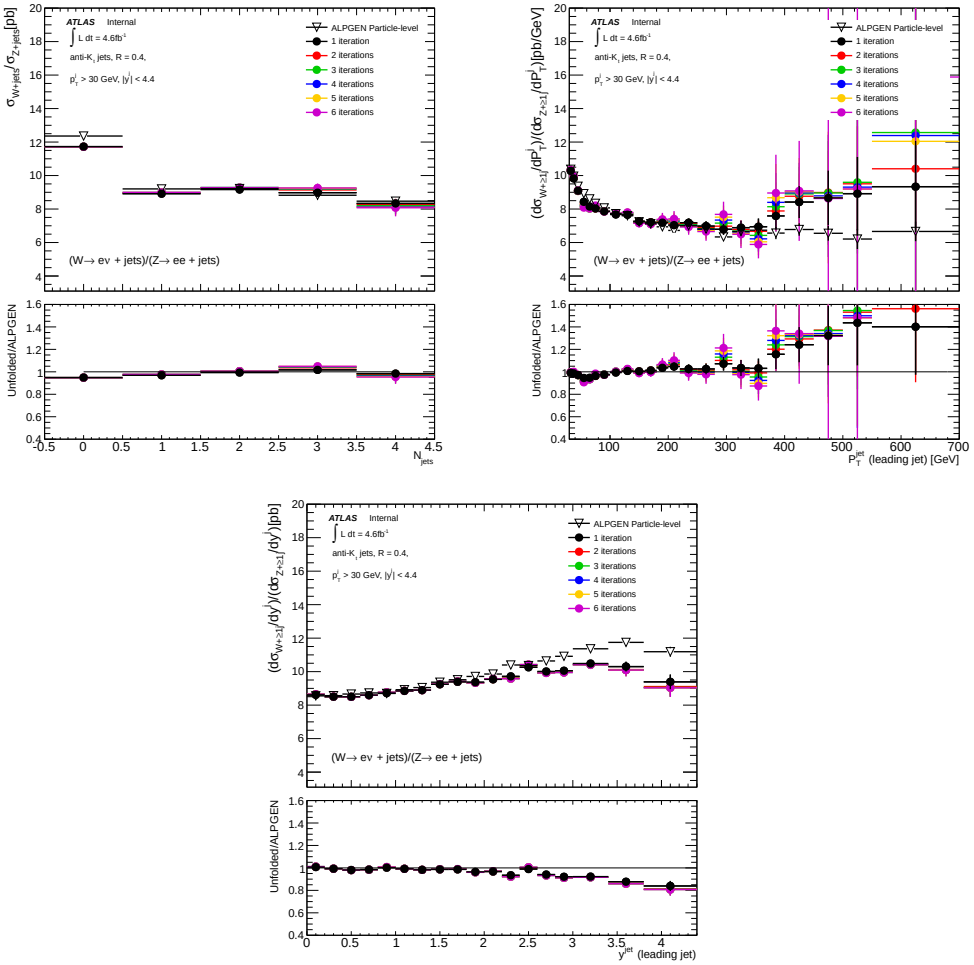

Figure 6.4: Electron channel unfolded data distributions for the ratio of $\frac{\text{W+jets}}{\text{Z+jets}}$. Shown are the distributions of exclusive jet multiplicity (top left), leading jet P_T (top right) and leading jet rapidity (bottom). Results are shown for unfolding with 1-6 Bayesian iterations and are compared to the corresponding particle-level ALPGEN Monte Carlo distribution.

butions and the corresponding ALPGEN particle-level distributions. For the closure test with SHERPA, very good closure is achieved for most of the distributions, with deviations occurring in the regions of low Monte Carlo statistics. The shape differences between ALPGEN and SHERPA are small, yet they are still an overestimation of the potential effect on unfolded data. The differences between data and ALPGEN at detector level are generally smaller than the shape differences between ALPGEN and SHERPA. This was one of the justifications for using ALPGEN samples for unfolding, and why the unfolding model uncertainty is evaluated with ALPGEN samples with shifted parameters (see Section 6.3.2).

The unfolded ratio measurement cannot be directly achieved by implementing Bayesian unfolding. It has to be formed by taking the ratio of the two statistically uncorrelated unfolded results for W and Z, thus rendering it more susceptible to the statistical fluctuations of the Monte Carlo samples and the data than either the W or Z measurements. One can see for the closure tests for the ratio measurements that the effect of such uncorrelated statistical fluctuations is negligible.

The results of the closure tests are largely similar for each number of Bayesian iterations, therefore the closure test could not be used to inform the decision on how many iterations to employ for the unfolding of data in this analysis. Instead, the number of iterations to use was decided upon after investigating how the systematic uncertainty related to the unfolding method (described in detail in Section 6.3) behaved for different numbers of iterations. We wished to find the number of iterations for which the uncertainty was minimum, this proved to be between one and three for most variables. Therefore, two was chosen as the nominal number of iterations used for the unfolding in this analysis.

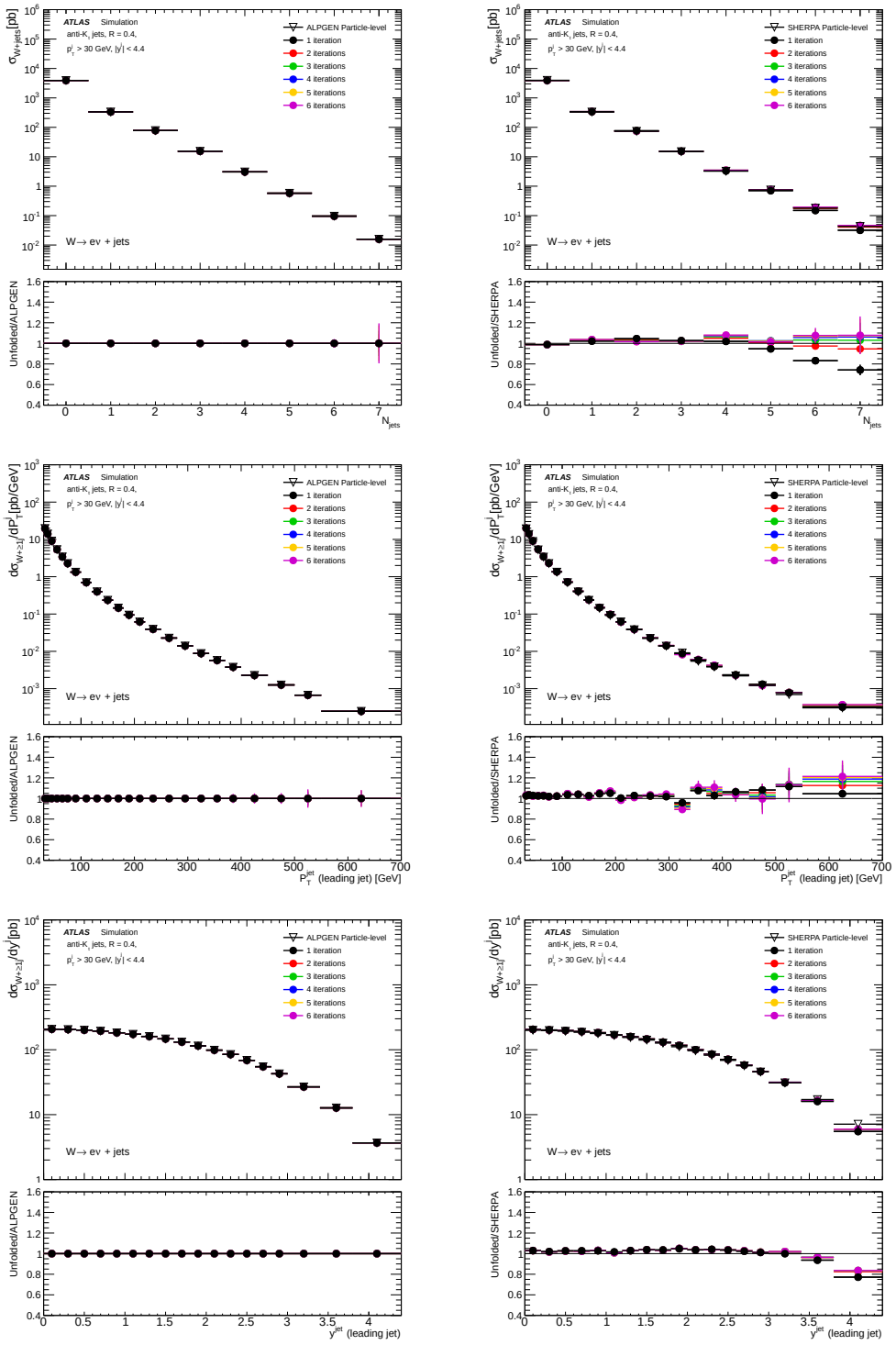

Figure 6.5: Electron channel closure tests for the W+jets channel. Shown are the exclusive jet multiplicity (top), leading jet P_T (middle) and leading jet rapidity (bottom) distributions. Left: ALPGEN closure test; Right: SHERPA closure test. In each case the result is compared to the corresponding particle-level distribution, from either ALPGEN or SHERPA.

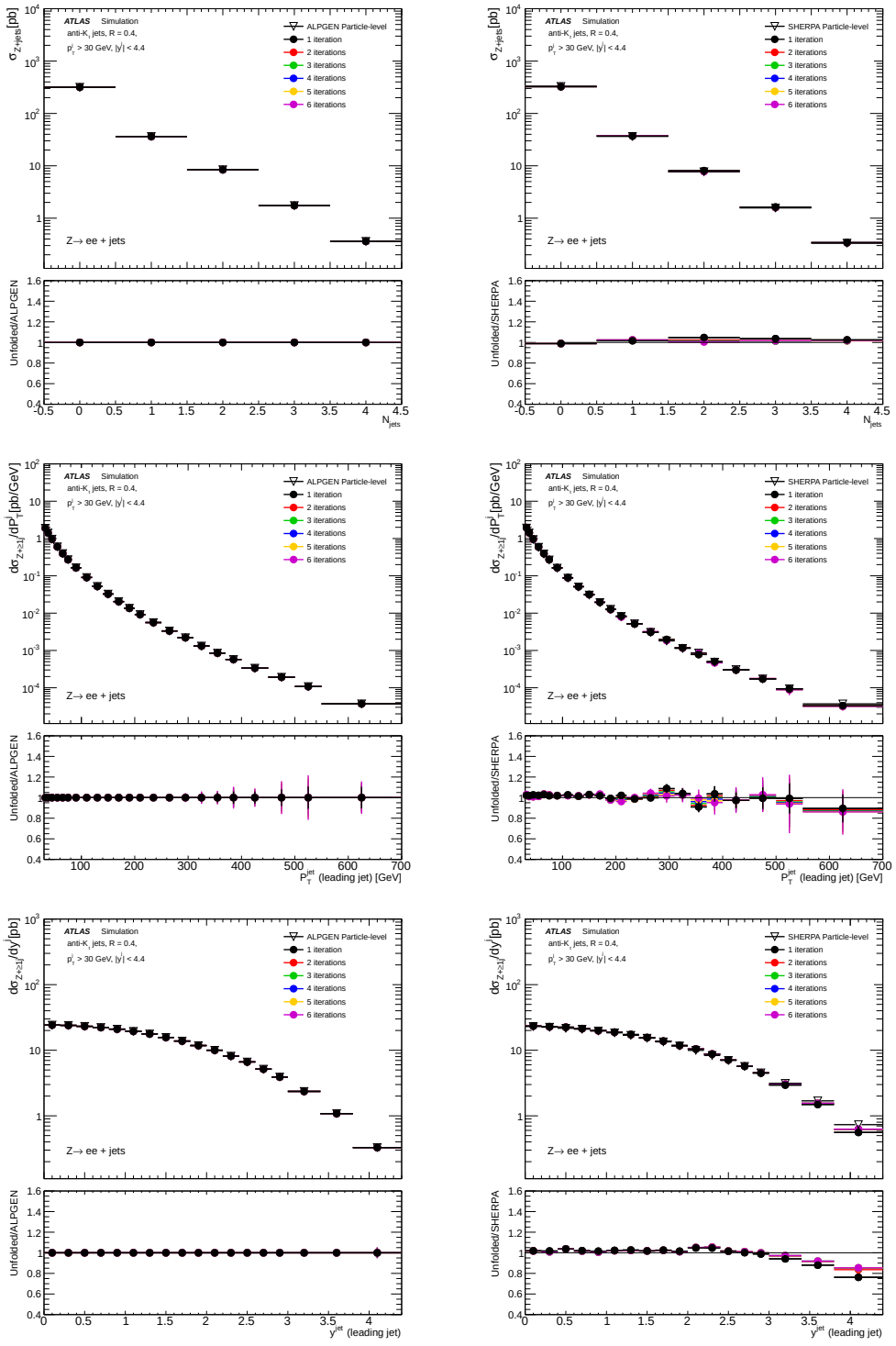

Figure 6.6: Electron channel closure tests for the Z+jets channel. Shown are the exclusive jet multiplicity (top), leading jet P_T (middle) and leading jet rapidity (bottom) distributions. Left: ALPGEN closure test; Right: SHERPA closure test. In each case the result is compared to the corresponding particle-level distribution, from either ALPGEN or SHERPA.

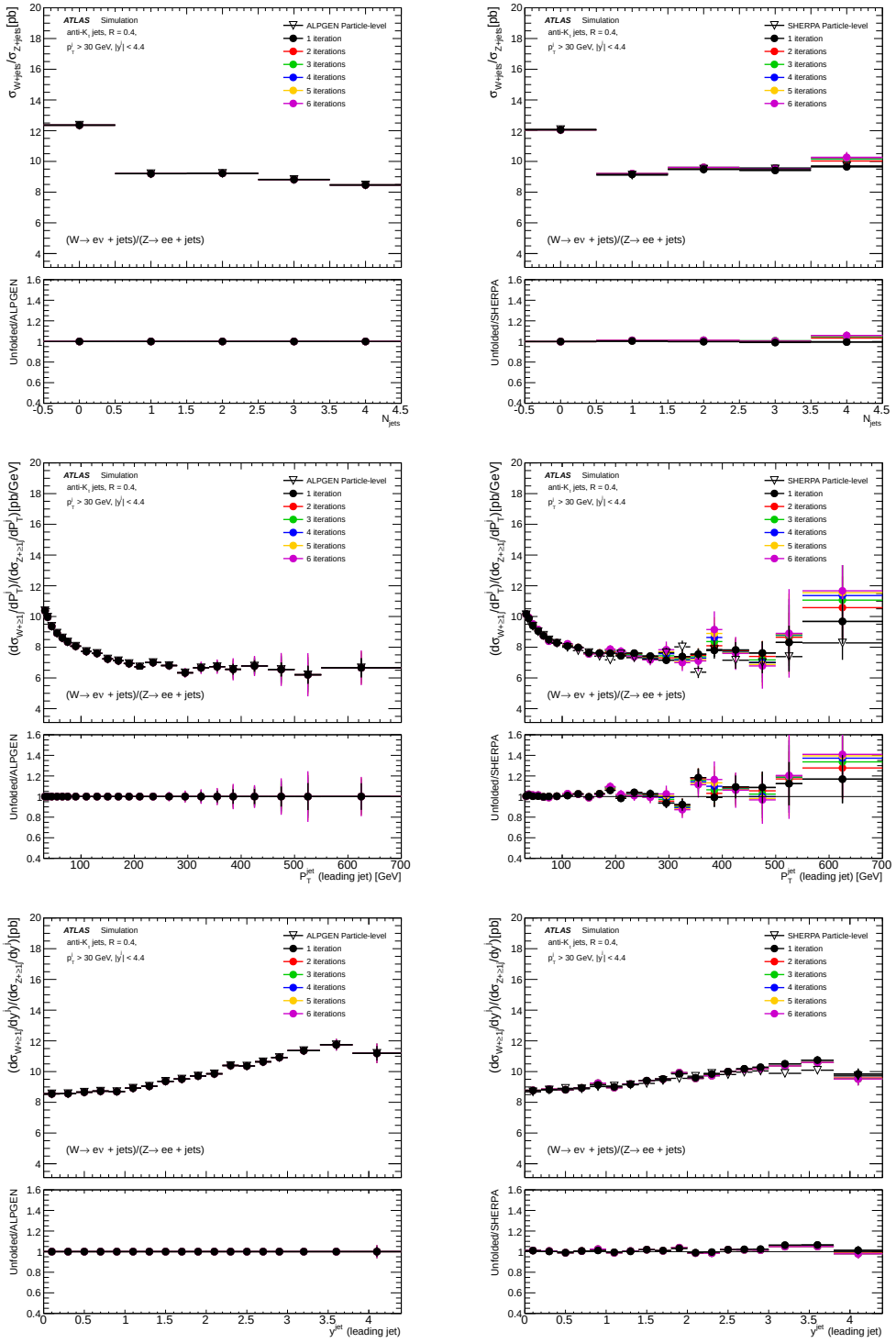

Figure 6.7: Electron channel closure tests for the $\frac{\text{W+jets}}{\text{Z+jets}}$ channel. Shown are the exclusive jet multiplicity (top), leading jet P_T (middle) and leading jet rapidity (bottom) distributions. Left: ALPGEN closure test; Right: SHERPA closure test. In each case the result is compared to the corresponding particle-level distribution, from either ALPGEN or SHERPA.

6.3 Systematic Uncertainties on the Unfolding Technique

The systematic uncertainties associated with the unfolding method described above can be broken down into two components; (i) those pertaining to the statistical fluctuations of the Monte Carlo sample used, (ii) those pertaining to the modelling of jet characteristics as implemented by the Monte Carlo sample chosen for unfolding. The methods of evaluating the two sources of systematic uncertainty are described below.

6.3.1 Statistical Unfolding Uncertainty

Toy Monte Carlo experiments were used to evaluate the unfolding uncertainty arising from limited statistics. Each of the unfolding inputs (Monte Carlo particle-level and reconstructed-level distributions, fake corrections and response matrices) were smeared according to a Gaussian distribution. The contents of each bin were varied according to a Gaussian distribution with a mean and sigma corresponding to the number and root mean square of the Monte Carlo events in that particular bin respectively. In order to avoid double smearing of events that are present at both reconstructed-level and particle-level, the distributions to be smeared were split into four discrete samples:

1. Particle-level events that had a corresponding event at reconstructed level.
2. Reconstructed-level events that had a corresponding event at particle level.
3. Particle-level events with no corresponding reconstructed-level event.
4. Reconstructed-level events with no corresponding particle-level event.

Each sample was smeared independently, after which the reconstructed-level and particle-level distributions were rebuilt. The particle-level distribution was built via a bin-by-bin sum of histograms from samples (1) and (3).

Likewise, the reconstructed-level distributions were built via a sum of histogram from samples (2) and (4). The data was then unfolded according to the method described above, but using the varied inputs. This was repeated 100 times and the root mean square of the average of the 100 results was taken as the unfolding statistics systematic uncertainty.

6.3.2 Model Unfolding Uncertainty

The unfolding uncertainty associated with the modelling of jet characteristics by ALPGEN was evaluated by separately unfolding the data with five different sets of ALPGEN samples, each with varied parameters. Specifically, the minimum parton P_T and the cone size of the MLM parton-jet matching[5] [82] were varied. The effect of changing the amount of radiation emitted by hard partons was also considered, by varying the QCD renormalisation/factorisation scales to twice and half the nominal values[6]. The data were unfolded with each of the varied ALPGEN samples in place of the nominal, and the offset from the nominal unfolded results was considered to be a source of systematic uncertainty. The five systematic uncertainties were then added in quadrature to form the total unfolding model uncertainty. Table 6.2 presents a breakdown of the electron channel unfolding statistical and modelling errors, in bins of exclusive and inclusive jet multiplicity. Figure 6.8 shows the unfolding uncertainties, and their quadratic sum, for exclusive and inclusive jet multiplicity, leading jet P_T and rapidity.

[5]The MLM matching procedure is employed in ALPGEN to remove any double counting between partons from the matrix element calculation and those from the parton shower.

[6]ALPGEN Monte Carlo simulations employ a nominal value for the renormalisation/factorisation scales of $\sqrt{M_V^2 + P_{T_V}^2}$, where V is the W or Z boson.

Systematic	N_{jet}=0	N_{jet}=1	N_{jet}=2	N_{jet}=3	N_{jet}=4	N_{jet}=5	N_{jet}=6	N_{jet}=7
				$W \to e\nu$				
Unf. Model	0.27	2.43	0.96	1.26	1.17	0.98	0.69	1.75
Unf. Stat.	0.07	0.07	0.15	0.36	0.61	1.06	3.67	11.04
Total	0.28	2.44	0.97	1.31	1.32	1.44	3.73	11.18
				$Z \to ee$				
Unf. Model	0.16	1.97	1.37	2.03	1.35	-	-	-
Unf. Stat.	0.07	0.23	0.28	0.66	1.12	-	-	-
Total	0.18	1.99	1.40	2.13	1.81	-	-	-
Systematic	Incl.	N_{jet} >1	N_{jet} >2	N_{jet} >3	N_{jet} >4	N_{jet}>5	N_{jet} >6	N_{jet} >7
				$W \to e\nu$				
Unf. Model	0.23	1.74	0.90	1.00	1.12	0.89	0.74	1.76
Unf. Stat.	0.07	0.11	0.21	0.45	0.80	1.70	5.70	11.05
Total	0.24	1.74	0.92	1.01	1.38	1.92	5.75	11.19
				$Z \to ee$				
Unf. Model	0.11	1.43	0.93	1.46	1.28	-	-	-
Unf. Stat.	0.10	0.27	0.41	0.89	1.77	-	-	-
Total	0.15	1.46	1.02	1.71	2.19	-	-	-

Table 6.2: Systematic uncertainties (quoted as total percentage error) on the unfolding method for the electron channel, in bins of exclusive and inclusive jet multiplicity.

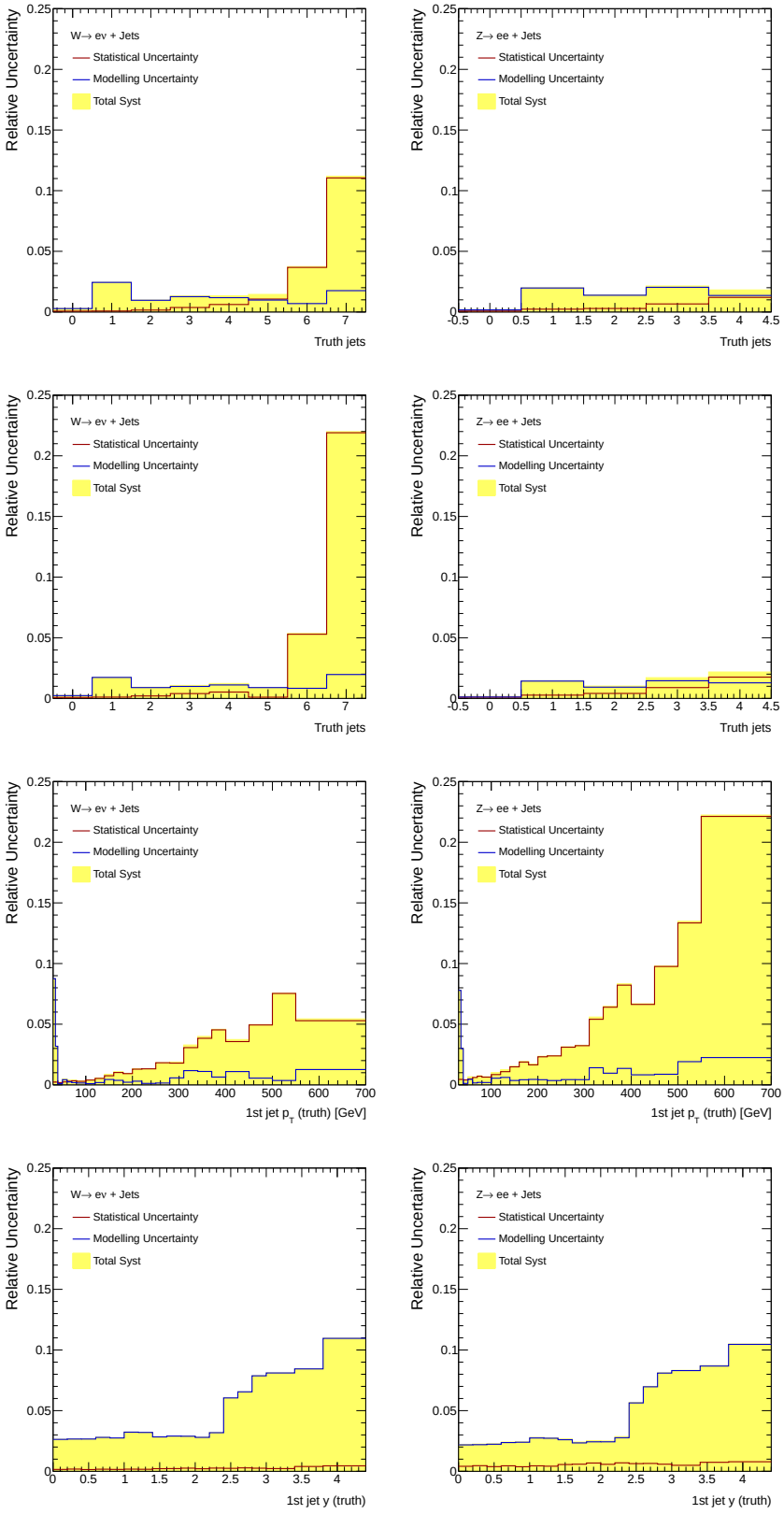

Figure 6.8: Electron channel uncertainties on the unfolding procedure arising from Monte Carlo modelling and statistics for exclusive jet multiplicity (top row), inclusive jet multiplicity (2nd row), leading jet P_T in events with at least one jet (3rd row) and leading jet rapidity in events with at least one jet (bottom row). Left: W+jets; Right: Z+jets

6.4 Systematic Uncertainties on the Unfolded Results

In addition to the systematic variations specifically related to the unfolding method, each of the systematic uncertainties mentioned in the preceding chapters was also propagated through the unfolding. Those variations, pertaining to the jet energy scale (JES), jet energy resolution (JER), lepton and E_T^{miss} uncertainties were propagated by shifting the reconstructed signal Monte Carlo distributions, the Monte Carlo backgrounds, the unfolding matrices and fake corrections. The data driven QCD and $t\bar{t}$ backgrounds were re-estimated using shifted Monte Carlo templates corresponding to the uncertainty to be evaluated, and those varied background estimates were used in the unfolding. For those systematic uncertainties relating to a specific background process (i.e. from Monte Carlo normalisation, or directly related to the data-driven technique), the variations were applied to the relevant background sample. This applied to both backgrounds estimated with Monte Carlo and those derived from data-driven techniques. All other inputs were unvaried in this case. The unfolding procedure was then performed for each systematic variation, taking each time the combination of nominal and varied inputs mentioned above. The components of each systematic uncertainty were propagated individually, e.g. the five up and five down electron energy scale uncertainties (see Section 4.4.4.1) were each treated separately. After unfolding each kinematic distribution, the individual systematic uncertainties were stored as variations from the nominal unfolded results. This way, the systematic sources could be treated individually in the combination technique (see Chapter 8).

Finally, the value for luminosity by which the Monte Carlo samples were scaled to data was deemed to have an associated error of 1.8% [83]. This error was propagated through the unfolding by scaling all inputs from Monte Carlo up and down by the luminosity $\pm 1.8\%$ and once again unfolding the data distributions.

Tables 6.3 and 6.4 present the systematic uncertainties on the unfolded inclusive jet multiplicity measurements for the electron and muon channels. Shown are the uncertainties on the W+jets and Z+jets channels, and the $\frac{\text{W+jets}}{\text{Z+jets}}$ ratio. Here the sources of uncertainty have been grouped and summed in quadrature for the purpose of providing an overview. Uncertainties on JES and jet energy resolution (JER) are the largest source of uncertainty in the separate lepton channels, but are highly correlated between the W+jets and Z+jets channels. Therefore, they are largely cancelled for the ratio measurement. Despite large cancellation, for low jet multiplicities, JES and JER are still the dominant source of uncertainty on the ratio measurement. This is because variations due to JES and JER were propagated to the measurement of E_T^{miss} in each event, yielding larger overall variations in the W+jets channel. The size of background processes is also larger for W+jets than Z+jets (see Tables 4.5 and 4.6), resulting in a larger overall jet uncertainty in the W+jets channel.

A final observation is that in the individual lepton channels, the JES and JER uncertainties on the ratio measurement are slightly larger in the electron channel than in the muon channel. At low jet multiplicities, this is mainly due to the $Z \to ee$ background in the $W \to e\nu$ selection being larger than the corresponding $Z \to \mu\mu$ background in the $W \to \mu\nu$ selection. This is because one electron from $Z \to ee$ events can be mis-identified as a jet, thus contributing to the total JES and JER uncertainties. At higher jet multiplicities (up to around 5 jets), the JES and JER uncertainties are larger in the electron channel due to fluctuations of the $t\bar{t}$ fit, described in Section 5.2.3.

6.5 Electron Channel Results Unfolded to Particle Level

The distributions shown in this section are electron channel data unfolded to particle level, via the method described in Section 6.2. The error band is

Systematic	Incl.	$N_{jet}>1$	$N_{jet}>2$	$N_{jet}>3$	$N_{jet}>4$	$N_{jet}>5$	$N_{jet}>6$	$N_{jet}>7$
$W \to e\nu$ + jets								
JES	0.09	7.37	9.51	12.83	17.40	24.01	35.44	21.98
JER	0.22	5.21	5.83	7.33	9.60	15.63	21.82	39.54
Jets	0.25	9.03	11.16	14.78	19.87	28.65	41.62	45.24
Elec.	1.13	1.31	1.32	1.23	1.21	1.34	2.67	3.48
E_T^{miss}	0.19	1.68	1.23	1.17	0.98	0.67	1.68	2.64
Bkgs.	0.48	1.59	1.87	5.24	14.49	42.09	105.22	88.22
Lumi.	1.87	2.08	2.12	2.21	2.32	2.45	2.57	2.18
Unf.	0.24	1.74	0.92	1.01	1.38	1.92	5.75	11.19
Total	2.27	9.79	11.69	15.97	24.79	51.00	113.35	101.67
$Z \to ee$+ jets								
JES	0.01	5.45	7.78	10.09	13.20	-	-	-
JER	0.02	2.93	2.52	3.30	3.80	-	-	-
Jets	0.02	6.19	08.18	10.61	13.74	-	-	-
Elec.	1.58	1.78	1.77	1.77	1.76	-	-	-
E_T^{miss}	0.00	0.00	0.00	0.00	0.00	-	-	-
Bkgs.	0.67	0.69	0.87	1.08	1.40	-	-	-
Lumi.	1.81	1.83	1.88	1.95	2.01	-	-	-
Unf.	0.15	1.46	1.02	1.71	2.19	-	-	-
Total	0.18	1.99	1.40	2.13	1.81	-	-	-
$(W \to e\nu$ + jets$)/(Z \to ee$+ jets$)$								
JES	0.09	2.01	1.97	3.52	5.22	-	-	-
JER	0.25	2.35	3.40	4.17	6.03	-	-	-
Jets	0.27	3.09	3.93	5.46	7.98	-	-	-
Elec.	0.89	0.93	0.93	0.97	1.04	-	-	-
E_T^{miss}	0.19	1.68	1.23	1.17	0.98	-	-	-
Bkgs.	0.82	1.69	1.93	5.30	14.69	-	-	-
Lumi.	0.06	0.25	0.24	0.27	0.31	-	-	-
Unf.	0.20	0.56	0.86	1.21	1.40	-	-	-
Total	1.27	4.06	4.73	7.85	16.84	-	-	-

Table 6.3: Systematic uncertainties (quoted as total percentage error) on the unfolded results for the electron channel, in bins of inclusive jet multiplicity.

Systematic	Incl.	$N_{jet}>1$	$N_{jet}>2$	$N_{jet}>3$	$N_{jet}>4$	$N_{jet}>5$	$N_{jet}>6$	$N_{jet}>7$
$W \to \mu\nu$ + jets								
JES	0.11	6.32	8.26	11.07	13.89	15.72	21.31	53.33
JER	0.07	4.42	4.24	5.76	7.54	12.54	19.32	20.88
Jets	0.13	7.71	9.29	12.48	15.81	20.11	28.77	57.27
Muon	1.51	1.64	1.63	1.38	1.43	2.05	3.62	4.36
E_T^{miss}	0.30	1.01	0.93	0.95	0.95	0.63	0.89	1.10
Bkgs.	0.23	0.59	1.21	4.26	10.94	26.23	46.26	56.60
Lumi.	1.87	2.10	2.16	2.20	2.34	2.49	2.62	2.24
Unf.	0.24	1.73	0.91	1.03	1.19	1.30	2.56	10.80
Total	2.47	8.39	9.80	13.48	19.45	33.21	54.70	81.39
$Z \to \mu\mu$ + jets								
JES	0.02	5.55	7.81	10.31	13.63	-	-	-
JER	0.02	2.91	2.56	3.36	3.78	-	-	-
Jets	0.03	6.26	8.22	10.84	14.14	-	-	-
Muon	0.52	0.62	0.67	0.75	0.84	-	-	-
E_T^{miss}	0.00	0.00	0.00	0.00	0.00	-	-	-
Bkgs.	0.18	0.34	0.85	1.62	3.22	-	-	-
Lumi.	1.81	1.84	1.90	2.00	2.13	-	-	-
Unf.	0.12	1.43	0.95	1.51	1.71	-	-	-
Total	1.89	6.72	8.56	11.27	14.78	-	-	-
$(W \to \mu\nu$ + jets$)/(Z \to \mu\mu$ + jets$)$								
JES	0.10	0.83	0.66	1.60	2.38	-	-	-
JER	0.09	1.55	1.73	2.48	3.91	-	-	-
Jets	0.14	1.76	1.85	2.95	4.57	-	-	-
Muon	1.13	1.18	1.12	0.82	0.81	-	-	-
E_T^{miss}	0.30	1.01	0.93	0.95	0.95	-	-	-
Bkgs.	0.29	0.67	1.44	4.58	11.43	-	-	-
Lumi.	0.10	0.11	0.09	0.03	0.07	-	-	-
Unf.	0.23	0.58	0.89	1.23	1.24	-	-	-
Total	1.24	2.51	2.90	5.73	12.44	-	-	-

Table 6.4: Systematic uncertainties (quoted as total percentage error) on the unfolded results for the muon channel, in bins of inclusive jet multiplicity.

the total systematic uncertainty, including all contributions discussed in the previous sections. The data is compared with theoretical predictions from BLACKHAT+SHERPA, ALPGEN and SHERPA. The theoretical predictions will be discussed in more detail in the following chapter. Figure 6.9 shows the unfolded measurements for exclusive and inclusive jet multiplicity. Figure 6.10 shows the measurement for leading and second-leading jet P_T in events with at least one and two jets respectively. Finally, Figure 6.11 shows the unfolded measurements for the scalar sum of all jet P_T in events with at least two jets, and leading jet rapidity for events with at least one jet. All results are shown for both W+jets and Z+jets channels. The corresponding muon channel results were unfolded using the same method described above. To form the final ratio measurement for each kinematic variable, the results from the two lepton channels were combined. Chapter 8 presents a discussion of the combination technique and the final unfolded ratio results.

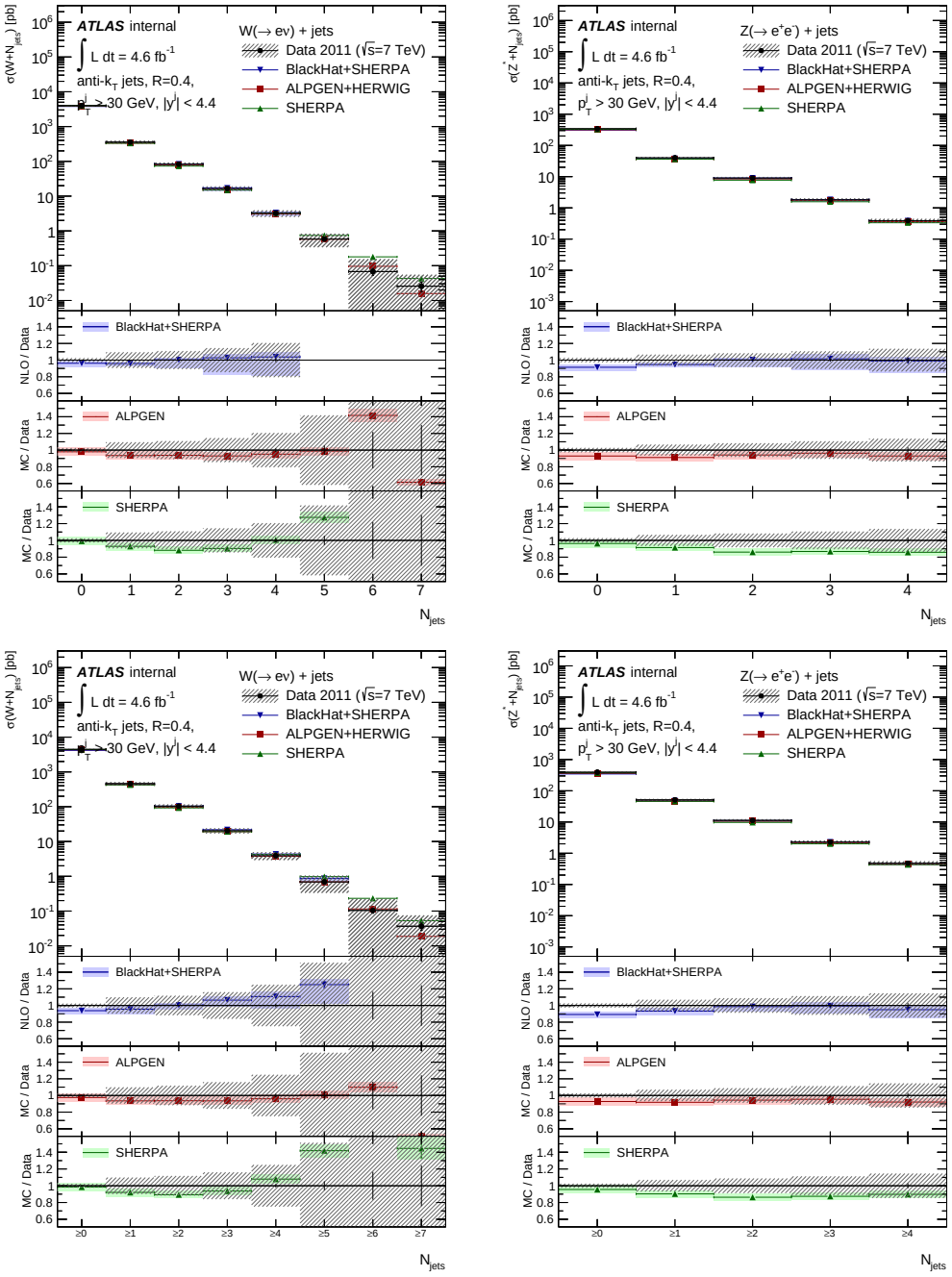

Figure 6.9: Electron channel unfolded data distribution and theoretical predictions for exclusive jet multiplicity (top) and inclusive jet multiplicity (bottom). Left: W+jets channel; Right: Z+jets channel.

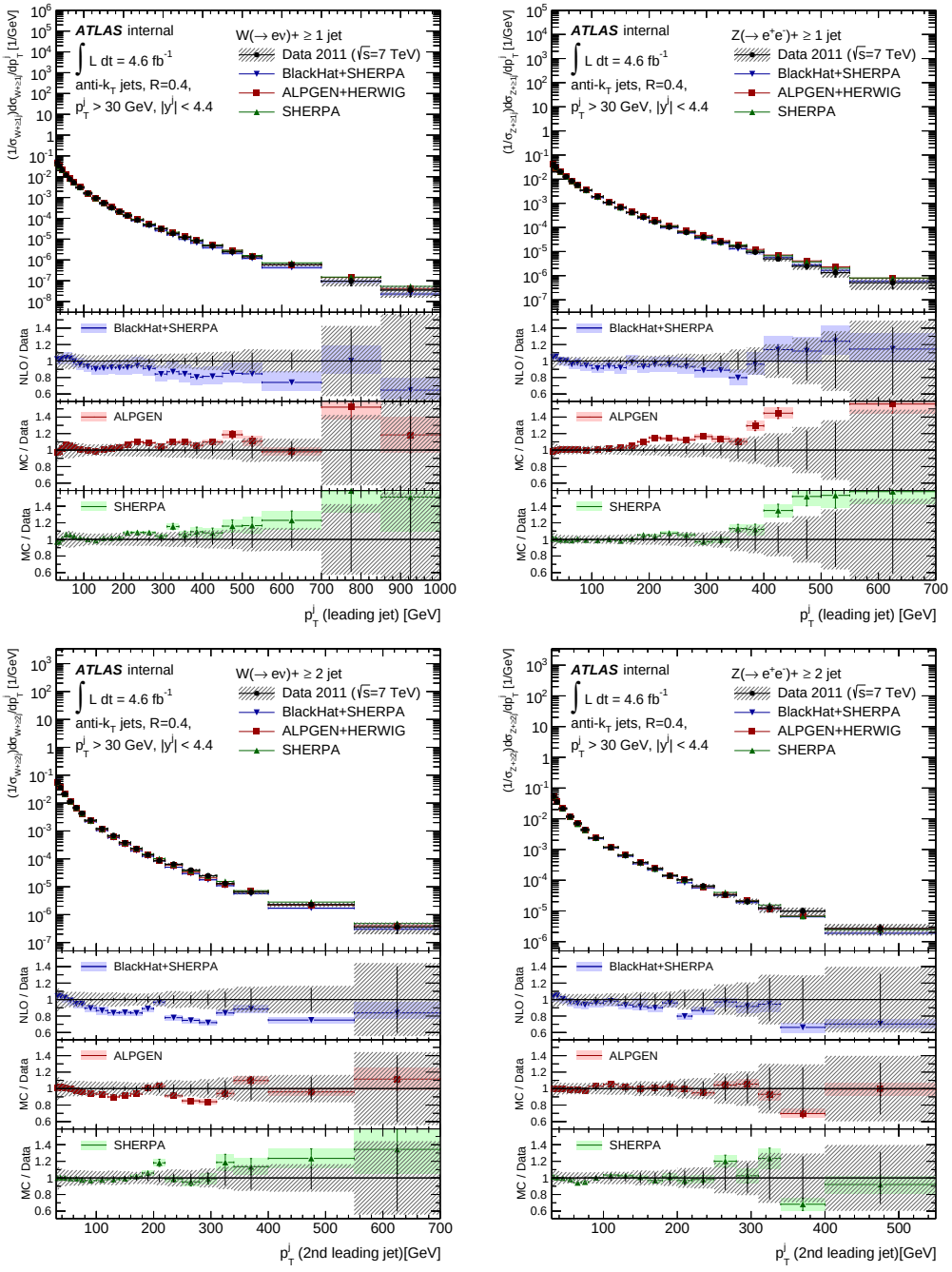

Figure 6.10: Electron channel unfolded data distribution and theoretical predictions for leading jet P_T in events with at least one jet (top) and second leading jet P_T in events with at least two jets (bottom). Left: W+jets channel; Right: Z+jets channel.

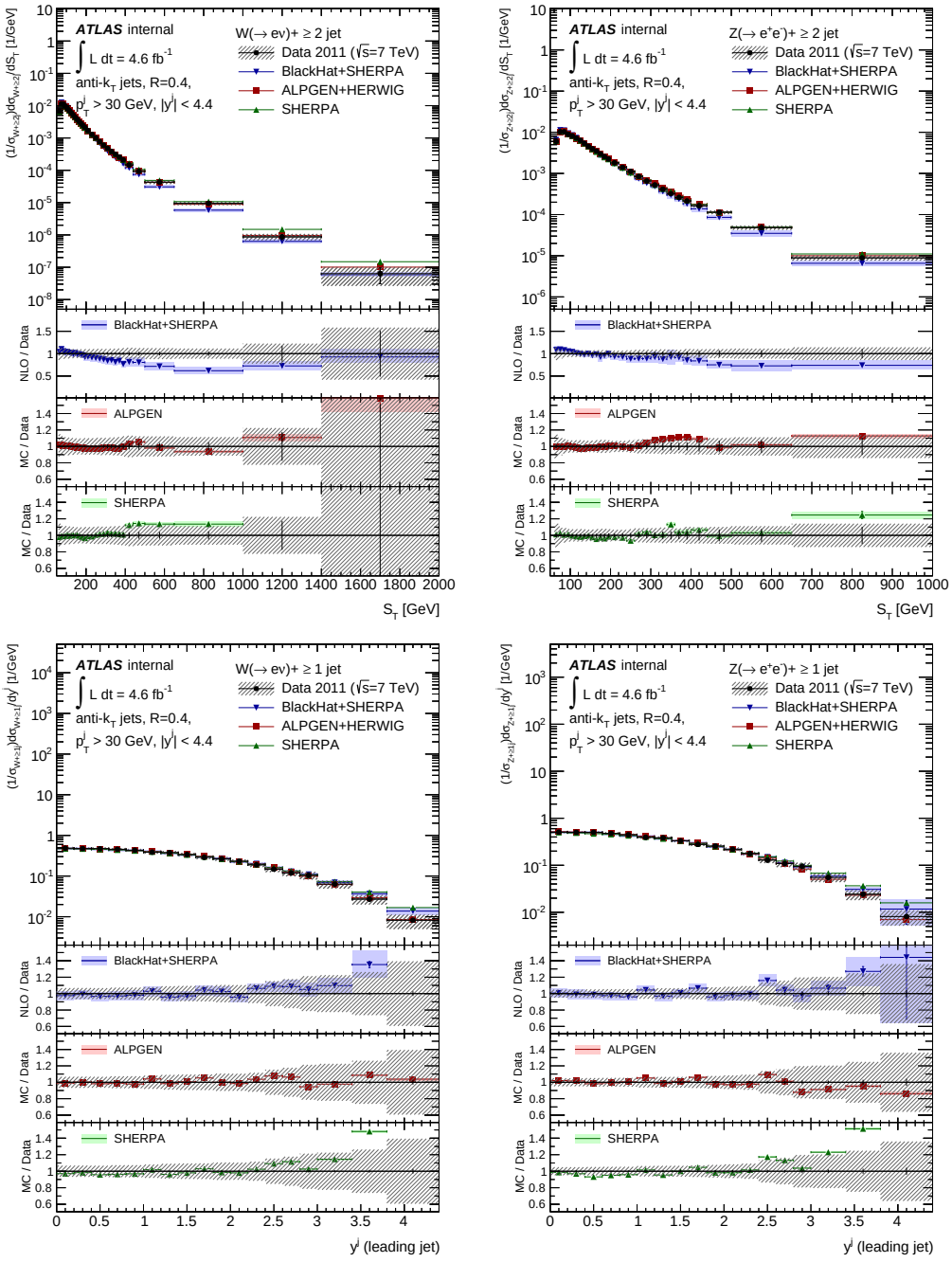

Figure 6.11: Electron channel unfolded data distribution and theoretical predictions for the scalar sum of all jet P_T (a variable referred to as S_T) in events with at least 2 jets (top) and leading jet rapidity in events with at least one jet (bottom). Left: W+jets channel; Right: Z+jets channel.

Chapter 7

Theoretical Predictions

The data which has been unfolded to particle level is presented with comparisons to theoretical predictions in Chapter 8. Two separate multiple-parton leading-order predictions, matched to leading-log parton shower approximations, are obtained from ALPGEN and SHERPA. Additionally, comparisons are made to next-to-leading order perturbative QCD predictions for parton multiplicities zero to four, provided by BLACKHAT+SHERPA (BH+S) [26, 27, 28].

This chapter presents a study on leading-order theoretical predictions to demonstrate the sensitivity of the ratio measurement to differences in QCD radiation modelling. Also discussed in this chapter are the sources of systematic uncertainty associated with next-to-leading order predictions provided by BH+S, and the corrections to BH+S required before accurate comparison with data can be made.

7.1 Sensitivity Study with Leading-Order Predictions

As mentioned above, the leading-order theoretical predictions provided by ALPGEN and SHERPA employ different methods of modelling the parton

shower and different matching procedures. The former is interfaced with HERWIG to model the parton shower and hadronisation, and uses the MLM matching procedure (performing a geometric measure of jet cones to analyse unconstrained radiation) [22]. SHERPA contains its own parton shower and uses the CKKW matching procedure which is based on parton showers which have been truncated [24, 84]. The matrix element calculations are the same for ALPGEN and SHERPA. With this knowledge, a study to compare the ratio as predicted by ALPGEN+HERWIG and SHERPA was performed. The aim of the study was to evaluate the sensitivity of the $\frac{\text{W+jets}}{\text{Z+jets}}$ ratio predictions to perturbative QCD predictions of radiation effects. Since the ratio is insensitive to non-perturbative effects and has a negligible sensitivity to choice of PDFs[1], the differences in their ratio predictions can be explained by the aforementioned differences in parton shower modelling and matching scheme, and thus their respective modelling of QCD radiation effects.

Figures 7.1 and 7.2 show the results of this study for leading jet P_T and S_T distributions respectively, where S_T is the scalar P_T sum of all jets in the event. The variables considered in this study are a subset of those this analysis measured. They were chosen because they are kinematic variables for which there are significant differences in the behaviour of W+jets and Z+jets events. The figures show a clear impact of the differences in radiation modelling on the ratio measurement. The shape of the ratio indicates differences in radiation between W+jets and Z+jets events. A flat ratio, as a function of P_T, would suggest that W+jets and Z+jets radiate energy at the same rate. For the ratios in Figures 7.1 and 7.2, SHERPA falls less steeply and is generally flatter than ALPGEN+HERWIG. This suggests SHERPA models a smaller difference than ALPGEN+HERWIG in radiated energy between W+jets and Z+jets events. The difference between the two predictions is as large as 8% in the lower P_T

[1] A full cancellation of PDF effects is prevented primarily because of mass differences between the W and Z and a residual b quark contribution from Z+jets events. However, the cancellation is good to the level of a few percent.

region, where differences between W+jets and Z+jets are expected.

The comparison of ratio predictions was performed in both electron and muon channels, and both channels exhibit very similar differences between ALPGEN+HERWIG and SHERPA. This is particularly evident in Figure 7.3 which shows the ratio comparison as a function of leading jet rapidity. For this distribution, large deviations between the two predictions are observed at high values of rapidity, and the same trend is seen in both lepton channels. As previously mentioned, ALPGEN is interfaced with PHOTOS to provide modelling of final state QED radiation, whereas SHERPA employs its own QED radiation model. From this, and the similarity of the ratio prediction comparisons across both lepton channels, we can conclude that QCD radiation effects are independent of QED final state radiation. The decoupling of QED and QCD radiation across the kinematic observables in this analysis, and the shape differences of the ratio for different QCD radiation models, demonstrate the sensitivity of the $\frac{\mathrm{W+jets}}{\mathrm{Z+jets}}$ measurement to QCD radiation from perturbative QCD models. Comparisons of the predicted ratio with data unfolded to particle level can therefore illuminate the successes and failures of the QCD modelling of theoretical predictions. This will be further discussed in Chapter 8.

7.2 Next-to-Leading Order Predictions

Next-to-leading order predictions are provided by BH+S, which uses CT10 PDFs [25]. The renormalisation and factorisation scales for these predictions is $H_T/2$, where H_T is the per-event scalar sum of the P_T of all particles and partons in the final state. BH+S reconstructs jets at particle level, using the anti-$k_\perp$ algorithm with a cone size of 0.4.

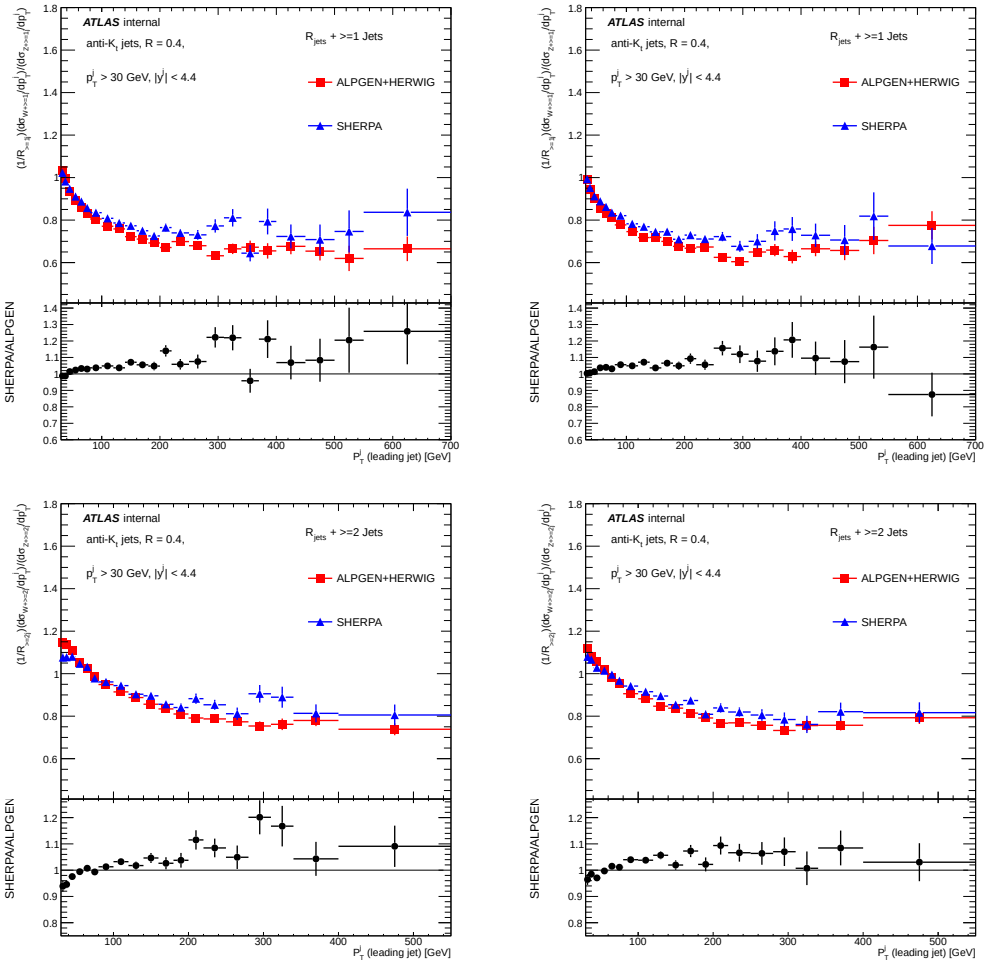

Figure 7.1: Comparison between ALPGEN+HERWIG and SHERPA theoretical predictions for the ratio of $\frac{\text{W+jets}}{\text{Z+jets}}$ events as a function of leading jet P_T. Top: Events with at least one jet; Bottom: Events with at least two jets. Left: Electron channel; Right: Muon channel.

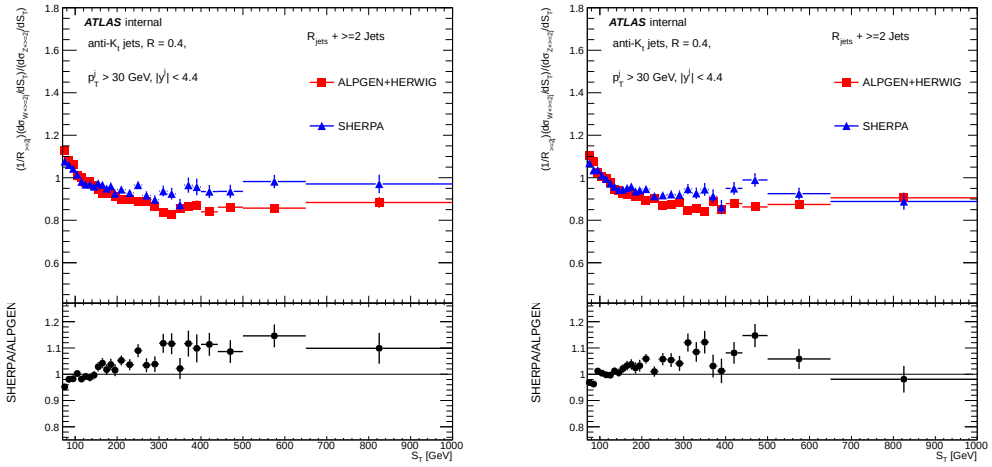

Figure 7.2: Comparison between ALPGEN+HERWIG and SHERPA theoretical predictions for the ratio of $\frac{\text{W+jets}}{\text{Z+jets}}$ events as a function of S_T, measured for events with at least 2 jets. Left: Electron channel; Right: Muon channel.

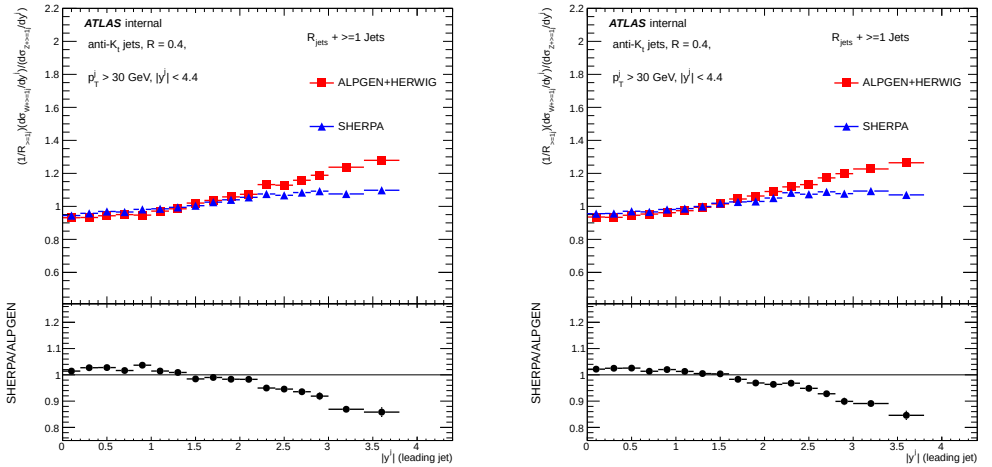

Figure 7.3: Comparison between ALPGEN+HERWIG and SHERPA theoretical predictions for the ratio of $\frac{\text{W+jets}}{\text{Z+jets}}$ events as a function of leading jet rapidity, measured for events with at least one jet. Left: Electron channel; Right: Muon channel.

7.2.1 Uncertainties on BH+S Predictions

Sources of systematic uncertainty on the BH+S predictions are threefold; uncertainties on the renomalisation and factorisation scales, PDF uncertainties, and the uncertainty on the value of α_s propagated through the evolution of the PDFs. The individual uncertainties on the W+jets and Z+jets channels were provided by the BH+S collaboration, the way in which they were evaluated is described below.

The renormalisation and factorisation scale uncertainty was evaluated by varying the energy scale up and down to twice and half the nominal value, i.e. H_T and $H_T/4$ respectively. The scale uncertainties are completely correlated between W and Z channels, therefore for each variation the uncertainty on the ratio was computed by simply taking the ratio of the varied W and Z distributions and taking the deviation from the nominal ratio.

The PDF uncertainties were evaluated from the 52 CT10 eigenvectors provided by the PDF fitters. An envelope of the maximum and minimum values for the ratio, achieved by varying each eigenvector independently, was taken as the uncertainty.

The value of α_s used in for the next-to-leading order calculations is 0.118. The uncertainty on the predictions arising from the uncertainty on α_s was evaluated by varying the value used in the calculation up and down by 0.0012. This uncertainty is a conservative estimate. However, the α_s uncertainty on the final predictions is small compared to the dominant renormalisation scale uncertainty. The α_s uncertainty was also considered in the evolution of the PDF uncertainty. As with the scale uncertainties, the uncertainty on α_s is completely correlated between W and Z channels, therefore the ratio uncertainty is evaluated in the same way, i.e. vary the W and Z distributions separately, form the ratio of the varied distributions, then take the uncertainty as the deviation of the varied ratio from the nominal ratio.

Each of the above systematics were added in quadrature to form the total

systematic uncertainty on the BH+S predictions. In the individual W+jets and Z+jets channels the dominant uncertainty is that related to the renormalisation scale. However, this uncertainty and the others mentioned are largely reduced for the ratio prediction. For example, in both W+jets and Z+jets channels the scale uncertainties on inclusive jet multiplicity are between 0.7-11.4%, as jet multiplicity increases from 1-4. This uncertainty on the ratio is between 0.7-2.3% in the same region. Breakdown plots for the uncertainties on the BH+S predictions are shown in [77].

7.2.2 Corrections to BH+S Predictions

In order to make appropriate comparisons between measured data and the BH+S predictions, a number of corrections must be first applied to the predictions. They are detailed below.

7.2.2.1 Non-Perturbative Corrections

The BH+S predictions are provided at parton level whereas the data is unfolded to particle level. Therefore, the non-perturbative contributions associated with hadronisation and the underlying event (UE), involved in moving from partons to hadrons, must be taken into account. The nominal ALPGEN+HERWIG+JIMMY Monte Carlo samples employed for the unfolding technique (described in Chapter 6) were used to evaluate two separate sets of bin-by-bin corrections for hadronisation and UE. The former correction was defined as the ratio of the distributions obtained from the above mentioned Monte Carlo when hadronic jets were selected, to those obtained by selecting parton jets. The BH+S predictions were formed using the lepton four-momentum before photon radiation, i.e. at the W or Z vertex. Such leptons are referred to as being at Born level. The distributions used in the numerator and denominator were selected using Born-level leptons, i.e:

$$\sigma^{had} = \frac{\text{hadron jets, Born leptons}}{\text{parton jets, Born leptons}} \tag{7.1}$$

The UE correction was formed by using separate ALPGEN+JIMMY+HERWIG samples generated without the underlying event. Another ratio was defined, of the distributions formed with parton jets and Born-level leptons with and without the underlying event, i.e.:

$$\sigma^{UE} = \frac{\text{parton jets, UE on, Born leptons}}{\text{parton jets, UE off, Born leptons}} \tag{7.2}$$

A systematic uncertainty on the above corrections was calculated by forming a separate set of corrections with ALPGEN+PYTHIA samples with the Perugia2011C tune [85]. The ALPGEN+PYTHIA samples utilise different hadronisation models and UE tunes, and the systematic uncertainty was evaluated as the difference between the total correction, $\sigma^{had} \times \sigma^{UE}$, as formed with the nominal samples and those generated with ALPGEN+PYTHIA. These corrections are shown in [77].

7.2.2.2 Corrections for QED Final State Radiation

The measured data distributions were formed from a selection which uses the lepton four-momentum in the final state. This includes the radiation of photons within a cone of radius 0.1 around the "bare" lepton. Such leptons are referred to as "dressed". For comparison with data, BH+S had to be corrected for QED final state radiation. Bin-by-bin corrections were once again calculated using the nominal ALPGEN+HERWIG+JIMMY samples. The corrections were applied as multiplicative factors, i.e. the closer a correction factor was to one, the smaller the correction. They were defined as the ratio of the parton level distributions obtained using a selection with dressed leptons, to those selected with Born leptons, i.e:

$$\sigma^{fsr} = \frac{\text{dressed leptons}}{\text{Born leptons}} \tag{7.3}$$

The systematic uncertainty on the QED final state radiation corrections was calculated by comparing the corrections obtained with the nominal Monte Carlo to those produced with SHERPA 1.4 samples. The latter employs its own model for photon radiation which is based on the YFS method [86]. The systematic uncertainty was once again taken as the difference between the two sets of corrections and symmeterised around the nominal corrections.

Separate corrections were derived for each kinematic distribution measured in this analysis. Figures 7.4 and 7.5 present two example distributions of the QED final state radiation corrections, shown are the corrections for exclusive jet multiplicity, leading jet P_T and rapidity, and the S_T for events with at least two jets. The corrections are mostly flat for these variables.

7.2.2.3 Acceptance Corrections

A final set of corrections were applied to the BH+S predictions to correct for the phase space selection employed. In the individual lepton channels, the measured data was from a selection in the fiducial phase space of that channel (as described in Chapter 4). The BH+S predictions were provided in the common phase space, defined in Table 8.1, in which the lepton has $|\eta|< 2.5$. Therefore, for data comparisons with BH+S in the individual channels, a bin-by-bin acceptance correction must be applied. The acceptance corrections for each distribution were calculated using the nominal ALPGEN+HERWIG+JIMMY samples and was defined as the ratio of the distribution obtained from a selection in the fiducial phase space to a selection in the common phases space, i.e:

$$\sigma^{fsr} = \frac{\text{Fiducial lepton phase space}}{\text{Common phase space}} \tag{7.4}$$

When the lepton channels were combined, the inverse of the quantity was applied to the measured data distributions to move them into a common phase space. As for the QED corrections, the acceptance corrections were applied as

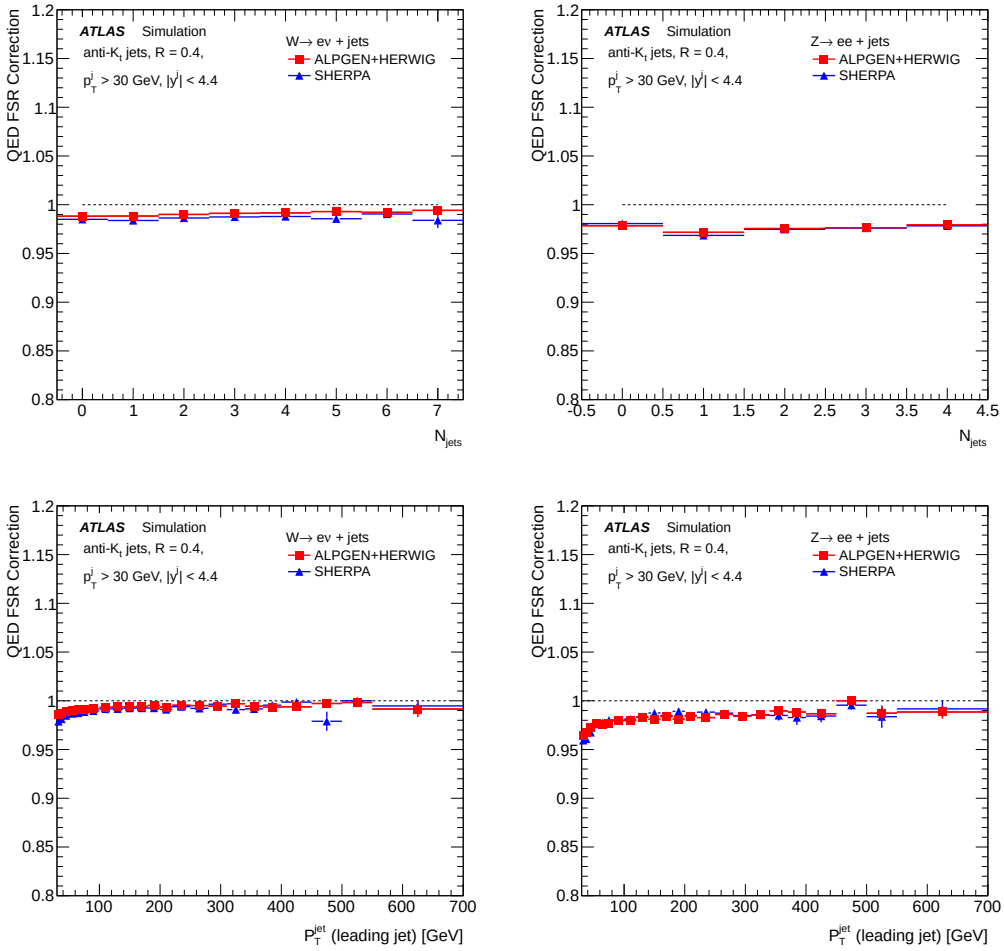

Figure 7.4: Electron channel QED final state radiation corrections for exclusive jet multiplicity (top) and leading jet P_T for events with at least one jet (bottom). Left: W+jets channel; Right: Z+jets channel

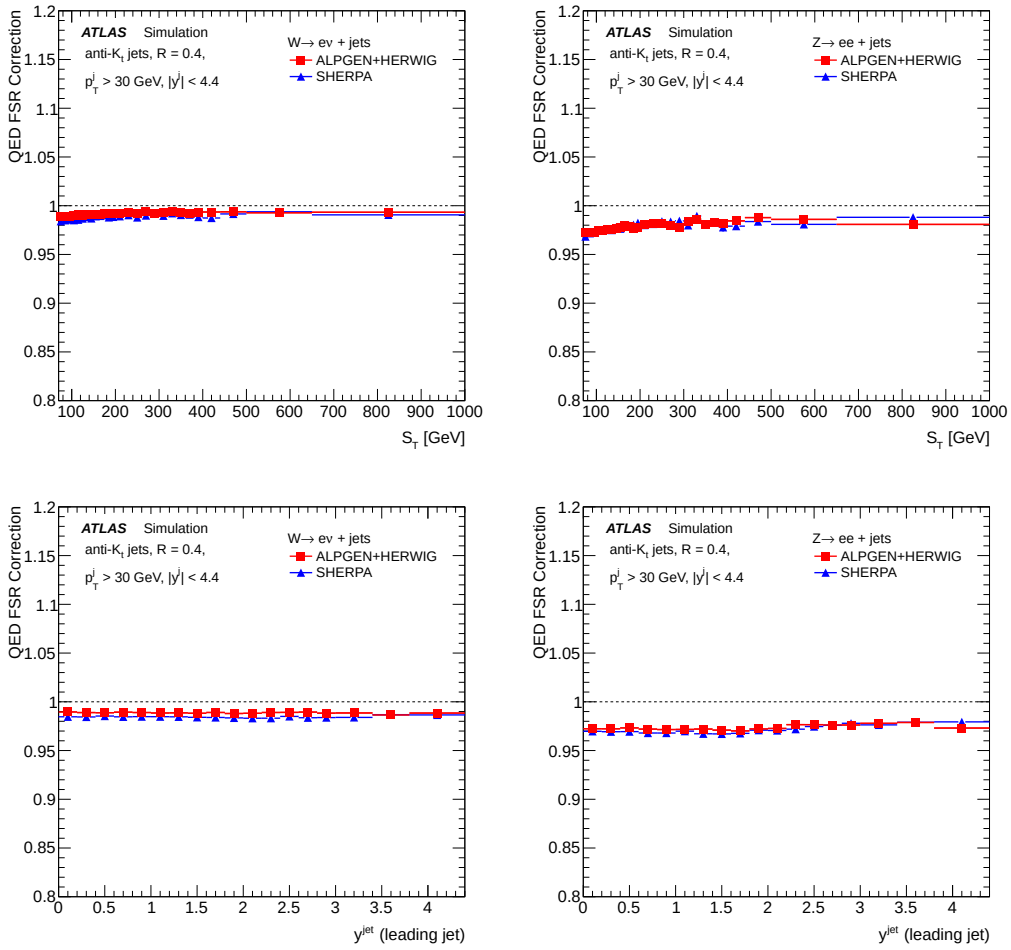

Figure 7.5: Electron channel QED final state radiation corrections for S_T for events with at least two jets (top) and leading jet rapidity in events with at least one jet (bottom). Left: W+jets channel; Right: Z+jets channel

multiplicative factors. The systematic uncertainty on the acceptance corrections was evaluated in the same way as for the QED corrections: an alternative set of corrections was formed using SHERPA samples and their difference from the nominal is symmeterised around the nominal corrections.

Figures 7.6 and 7.7 present examples of the acceptance corrections, shown are the corrections for exclusive jet multiplicity, leading jet P_T and rapidity, and the S_T for events with at least two jets. In all cases, the Z channel acceptance corrections are larger, this is expected as in this case there are two electrons in the final state, both of which are required to pass the fiducial phase space requirements.

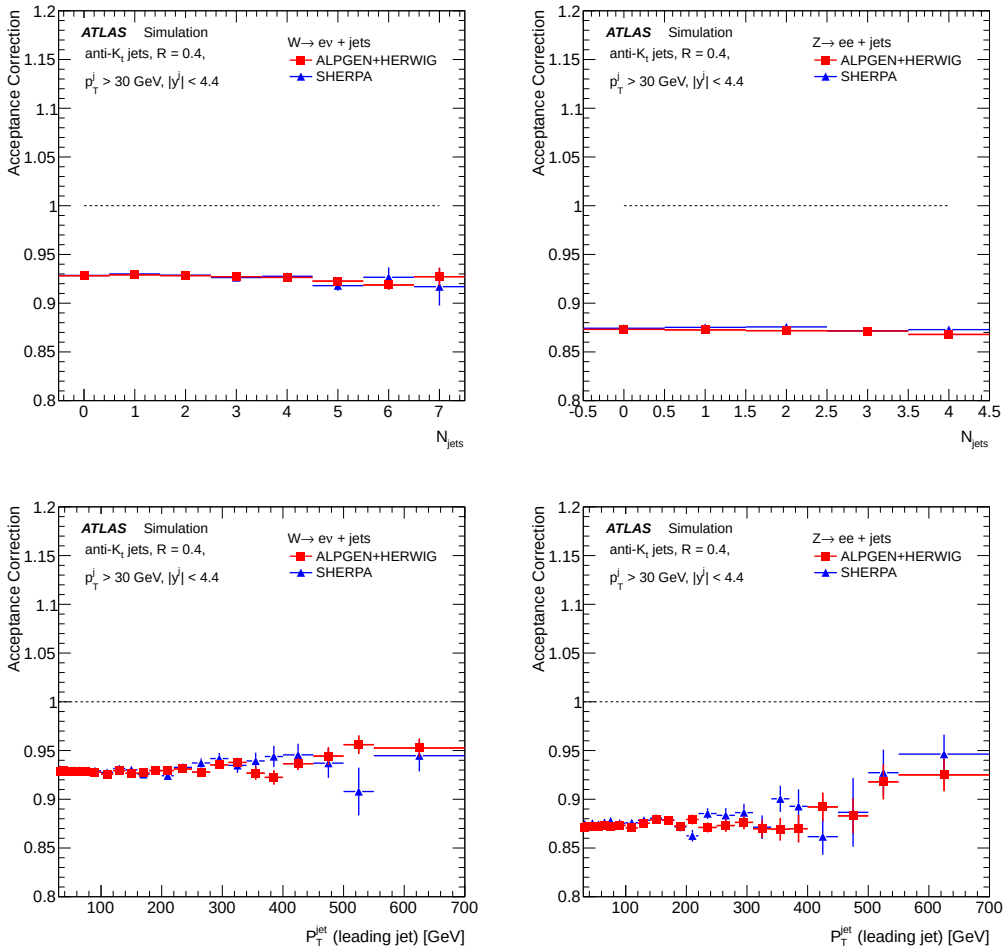

Figure 7.6: Electron channel acceptance corrections for exclusive jet multiplicity (top) and leading jet P_T for events with at least one jet (bottom). Left: W+jets channel; Right: Z+jets channel

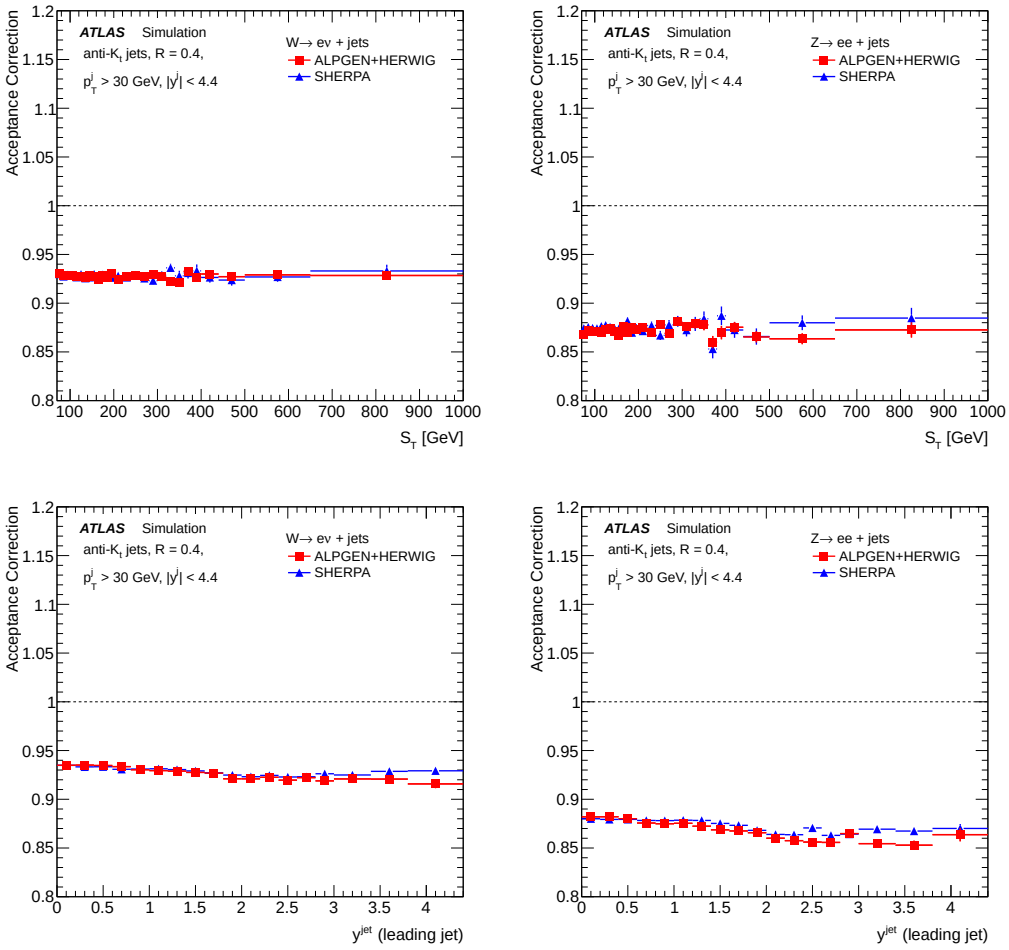

Figure 7.7: Electron channel acceptance corrections for S_T for events with at least two jets (top) and leading jet rapidity in events with at least one jet (bottom). Left: W+jets channel; Right: Z+jets channel

Chapter 8

Combined Results and Discussion

In this chapter, the method of combining the electron and muon channel measurements is discussed, and the final $\frac{\text{W+jets}}{\text{Z+jets}}$ ratio measurements are presented as a function of exclusive and inclusive jet multiplicity up to four jets. The ratio is also presented as a function of a host of kinematic variables for which there are significant differences in the behaviour of W+jets and Z+jets events. This is especially true in the kinematic regions where the mass differences between the W and Z affect the scale of partonic radiation from hard processes, and polarisation differences affect the kinematics of decay products upon which the event selections are based. The ratio is presented as a function of the P_T and rapidity of the leading and sub-leading jets in an event, the "di-jet" variables pertaining to the kinematics of the two leading jets, and the scalar sum of the P_T of all jets in an event[1].

Comparisons with theoretical predictions discussed in the previous chapter are presented, providing a test of how well such predictions describe the perturbative QCD processes to which the $\frac{\text{W+jets}}{\text{Z+jets}}$ ratio is sensitive (as demonstrated

[1]More kinematic variables than those presented in this chapter were investigated and deemed less relevant to the scope of the analysis. Therefore, only those more relevant to the scope of the analysis are presented and commented on here.

in Section 7.1).

8.1 Combination of Electron and Muon Channels

Once the electron and muon channel measurements have been unfolded to particle level, they were combined, exploiting lepton universality. This increases the statistics of the measurements and thus improves the precision of the differential cross-section measurements. Before combination, the individual lepton channels were extrapolated from their respective fiducial phase space into a common phase space (defined in Table 8.1) by correcting the lepton η requirement from the fiducial selection to $|\eta|<2.5$. Bin-by-bin acceptance correction factors derived using ALPGEN Monte Carlo samples in the manner described in Section 7.2.2.3 were applied to each distribution, but since we were extrapolating from fiducial to common phase space, they were defined as the reciprocal of Equation 7.4. Once extrapolated, the individual lepton channels were compared and the results were found to be compatible within their respective total (statistical+ systematic) uncertainties.

Selection	Common Phase Space
W$\rightarrow l\nu$	1 e or μ with $P_T > 25$ GeV and $\|\eta\|< 2.5$, 1 ν with $P_T > 25$ GeV, $m_T >$40 GeV
Z$\rightarrow ll$	2 OS l with $P_T > 25$ GeV and $\|\eta\|< 2.5$, $66 < m_{ll} < 116$ GeV, $\Delta R(l,l) > 0.2$
Jets	$P_T > 30$ GeV, $\|y\|<4.4$ and $\Delta R(jet,l) > 0.5$

Table 8.1: Common phase space for W and Z boson channels and jet selection. "OS" refers to a selection of two leptons of opposite sign, i.e. e^+e^- or $\mu^+\mu^-$.

The combination was achieved via an averaging procedure as described in [87, 88] whereby each distribution is combined separately by minimising the

following χ^2 function:

$$\chi^2 = \sum_{k,i} \frac{[m^i - \Sigma_j \gamma^i_{j,k} m^i b_j - \mu^i_k]^2}{(\sigma^i_{stat,k})^2 \mu^i_k (m^i - \Sigma_j \gamma^i_{j,k} m^i b_j) + (\sigma^i_{uncor,k} m^i)^2} + \sum_j b_j^2 \qquad (8.1)$$

where the index k runs over the two lepton channel sets of extrapolated measurements, i runs over the bins in each distribution and j runs over the correlated-across-bins sources of systematic uncertainty. The function is dependent on m^i and b_j, respectively the combined measurement (number of events) in bin i and the size of the systematic uncertainty j. $\sigma^i_{stat,k}$ and $\sigma^i_{uncor,k}$ are the relative statistical and uncorrelated systematic uncertainties on a measurement in bin i respectively. $\gamma^i_{j,k}$ is the relative correlated systematic uncertainty and quantifies the influence of the correlated error source j on the measurement in bin i in the dataset k. Finally, μ^i_k are the original measurements, the deviation of m^i from which is minimised.

For this approach, most sources of systematic uncertainty were treated as completely correlated across all channels and bins. They were the jet energy scale (JES), unfolding model, luminosity, Monte Carlo background uncertainties and all systematic uncertainties associated with the data driven $t\bar{t}$ background estimation (as described in Section 5.2.4), except the statistical uncertainty on the $t\bar{t}$ fit. Systematic uncertainties treated as correlated across bins, but independent between lepton channels, were the lepton uncertainties and those systematic uncertainties associated with the data driven QCD estimation as described in Section 5.1.3. The statistical uncertainties associated with data and Monte Carlo predictions, and the statistical uncertainties on the unfolding method and the $t\bar{t}$ fit, were all treated as completely uncorrelated across all bins and lepton channels. Also treated as completely uncorrelated was the jet energy resolution (JER) uncertainties[2].

[2]The JER uncertainties were treated as uncorrelated for technical reasons relating to the code which performed the combination. Work is ongoing to include the JER uncertainties as correlated, in the same way as JES. The effect of treating JER uncorrelated is not very

8.2 Results

This section presents the unfolded combined electron and muon channel $\frac{\text{W+jets}}{\text{Z+jets}}$ ratio measurements, with comparisons to theoretical predictions at leading order from ALPGEN and SHERPA, and next-to-leading order from BLACKHAT+SHERPA, after the corrections described in Section 7.2.2 have been applied. The distributions as a function of jet multiplicity correspond to the actual data luminosity. All other distributions have been normalised to unity, such that the shapes of the distributions of data and theoretical predictions to be accurately compared. The normalisation was achieved by dividing the measured differential cross-section distributions for the $\frac{\text{W+jets}}{\text{Z+jets}}$ ratio by the total cross-section obtained for the ratio of W+jets and Z+jets events, in corresponding jet multiplicity bin, as presented in Figure 8.1.

8.2.1 Jet Multiplicity

Figure 8.1 shows the $\frac{\text{W+jets}}{\text{Z+jets}}$ ratio combined measurement as a function of exclusive (left) and inclusive (right) jet multiplicity. For exclusive jet multiplicity, a good agreement with data is observed for both ALPGEN and BLACKHAT+SHERPA predictions. The good agreement excludes the zero-jet bin in which a discrepancy of approximately 2σ is observed for both predictions. The SHERPA predictions describe the data less well. As jet multiplicity increases, SHERPA systematically overestimates the value of the ratio such that at high multiplicities (the region in which the effects of hard QCD radiation are tested) the discrepancy is as large as 1.5σ.

For inclusive jet multiplicity, the data once again favours the predictions from ALPGEN while SHERPA increasingly overestimates the ratio with increasing jet multiplicity. The observed discrepancy between data and BLACKHAT+SHERPA in the higher jet multiplicity bins is expected. This is because BLACKHAT+SHERPA predictions are only available up to an exclusive jet

large and therefore has a negligible impact on the final results.

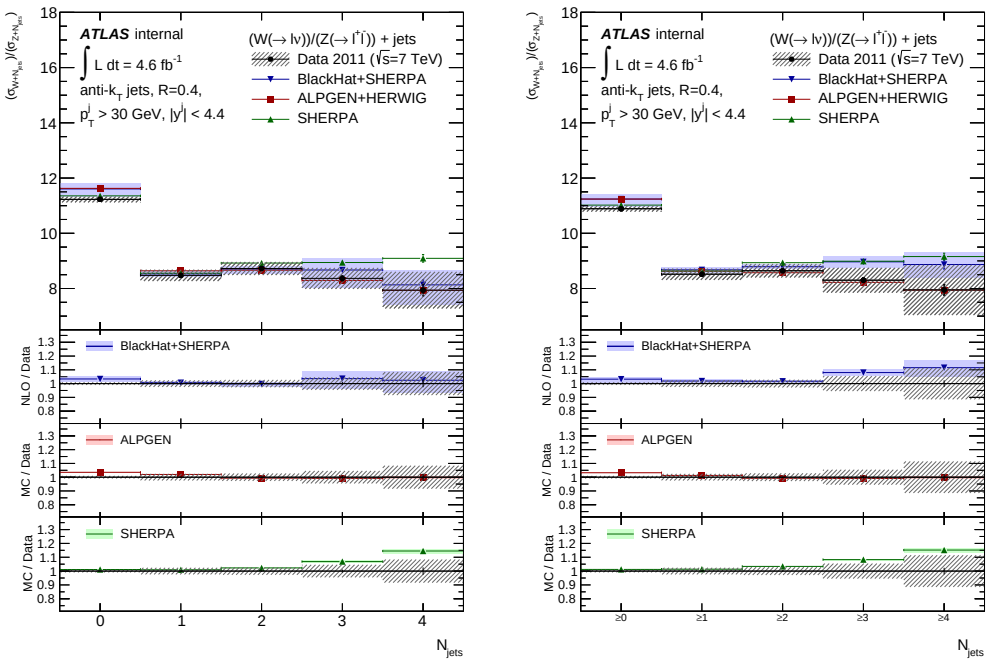

Figure 8.1: $\frac{\text{W+jets}}{\text{Z+jets}}$ ratio measurement of data unfolded to particle level in the combined electron and muon channel, presented as a function of exclusive (left) and inclusive (right) jet multiplicity.

multiplicity of four, and are therefore not directly comparable to data in the high inclusive jet multiplicity region.

8.2.2 Leading Jet P_T

Figures 8.2 and 8.3 respectively show the $\frac{\text{W+jets}}{\text{Z+jets}}$ ratio measurements as a function of leading jet P_T, for events with at least one jet (both lepton channels and the combined measurement) and exactly one jet. All distributions are normalised to their respective jet multiplicity bins as shown in Figure 8.1. In both distributions, a shape difference between W+jets and Z+jets events is observed in data for the region below 200 GeV, evidenced by the decay of the ratio values in this region before flattening out. The shape difference between the leading jet P_T distributions for W+jets and Z+jets events can be attributed to the differing mass of the W and Z bosons which in turn affects the scale of partonic radiation. Polarisation differences between the W and Z affect

the kinematic properties of their decay products, on which the fiducial event selections described in Section 4.1 are applied. For this reason, polarisation differences will also affect the shape of the W+jets and Z+jets distributions, contributing to the observed shape differences.

As shown in Section 7.1 (Figure 7.1), ALPGEN predictions for this distribution are steeper than the corresponding SHERPA predictions. The region below 80 GeV is where radiative parton shower effects are important and is thus the region that provides a test of the radiation model employed in the theoretical predictions. In this region we observe that the data is steeper than both predictions but in better agreement with ALPGEN than with SHERPA. This suggests the need for the generators to employ a better tuning of the parton shower interfaced to the matrix element.

In the region of high leading jet P_T (400-700 GeV) for events with at least one jet, we observe a systematic underestimation of the combined data across all predictions. This effect appears to be led by the electron channel. The individual lepton channel results show the consistent underestimation of approximately 1σ in the electron channel, yet a consistent overestimation in this region in the muon channel, albeit of smaller magnitude. Such a deviation is not observed in the combined ratio distribution for events with exactly one jet in the final state since there are insufficient statistics in the high P_T region of the Z+jets distribution to see such an effect. This statistical limitation derives from the high likelihood of a jet of 400-700 GeV radiating a jet of at least 30 GeV.

Figures 8.4 and 8.5 show the $\frac{\text{W+jets}}{\text{Z+jets}}$ ratio as a function of leading jet P_T for events with at least two and three jets respectively, where the specific requirement that the event contain a second (or third) jet of at least 30 GeV has been imposed. In these cases, the difference between the generators in how the parton shower is matched to the higher multiplicity matrix element is of greater importance than the case of events with at least one jet.

For events with at least two jets, the first observation is that the general

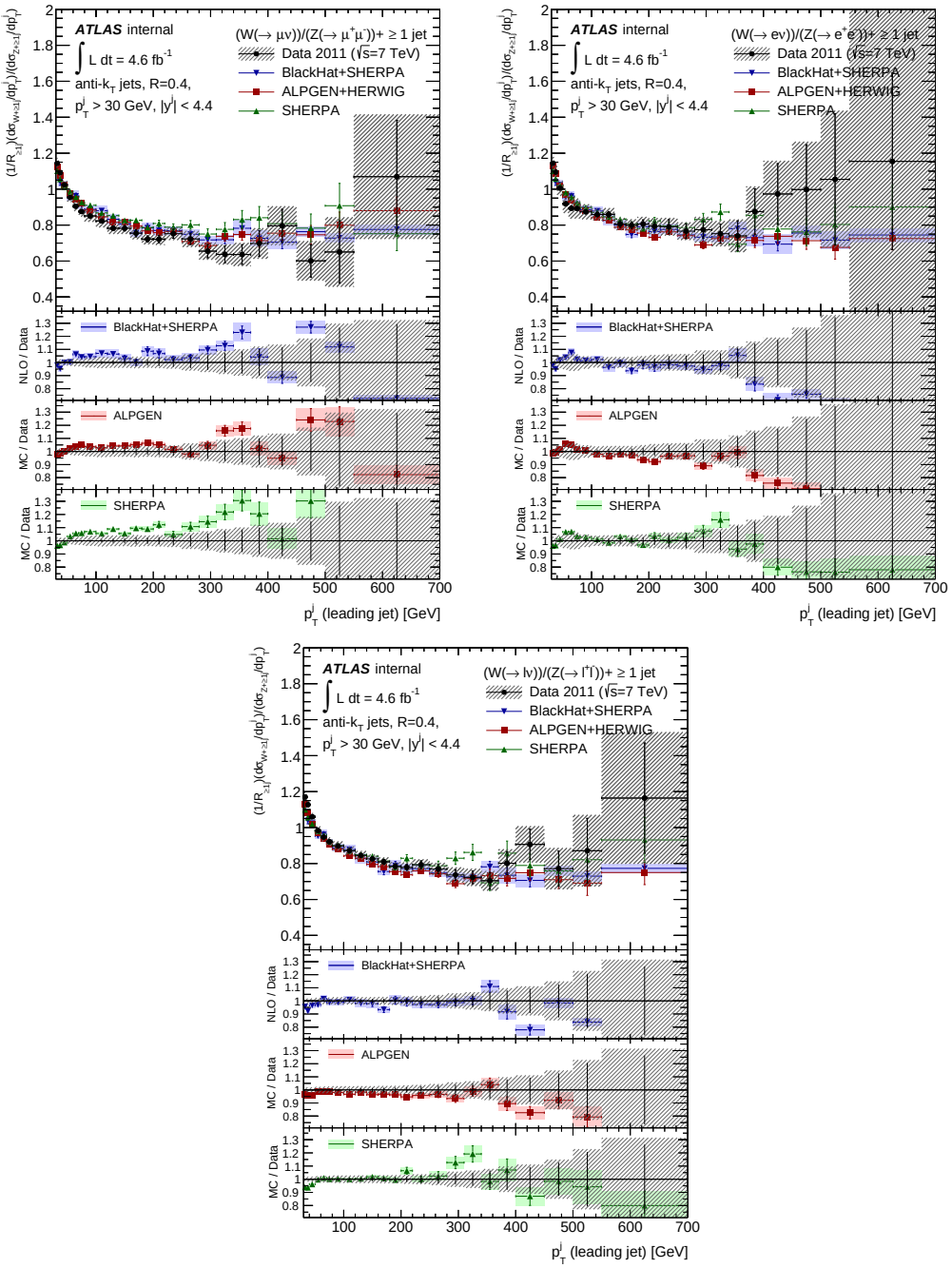

Figure 8.2: $\frac{\text{W+jets}}{\text{Z+jets}}$ ratio measurement of data unfolded to particle level as a function of leading jet P_T for events with at least one jet, in the muon (left), electron (right) and combined (centre) channels.

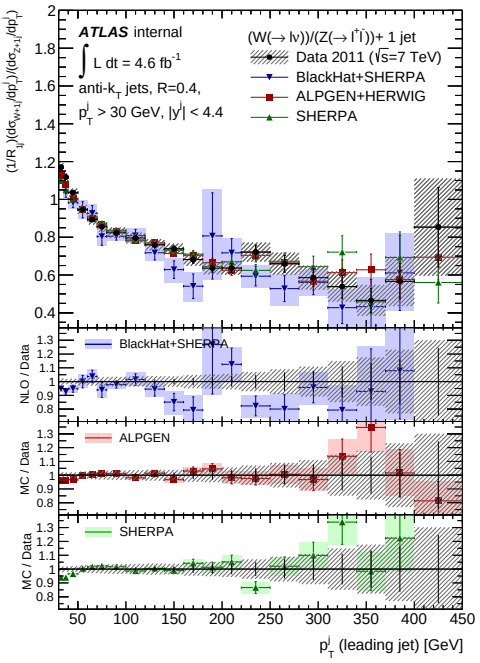

Figure 8.3: $\frac{\text{W+jets}}{\text{Z+jets}}$ ratio measurement of data unfolded to particle level as a function of leading jet P_T for events with exactly one jet, in the combined channel.

shapes of the data distributions are different than for events with at least and exactly one jet. Specifically, the data fall less steeply in the lower P_T region of the $\frac{\text{W+jets}}{\text{Z+jets}}$ ratio. This suggests that the differences between W+jets and Z+jets events discussed above propagate to the kinematics of higher multiplicity jets, as opposed to the case of at least one jet in the final state. This effect can be explained by the fact that, in such events, two jets can now recoil against each other which leaves W and Z bosons of a lower P_T than when there is only one jet. Since the average boson P_T is lower than the leading jet P_T, the effect of the mass and polarisation differences is reduced with respect to the case with at least one jet. This $\frac{\text{W+jets}}{\text{Z+jets}}$ ratio measurement is therefore more sensitive to QCD effects.

The $\frac{\text{W+jets}}{\text{Z+jets}}$ ratio for the combined electron and muon channels in Figure 8.4 exhibits similar features to that in Figure 8.2, namely that the data favours ALPGEN over SHERPA. This conclusion appears to be driven by the muon channel, since the electron channel distribution favours neither ALPGEN nor

SHERPA. Again for the combined result, in the low P_T region where differences between W+jets and Z+jets events are most pronounced, ALPGEN is still somewhat lacking in its ability to accurately predict the data distribution.

For the individual W+jets and Z+jets measurements (shown in Figure 8.6), there are significant discrepancies between ALPGEN and BLACKHAT+SHERPA at low P_T. This difference can be attributed to the lack, in BLACKHAT+SHERPA, of parton shower matching to the matrix element in the fixed order next-to-leading order calculation. The effect of this lack of correction is significantly cancelled in the ratio, for which ALPGEN and BLACKHAT+SHERPA predictions are in good agreement at low P_T. On the contrary, the effect of including the correction (but in different ways) is not cancelled, as observed by the differences between ALPGEN and SHERPA in this region, which is sensitive to differences between W+jets and Z+jets. The high P_T regions of the distributions in Figure 8.4 exhibit similar discrepancies as observed in the distributions presented in Figure 8.2 and described above.

The ratio distribution as a function of leading jet P_T for events with at least three jets (Figure 8.5) exhibits similar properties as that for at least two jets. The discrepancy between ALPGEN and BLACKHAT+SHERPA in the low P_T region is more pronounced for this distribution, suggesting that the lack of parton showering matched to matrix element is increasingly important for events with at least three jets of roughly the same P_T. Furthermore, this effect does not cancel in the ratio and is thus of different magnitude for W+jets and Z+jets events.

8.2.3 Sub-Leading Jet P_T

Figures 8.7 and 8.8 present the combined $\frac{\text{W+jets}}{\text{Z+jets}}$ ratio measurements as a function of the second and third most energetic jets for events with at least two and three jets in the final state. At low P_T, these distributions are probing the lowest energy jet in an event. With increasing P_T, there will be an increasing

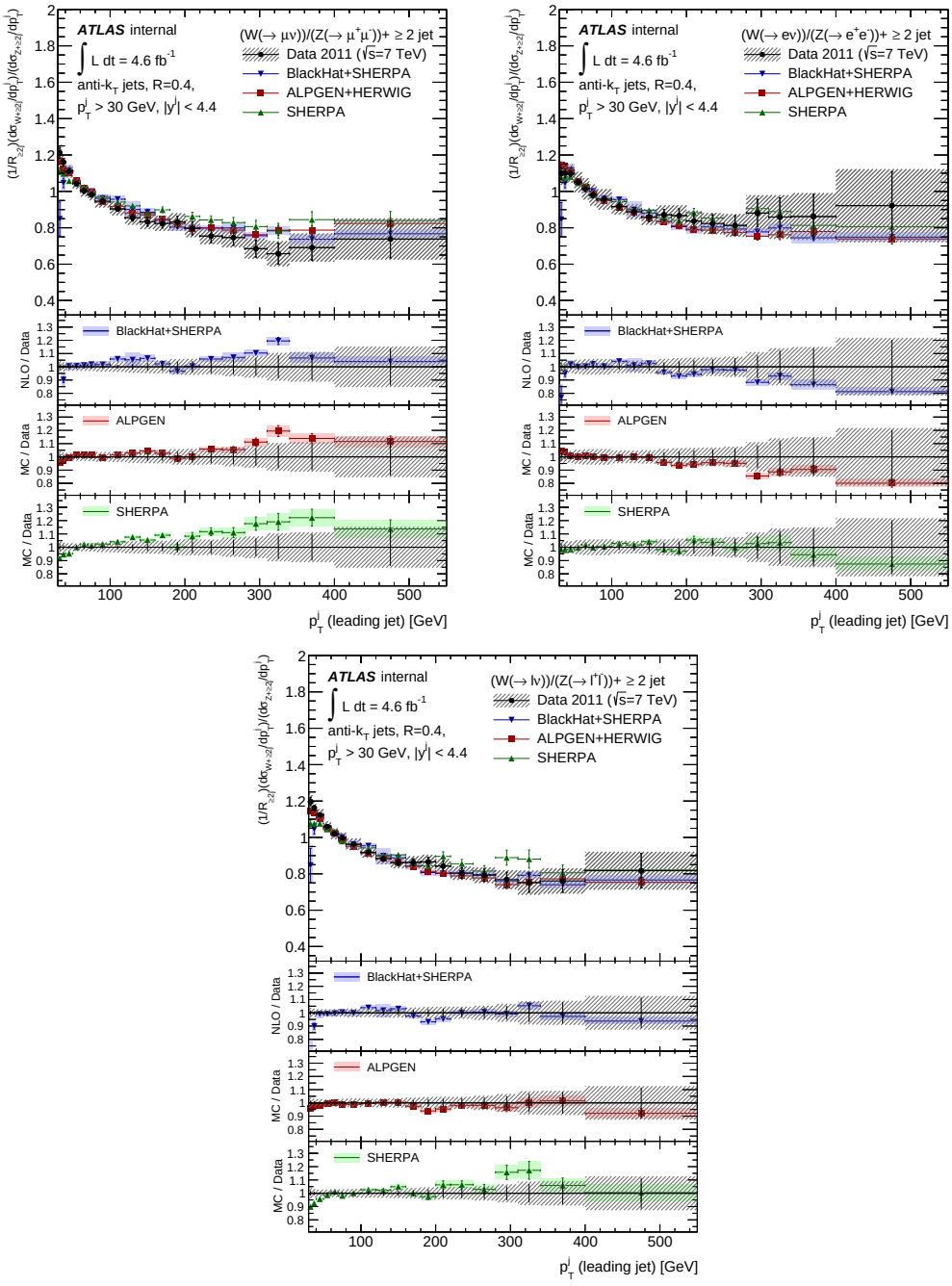

Figure 8.4: $\frac{\text{W+jets}}{\text{Z+jets}}$ ratio measurement of data unfolded to particle level as a function of leading jet P_T for events with at least two jets, in the muon (left), electron (right) and combined (centre) channels.

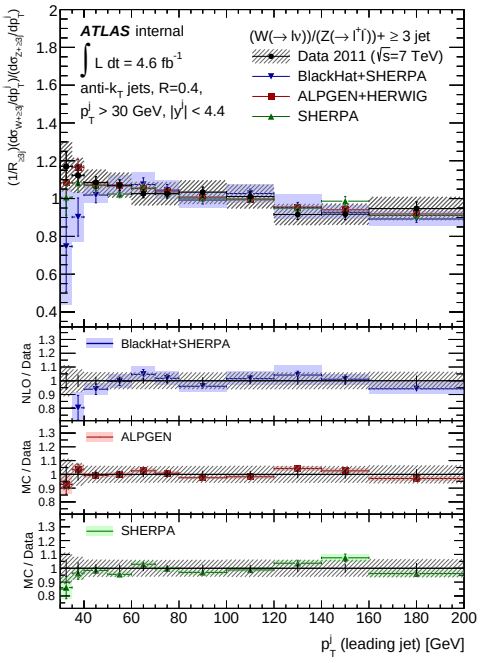

Figure 8.5: $\frac{\text{W+jets}}{\text{Z+jets}}$ ratio measurement of data unfolded to particle level as a function of leading jet P_T for events with at least 3 jets, in the combined channel.

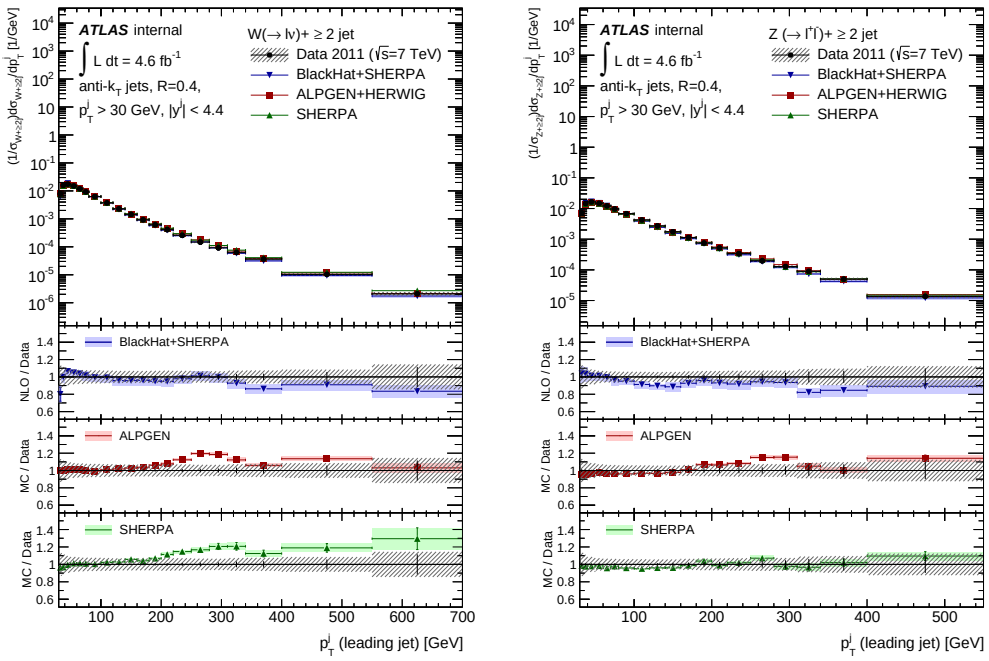

Figure 8.6: W+jets (left) and Z+jets (right) measurements of data unfolded to particle level as a function of leading jet P_T for events with at least two jets, in the combined channel.

fraction of these events with a lower P_T jet than the one probed. This contribution is marginal, however, it is nevertheless expected that the low and high P_T regions of the distributions shown will exhibit different levels of agreement between the data and theoretical predictions and will be discussed separately below.

In the region of low P_T, the data agrees well with the predictions provided by ALPGEN and BLACKHAT+SHERPA. As with the leading jet P_T distributions presented above, SHERPA falls less steeply than the data in this region. SHERPA is therefore less sensitive to the differences between W+jets and Z+jets events, radiating similar amounts of energy through the softest jet P_T for both W+jets and Z+jets events.

In the region of high P_T, we observe trends similar to those in the leading jet P_T distributions for events with at least one jet, i.e. that all theoretical predictions underestimate the data in the electron channel while overestimating the data in the muon channel. However, the conclusions in the region are somewhat affected by larger systematic uncertainties and data fluctuations than in the leading jet P_T distribution.

Similar trends can be observed for the third jet P_T distribution in Figure 8.8 but are less pronounced due to the flatter nature of the ratio and the large uncertainties on the measurement.

8.2.4 Scalar Sum P_T

Figure 8.9 shows the $\frac{\text{W+jets}}{\text{Z+jets}}$ ratio measurement as a function of S_T, the scalar sum of the P_T of all jets in an event, for events with at least two jets and exactly two jets respectively. This variable is often used in searches for new high-mass particles. The effects on the S_T distributions for events with more than two jets are obscured by large systematic uncertainties and data fluctuations, and are therefore not shown.

In the region of low S_T, it is observed that ALPGEN provides a better

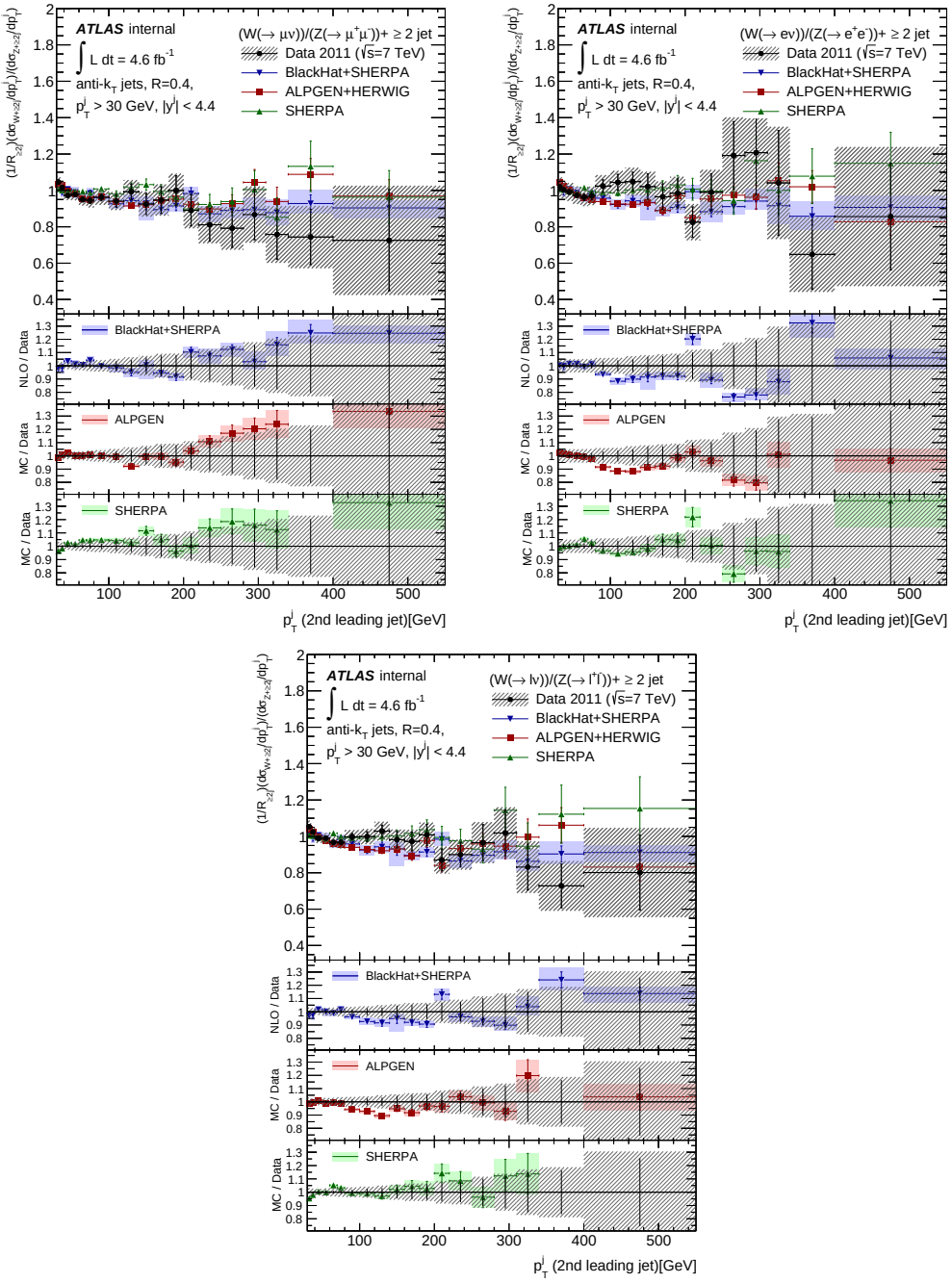

Figure 8.7: $\frac{\text{W+jets}}{\text{Z+jets}}$ ratio measurement of data unfolded to particle level as a function of the second leading jet P_T for events with at least two jets, in the muon (left), electron (right) and combined (centre) channels.

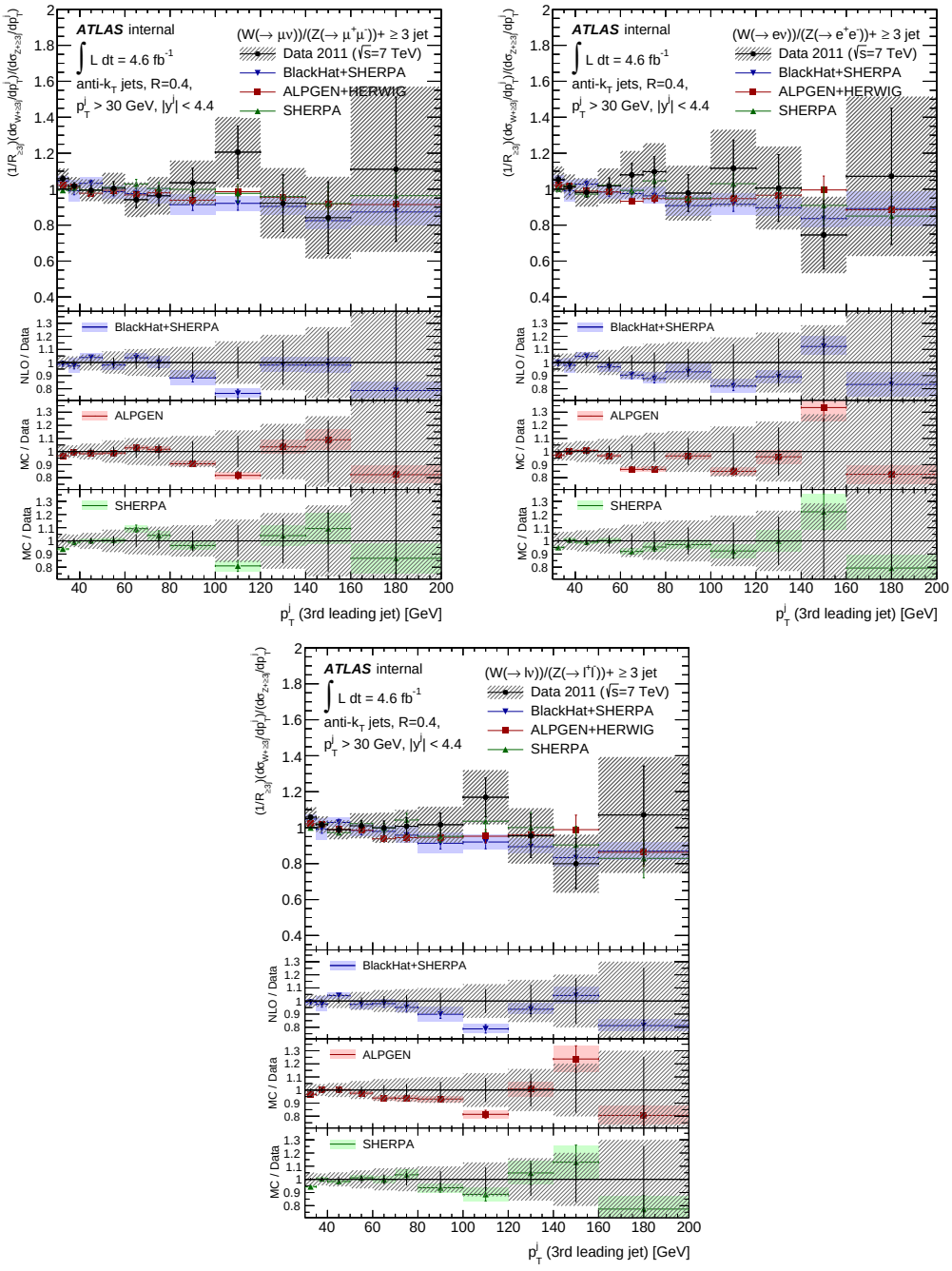

Figure 8.8: $\frac{\text{W+jets}}{\text{Z+jets}}$ ratio measurement of data unfolded to particle level as a function of the third leading jet P_T for events with at least three jets, in the muon (left), electron (right) and combined (centre) channels.

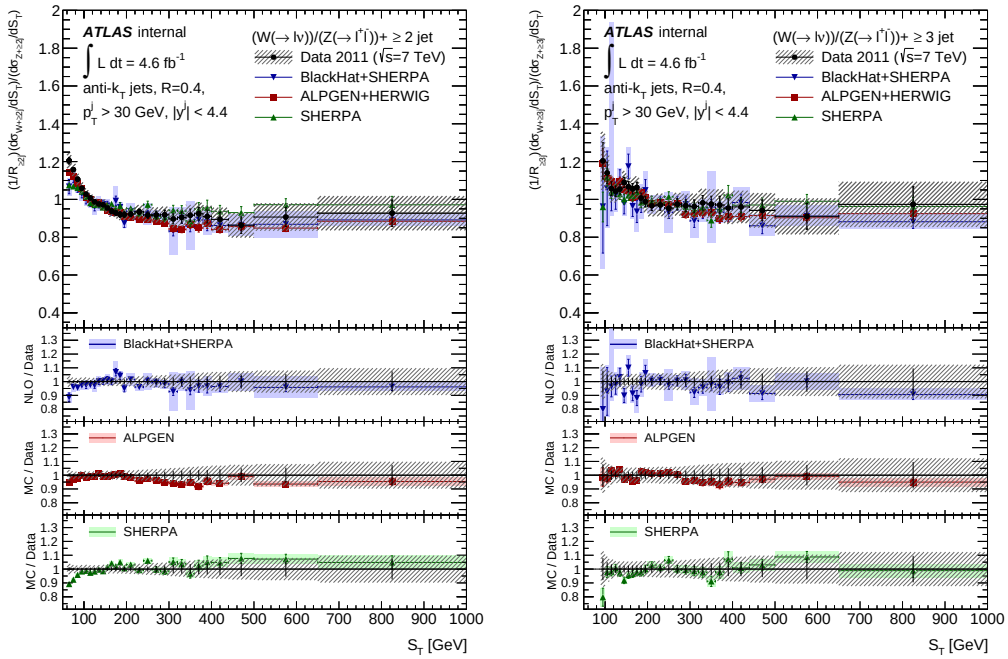

Figure 8.9: $\frac{\text{W+jets}}{\text{Z+jets}}$ ratio measurement of data unfolded to particle level in the combined electron and muon channel, presented as a function of S_T for events with at least two (left) and three (right) jets.

description of QCD radiation as there is a better agreement in this region with the data distribution than for SHERPA, which once again exhibits a less steeply falling, flatter ratio. In the region of high S_T, the data do not particularly agree with one theory prediction over another. The observations for the ratio in both low and high S_T regions are similar to those for leading and sub-leading jet P_T ratio distributions. This is to be expected since S_T is the scalar sum of all jet P_T in an event.

BLACKHAT+SHERPA predictions do not include higher-order contributions in the calculation of S_T. This means that higher multiplicity jets that contribute to the P_T sum in the high S_T region are not included, therefore BLACKHAT+SHERPA does not describe this S_T region of the individual W+jets and Z+jets distributions very well. However, this effect is significantly cancelled when the ratio is formed, yielding a good agreement with data for high S_T.

8.2.5 Jet Rapidity

Figures 8.10 and 8.11 present the $\frac{\text{W+jets}}{\text{Z+jets}}$ ratio measurement as a function of leading jet and second-leading jet rapidity in events with at least one and at least two jets respectively. In the region of low rapidity (below 2.5), a very good agreement is observed between the data and both the SHERPA and BLACKHAT+SHERPA predictions, while the data favours ALPGEN less in this region.

Figure 7.3 in Section 7.1 shows that there is a very large disagreement between ALPGEN and SHERPA predictions of leading jet rapidity in the region of high rapidity. This large discrepancy is attributable to differences in the PDF set used. While the uncertainty on the PDF is cancelled in the ratio, the effect of the difference between PDF sets for the ratio measurement, as a function of leading jet rapidity, is large at high rapidity. This is illustrated in Figure 8.12 which shows MCFM predictions for the leading jet rapidity ratio measurement, obtained with different PDF sets. As mentioned earlier, SHERPA employs a next-to-leading order PDF (CT10) whereas ALPGEN uses a leading order PDF (CTEQ6L). Leading order PDFs are not particularly reliable when probing the region of large longitudinal momentum fraction (x) considered when high rapidity jets are observed. Therefore, a large discrepancy between ALPGEN and SHERPA is to be expected in this region.

For Figure 8.10, at high rapidity (between 2.5-4.4), ALPGEN provides a poor description of the data in the electron channel, whereas SHERPA describes the data well. In the muon channel, ALPGEN overestimates the data in the high rapidity region but not as significantly as in the electron channel. SHERPA exhibits a significant underestimation of the muon channel data which is also manifest in the combined ratio measurement. It should be noted that although the electron and muon channels show different trends when compared with theory in the high rapidity region, the data measurements are compatible within errors. From Figure 8.11, similar observations can be

made about the ALPGEN and SHERPA description of the electron channel. However, here we observe a much better overall agreement between data and predictions for the combined ratio result.

8.2.6 Di-jet Variables

The final set of variables measured were those pertaining to the topology and invariant mass of the two leading jets (in P_T) in events with at least two jets. This subset are termed "di-jet" variables, here the ratio results are presented as a function of the angular distance, $\Delta R_{j_1,j_2} = \sqrt{(\Delta\phi_{j_1,j_2})^2 + (\Delta\eta_{j_1,j_2})^2}$, the separation in azimuthal angle, $\Delta\phi_{j_1,j_2}$, and invariant mass, M_{j_1,j_2}, of the two leading jets in an event. The $\frac{\text{W+jets}}{\text{Z+jets}}$ ratio results for the di-jet variables are shown in Figures 8.13 and 8.14.

For the ratio as a function of $\Delta R_{j_1,j_2}$, the predictions provided by ALPGEN, SHERPA and BLACKHAT+SHERPA exhibit no major shape differences between each other and mostly agree well with the data. The exception is in the low $\Delta R_{j_1,j_2}$ region of the spectrum where a large discrepancy with data is observed, this is driven by the electron channel. This analysis is primarily concerned with the behaviour of perturbative QCD calculations, therefore the low $\Delta R_{j_1,j_2}$ region is not of particular interest since non-perturbative effects are important here and are not expected to cancel in the $\frac{\text{W+jets}}{\text{Z+jets}}$ ratio. The non-perturbative contribution in this region is attributed to the fact that jets that are close together are more likely to be produced from softer radiation such as gluon splitting in the parton shower. Furthermore, such effects are not expected to cancel since the difference in mass between the W and Z bosons results in softer and broader jets in the low kinematic region of W+jets events than in the same region of Z+jets events.

The angular separation in ϕ is shown in Figure 8.14. Unlike the $\Delta R_{j_1,j_2}$ distribution, a large systematic discrepancy between data and all predictions at low values of $\Delta\phi_{j_1,j_2}$ is not observed. This is because two jets that are

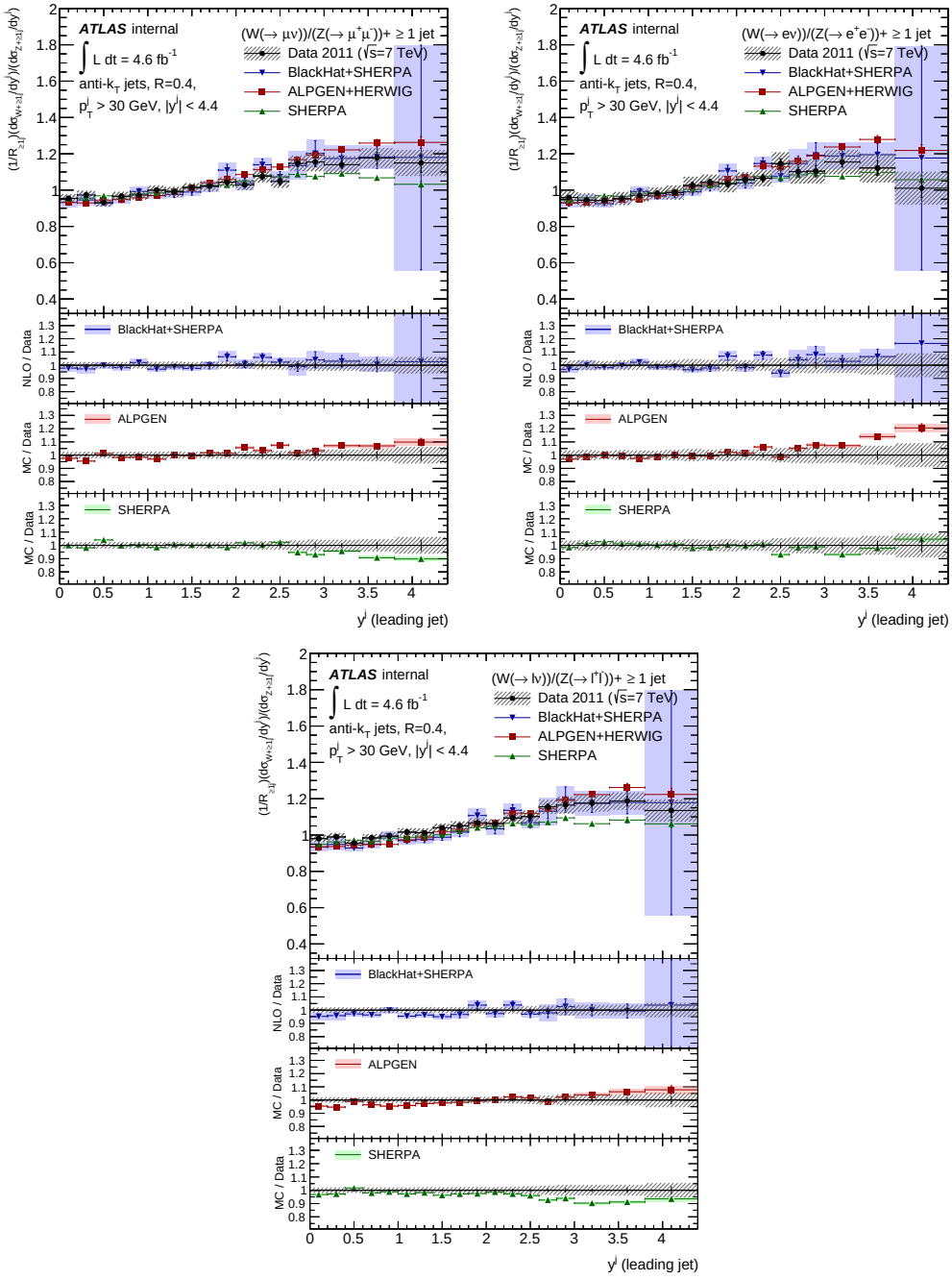

Figure 8.10: $\frac{\text{W+jets}}{\text{Z+jets}}$ ratio measurement of data unfolded to particle level as a function of the rapidity of the leading jet in events with at least one jet, in the muon (left), electron (right) and combined (centre) channels.

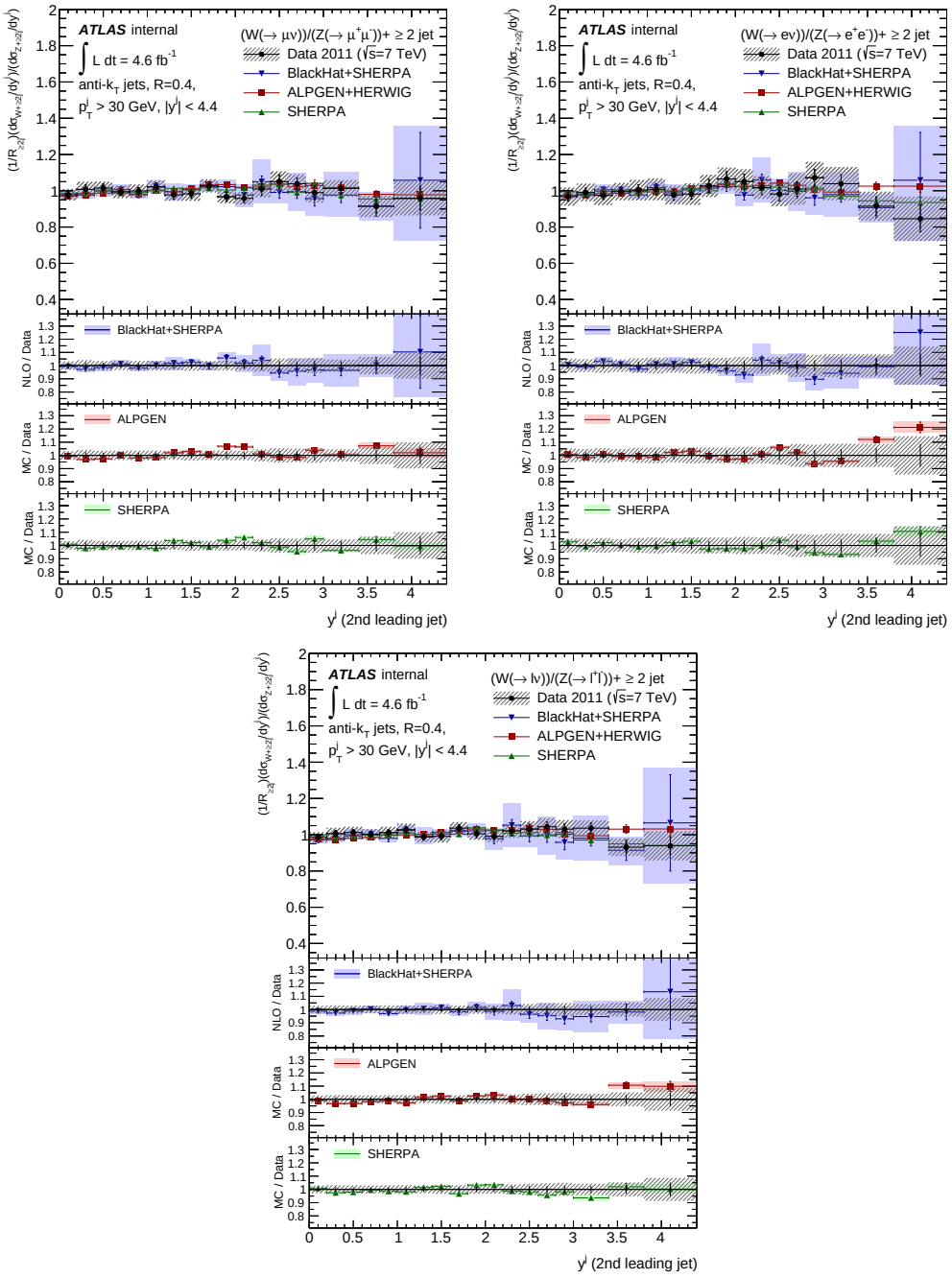

Figure 8.11: $\frac{\text{W+jets}}{\text{Z+jets}}$ ratio measurement of data unfolded to particle level as a function of the rapidity of the second leading jet in events with at least two jets, in the muon (left), electron (right) and combined (centre) channels.

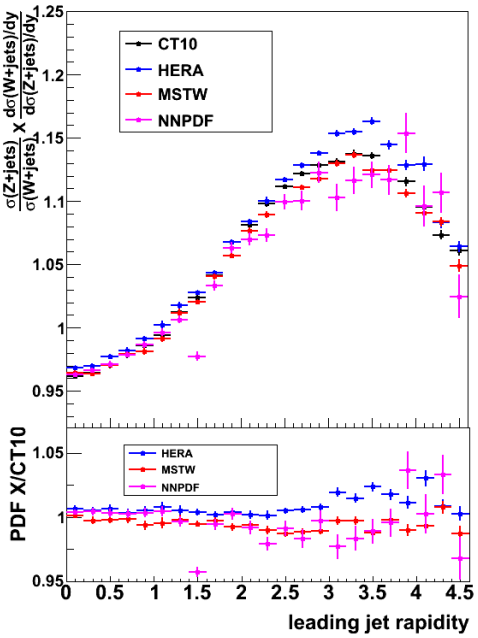

Figure 8.12: $\frac{\text{W+jets}}{\text{Z+jets}}$ ratio measurement as a function leading jet rapidity obtained from MCFM with four different PDF sets: CT10 (black), NNPDF 2.3 (cyan), MSTW 2008 (blue) and HERAPDF (red). Plot taken from [77]

close in ϕ may be well separated in rapidity and thus not necessarily have a small value of $\Delta R_{j_1,j_2}$. However, large discrepancies are observed between the data distribution and all predictions. Figure 8.15 gives a comparison between the theory predictions provided by ALPGEN and SHERPA for $\Delta\phi_{j_1,j_2}$ which clearly shows that jets are less separated in $\Delta\phi_{j_1,j_2}$ in the SHERPA predictions than in those provided by ALPGEN, and that this effect is more pronounced for Z+jets events.

For the invariant mass of the two leading jets, also shown in Figure 8.14, all predictions overestimate the data in the region below approximately 40 GeV. Above around 80 GeV there is agreement with data, apart from an upward trend in all predictions at approximately 500 GeV which is most likely attributable to a data fluctuation.

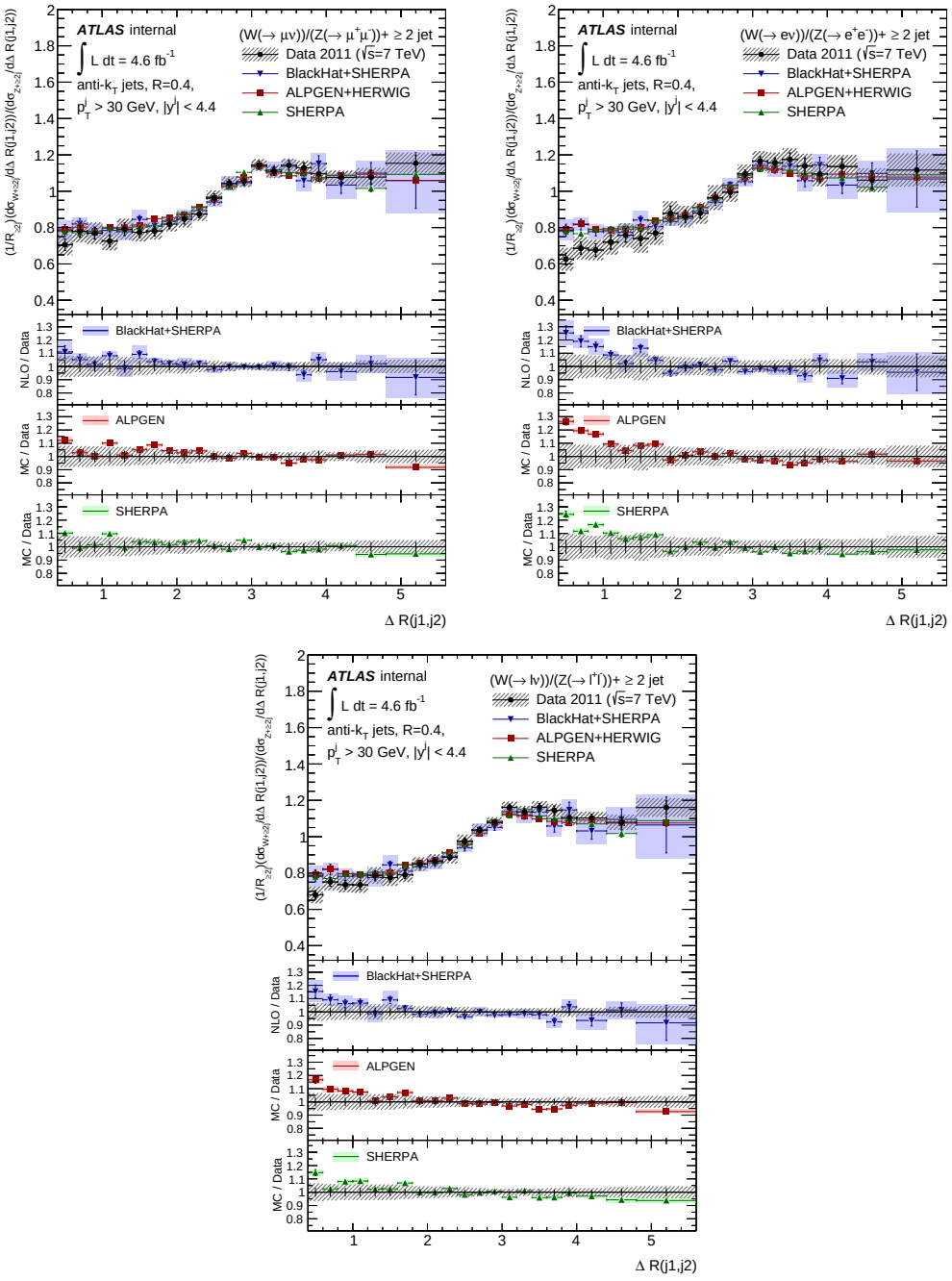

Figure 8.13: $\frac{\text{W+jets}}{\text{Z+jets}}$ ratio measurement of data unfolded to particle level as a function of the angular distance (ΔR) between the two leading jets in events with at least two jets, in the muon (left), electron (right) and combined (centre) channels.

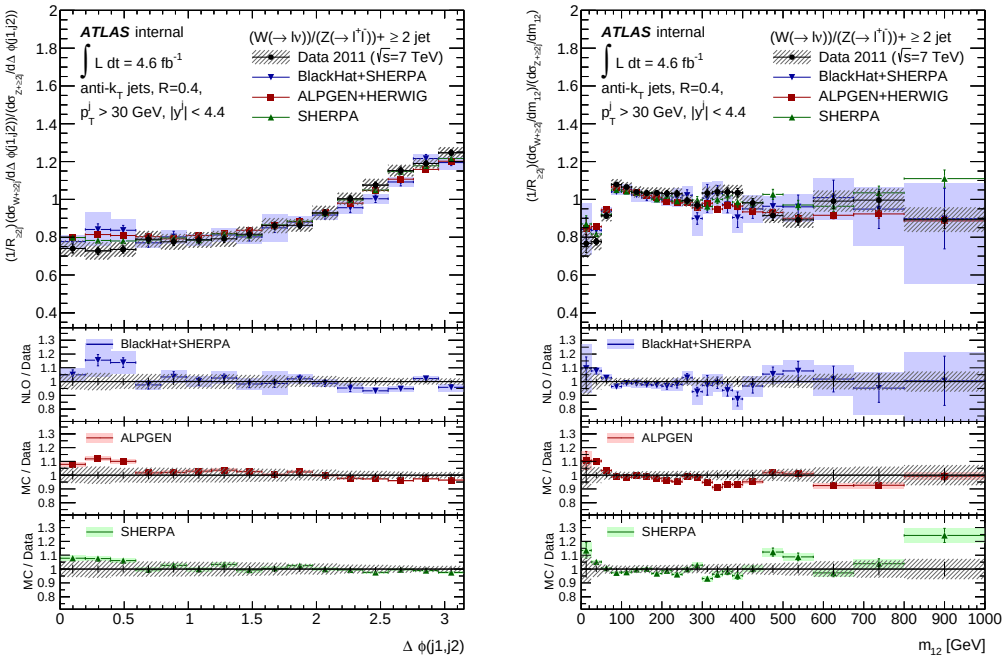

Figure 8.14: $\frac{\text{W+jets}}{\text{Z+jets}}$ ratio measurement of data unfolded to particle level as a function of the separation in azimuthal angle, $\Delta\phi_{j_1,j_2}$, of the two leading jets in events with at least 2 jets, in the combined channel.

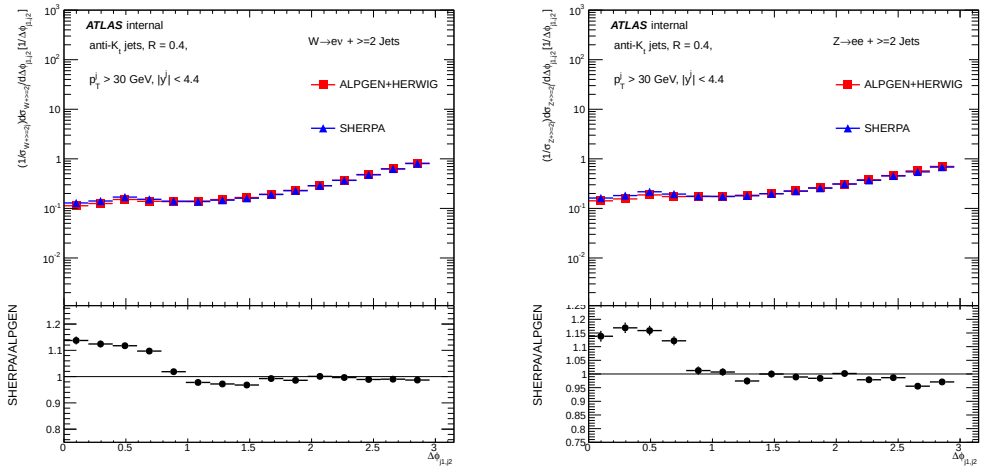

Figure 8.15: Comparison of ALPGEN+HERWIG and SHERPA theoretical predictions for $\Delta\phi_{j_1,j_2}$ between the two leading jets in events with at least two jets in the electron channel. Left: W+jets events; Right: Z+jets events.

Chapter 9

Conclusion

A $\frac{\text{W+jets}}{\text{Z+jets}}$ ratio measurement has been performed of the cross-section for hadronic jets produced in association with W and Z vector bosons. The analysis used 4.6 fb^{-1} of data acquired by the ATLAS detector during proton-proton collisions at the LHC, with a centre of mass energy $\sqrt{s}$=7 TeV. It has been demonstrated that the ratio measurement is sensitive to the differences between W+jets and Z+jets events, and that many systematic uncertainties on W+jets and Z+jets measurements are significantly reduced in the ratio. The cancellation of many non-perturbative effect such as those from hadronisation and multiple-parton interactions allow the ratio to provide a robust and sensitive test of theoretical predictions for perturbative QCD processes. The understanding of such processes is crucial for the future success of the ATLAS physics programme.

The measurement was performed in two separate lepton channels: for vector bosons decaying to electrons and muons. In each case, background processes were characterised by a combination of Monte Carlo simulation and data-driven techniques. The latter approach was taken for the understanding of multi-jet QCD backgrounds and those from semileptonic top decay. Following the subtraction of background processes, each channel was separately unfolded to particle level before being combined via a χ^2 minimisation technique.

The combined ratio measurements have been compared to theoretical predictions for perturbative QCD, arrived at from fixed order next-to-leading order calculations and high multiplicity leading-order matrix element calculations, matched to parton shower. The former were provided by BLACKHAT+SHERPA, the latter by ALPGEN+HERWIG and SHERPA Monte Carlo simulations.

The cross-section of the $\frac{\text{W+jets}}{\text{Z+jets}}$ ratio has been presented as a function of inclusive and exclusive jet multiplicity up to four jets. Differential cross-section $\frac{\text{W+jets}}{\text{Z+jets}}$ ratios were also presented as a function of the transverse momentum and rapidity of jets in the final state, of the scalar sum of all jet transverse momentum in an event, and of di-jet variables pertaining to the kinematics of the two leading jets. The ability of the various predictions to provide an accurate description of data in various kinematic regimes has been discussed.

To conclude, the advent of the LHC, and the unprecedented energies at which it is designed to operate, presents an extremely fertile hunting ground for hitherto undiscovered physics. Testament to this statement was the discovery of the Higgs boson in July 2012. Faced with the requirement of increasingly accurate theoretical predictions to describe perturbative QCD in the LHC environment, measurements to highlight the successes and failings of state-of-the-art predictions must be performed. The work presented in this thesis is one such measurement.

Bibliography

[1] ATLAS Collaboration, A measurement of the ratio of the W and Z cross sections with exactly one associated jet in pp collisions at $\sqrt{s} = 7$ TeV with ATLAS, Phys.Lett. B708 (2012) 221-240, arXiv:1108.4908.

[2] ATLAS Collaboration, Measurements of the W production cross sections in association with jets with the ATLAS detector, CERN-PH-EP-2014-199, arXiv:1409.8639.

[3] K.A. Olive et al. (Particle Data Group), Chin. Phys. C, 38, 090001 (2014).

[4] ATLAS Collaboration, Observation of a New Particle in the Search for the Standard Model Higgs Boson with the ATLAS Detector at the LHC, Physics Letters B 716 (2012), no. 1 1 29.

[5] CMS Collaboration, Observation of a New Boson at a Mass of 125 GeV with the CMS Experiment at the LHC, Physics Letters B 716 (2012), no. 1 30-61.

[6] ATLAS Collaboration, Determination of the strange quark density of the proton from ATLAS measurements of the W $\to l\nu$ and Z $\to ll$ cross sections, Phys.Rev.Lett. 109 (2012) 012001, arXiv:1203.4051

[7] Y. L. Dokshitzer, Calculation of Structure Functions of Deep-Inelastic Scattering and e^+e^- Annihilation by Perturbation Theory in Quantum Chromodynamics, JETP 46 (1977) 641. http://www.jetp.ac.ru/cgi-

bin/e/index/e/46/4/p641 (English Translation). Y. L. Dokshitzer Zh. Eksp. Teor. Fiz. 73 (1977) 1216. (Russian Original).

[8] V. N. Gribov and L. N. Lipatov Sov. J. Nucl. Phys. 15 675. (English Translation). V. N. Gribov and L. N. Lipatov Yad. Fiz. 15 1218. (Russian Original).

[9] V. N. Gribov and L. N. Lipatov Sov. J. Nucl. Phys. 15 438. (English Translation). V. N. Gribov and L. N. Lipatov Yad. Fiz. 15 781. (Russian Original).

[10] G. Altarelli and G. Parisi, Asymptotic Freedom in Parton Language, Nuclear Physics B 126 (1977), no. 2 298-318.

[11] The UA1 Collaboration, Experimental observation of isolated large transverse energy electrons with associated missing energy at $\sqrt{s} = 540$ GeV, Physics Letters B, Volume 122, Issue 1, 24 February 1983, Pages 103-116

[12] The UA2 Collaboration, Observation of single isolated electrons of high transverse momentum in events with missing transverse energy at the CERN $p - \bar{p}$ collider, Physics Letters B, Volume 122, Issues 5-6, 17 March 1983, Pages 476-485

[13] N. Cabibbo, Phys. Rev. Lett 10 (1963) 531.

[14] M. Kobayashi and T. Maskawa, Prog. Theor. Phys. 49 (1973) 652.

[15] S. Catani, Y. L. Dokshitzer, M. Olsson, G. Turnock and B. R. Webber, Phys. Lett. B 269, 432 (1991); S. Catani, Y. L. Dokshitzer, M. H. Seymour and B. R. Webber, Nucl. Phys. B 406, 187 (1993); S. D. Ellis and D. E. Soper, Phys. Rev. D 48, 3160 (1993) [hep-ph/9305266].

[16] Y. L. Dokshitzer, G. D. Leder, S. Moretti and B. R. Webber, JHEP 9708, 001 (1997) [hep-ph/9707323]; M. Wobisch and T. Wengler [hep-ph/9907280].

[17] M. Cacciari, G. P. Salam G. Soyez, JHEP 0804 (2008) 063, arXiv:0802.1189.

[18] G. Corcella, et al., JHEP 0101, 010 (2001). DOI 101.041 1088/1126-6708/2001/01/010

[19] Matteo Cacciari, Gavin P. Salam, Gregory Soyez, The Anti-k(t) jet clustering algorithm, JHEP 0804 (2008) 063, arXiv:0802.1189

[20] GEANT4 Collaboration, S. Agostinelli et al., GEANT4: A simulation toolkit, Nucl. Instrum. Meth. A506 (2003) 250-303.

[21] J. Butterworth, J.R. Forshaw, M. Seymour, Z. Phys1.043 C72, 637 (1996). DOI 10.1007/s002880050286

[22] M.L. Mangano, et al., JHEP 0307, 001 (2003). DOI1039 10.1088/1126-6708/2003/07/001

[23] J. Pumplin, et al., JHEP 0207, 012 (2002). DOI 10.1088/1047 1126-6708/2002/07/012

[24] T. Gleisberg, et al., JHEP 0902, 007 (2009). DOI 10. 1088/1126-6708/2009/02/007

[25] H.L. Lai, et al., Phys. Rev. D82, 074024 (2010). DOI 10.1103/Phys-RevD.82.074024

[26] C. Berger, et al., Phys. Rev. D80, 074036 (2009). DOI 10.1103/Phys-RevD.80.074036

[27] C. Berger, et al., Phys. Rev. D82, 074002 (2010). DOI 10.1103/Phys-RevD.82.074002

[28] C. Berger, et al., Phys. Rev. Lett. 106, 092001 (2011). DOI 10.1103/Phys-RevLett.106.092001

[29] CERN, The accelerator complex, http://public.web.cern.ch/public/en/research/AccelComplex-en.html, 2012.

[30] https://twiki.cern.ch/twiki/bin/view/AtlasPublic/LuminosityPublicResults

[31] ATLAS Collaboration, J. Pequenao, Computer Generated Image of the Whole ATLAS Detector. http://cds.cern.ch/record/1095924, March, 2008.

[32] ATLAS Collaboration. ATLAS Detector and Physics Performance Technical Design Report: Volume One, May 1999. pages 3. CERN/LHCC 99-15.

[33] ATLAS Collaboration, J. Pequenao, Computer Generated Image of the ATLAS Inner Detector. http://cds.cern.ch/record/1095926, March, 2008.

[34] The ATLAS Collaboration, G. Aad et al., The ATLAS Experiment at the CERN Large Hadron Collider, JINST 3 (2008). pages 53. S08003.

[35] ATLAS Collaboration. ATLAS Detector and Physics Performance Technical Design Report: Volume One, May 1999. pages 7-8. CERN/LHCC 99-15.

[36] ATLAS Collaboration. ATLAS Detector and Physics Performance Technical Design Report: Volume One, May 1999. pages 9. CERN/LHCC 99-15.

[37] The ATLAS Collaboration, G. Aad et al., The ATLAS Experiment at the CERN Large Hadron Collider, JINST 3 (2008). pages 56-58. S08003.

[38] The ATLAS Collaboration, G. Aad et al., The ATLAS Experiment at the CERN Large Hadron Collider, JINST 3 (2008). pages 64-65. S08003.

[39] ATLAS Collaboration. ATLAS Detector and Physics Performance Technical Design Report: Volume One, May 1999. pages 10. CERN/LHCC 99-15.

[40] C. Jacoboni, C. Canali, G. Ottaviani and A. Alberighi Quaranta, A review of some charge transport properties of silicon , Solid State Electronics 20 (1977) 77 - 89

[41] C. Canali, G. Majini, R. Minder and G. Ottaviani, Electron and hole drift velocity measurements in silicon and their empirical relation to electric field and temperature, IEEE Trans. Electron Devices ED-7, (1970) 481.

[42] E. Coniavitis, A. Okamoto, and R. Tanaka, Lorentz angle and cluster width studies for the atlas sct, ATLAS note ATL-COM-INDET-2009-039 (2009).

[43] J. Becker, E. Fretwurst , R. Klanner, Measurements of charge carrier mobilities and drift velocity saturation in bulk silicon of <111> and <100> crystal orientation at high electric fields, Solid-State Electronics 56 (2011), 104-110.

[44] The ATLAS Collaboration, G. Aad et al., The ATLAS Experiment at the CERN Large Hadron Collider, JINST 3 (2008). pages 59. S08003.

[45] ATLAS Collaboration. ATLAS Detector and Physics Performance Technical Design Report: Volume One, May 1999. pages 12-14. CERN/LHCC 99-15.

[46] ATLAS Collaboration. ATLAS Detector and Physics Performance Technical Design Report: Volume One, May 1999. pages 14-17. CERN/LHCC 99-15.

[47] TLAS Collaboration, J. Pequenao, Computer Generated Image of the ATLAS Calorimeter. http://cds.cern.ch/record/1095927, March, 2008.

[48] ATLAS Collaboration. ATLAS Detector and Physics Performance Technical Design Report: Volume One, May 1999. pages 17-19. CERN/LHCC 99-15.

[49] ATLAS Collaboration. ATLAS Detector and Physics Performance Technical Design Report: Volume One, May 1999. pages 20. CERN/LHCC 99-15.

[50] ATLAS Collaboration. ATLAS Detector and Physics Performance Technical Design Report: Volume One, May 1999. pages 21-22. CERN/LHCC 99-15.

[51] ATLAS Collaboration, J. Pequenao, Computer Generated Image of the ATLAS Muons Subsystem. http://cds.cern.ch/record/1095929, March, 2008.

[52] ATLAS Collaboration, Cross-section of the Barrel of the ATLAS Muon Spectrometer. NIKHEF ATLAS Wiki, http://www.nikhef.nl/pub/experiments/atlaswiki/index.php/Chapter˙II.

[53] ATLAS Collaboration. ATLAS Detector and Physics Performance Technical Design Report: Volume One, May 1999. pages 23-26. CERN/LHCC 99-15.

[54] https://twiki.cern.ch/twiki/bin/view/AtlasProtected/GoodRunListsForAnalysis

[55] ATLAS Collaboration. New ATLAS event generator tunes to 2010 data (2011). https://cds.cern.ch/1050 record/1345343. ATL-PHYS-PUB-2011-008

[56] P. Golonka and Z. Was, Eur. Phys. J. C50 (2007) 53-62, arXiv:hep-ph/0604232.

[57] A. Sherstnev and R. Thorne, Eur. Phys. J. C 55 (2008) 553-575, arXiv:0711.2473

[58] T. Sjstrand, S. Mrenna, and P. Z. Skands, JHEP 0605 (2006) 026, arXiv:hep-ph/0603175

[59] ATLAS Collaboration, Eur. Phys. J. C 74 (2014) 294, arXiv:1404.2240

[60] ATLAS Collaboration, B. Resende, Muon Identification Algorithms in ATLAS, September, 2009. Europhysics Conference on High Energy Physics Proceedings. http://cds.cern.ch/record/1209632/.

[61] ATLAS Collaboration, arXiv:1404.4562. submitted to Eur. Phys. J. C.

[62] ATLAS Collaboration, Electron and photon energy calibration with the ATLAS detector using Run 1 data. Eur.Phys.J. C74 (2014) 10, 3071, arXiv:1407.5063

[63] ATLAS Collaboration, G. Aad et al., Jet energy scale and its systematic uncertainty for jets produced in proton-proton collisions at s = 7 TeV and measured with the ATLAS detector, Tech. Rep. ATLAS-CONF-2010-056, CERN, Geneva, 2010.

[64] ATLAS Collaboration, G. Aad et al., Jet energy measurement with the ATLAS detector in proton-proton collisions at $\sqrt{s}$ = 7 TeV, Tech. Rep. CERN-PH-EP-2011-191, CERN, Geneva, 2011. arXiv:1112.6426.

[65] ATLAS Collaboration, G. Aad et al., Charged particle multiplicities in pp interactions at $\sqrt{s}$ = 900 GeV and 7 TeV in a diffractive limited phase-space measured with the ATLAS detector at the LHC and new PYTHIA6 tune, Tech. Rep. ATLAS-CONF-2010-031, CERN, Geneva, 2010.

[66] ATLAS Collaboration, Jet energy scale and its systematic uncertainty in proton-proton collisions at $\sqrt{s}$ = 7 TeV with ATLAS 2011 data, ATLAS-CONF-2013-004. http://cds.cern.ch/record/1509552.

[67] ATLAS Collaboration, Eur. Phys. J. C73 (2013) 2306, arXiv:1210.6210.

[68] ATLAS Collaboration, Performance of Missing Trans- verse Momentum Reconstruction in ATLAS with 2011 Proton-Proton Collisions at $\sqrt{s}$ = 7 TeV (2012). ATLAS- CONF-2012-101

[69] Ryan Gavin, Ye Li, Frank Petriello, Seth Quackenbush. FEWZ 2.0: A code for hadronic Z production at next-to-next-to-leading order. Comput.Phys.Commun. 182 (2011) 2388-2403. arXiv:1011.3540

[70] Michal Czakon, Alexander Mitov. Top++: A Program for the Calculation of the Top-Pair Cross-Section at Hadron Colliders. arXiv:1112.5675

[71] J. Butterworth, E. Dobson, U. Klein, B. Mellado Garcia, T. Nunnemann, J. Qian, D. Rebuzzi, and R. Tanaka, Single Boson and Diboson Production Cross Sections in pp Collisions at $\sqrt{s} = 7$ TeV, Tech. Rep. ATL-COM-PHYS-2010-695, CERN, Geneva, Aug, 2010.

[72] Top Group Twiki Page, https://twiki.cern.ch/twiki/bin/viewauth/AtlasProtected/TopMC11.

[73] http://root.cern.ch/root/htmldoc/TFractionFitter.html

[74] ATLAS Collaboration, Commissioning of the ATLAS high-performance b-tagging algorithms in the 7 TeV collision data (2011). https://cds.cern.ch/record/1101 1369219. ATLAS-CONF-2011-102

[75] ATLAS Collaboration, Measurement of the top quark pair production cross-section with ATLAS in the single lepton channel, Phys. Lett B 711 (2012) 244-263

[76] http://root.cern.ch/drupal/content/roofit

[77] ATLAS Collaboration, A measurement of the W production cross section and the ratio of W to Z production cross section in association with jets with the ATLAS detector. ATL-COM-PHYS-2013-590. https://cds.cern.ch/record/1545593

[78] G. D'Agostini, A multidimensional unfolding method based on Bayes theorem. Nuclear Instruments and Methods in Physics Research A 362 (1995) 487-498.

[79] Tim Adye, in Proceedings of the PHYSTAT 2011 Workshop on Statistical Issues Related to Discovery Claims in Search Experiments and Unfolding, CERN, Geneva, Switzerland, 17-20 January 2011, edited by H.B. Prosper and L. Lyons, CERN-2011-006, pp. 313-318.

[80] ATLAS Collaboration, Study of jets produced in association with a W boson in pp collisions at $\sqrt{s} = 7$ TeV with the ATLAS detector. Phys.Rev. D85 (2012) 092002. DOI: 10.1103/PhysRevD.85.092002

[81] K. et al.. Bierwagen, Measurement of the cross section for jets produced in association with Z bosons, ATL-COM-PHYS-2012-735 .

[82] J. Alwall et al., Eur. Phys. J. C53 (2008) 473-500, arXiv:0706.2569.

[83] ATLAS Collaboration, Eur. Phys. J. C73 (2013) 2518, arXiv:1302.4393.

[84] S. Hoeche, F. Krauss, M. Schonherr, F. Siegert, JHEP 1304, 027 (2013). DOI 10.1007/JHEP04(2013)027

[85] P.Z. Skands, Phys. Rev. D82, 074018 (2010). DOI 10. 1103/Phys-RevD.82.074018

[86] D. Yennie, S.C. Frautschi, H. Suura, Annals Phys. 13, 379 (1961). DOI 10.1016/0003- 4916(61)90151- 8

[87] A. Glazov, AIP Conf.Proc. 792, 237 (2005). DOI 10. 1063/1.2122026

[88] F. Aaron, et al., Eur.Phys.J. C63, 625 (2009). DOI 10.1140/ep jc/s10052-009- 1128- 6